Errata

p.38	line 25	radiation can recorded... *should read* radiation can be recorded...
p.40	line 4	NaI... *should read* NaI(Tl)...
p.40	Figure 2.2	gd-153... *should read* Gd-153...
p.41	Figure 2.3	x-ray source *should read* x-ray source filtered with 0.6 gcm^{-2} samarium
p.42	line 27	NaI... *should read* NaI(Tl)...
p.45	line 20	Gadolinium... *should read* gadolinium...
	line 21	Germanium... *should read* germanium...
	line 26	Samarium... *should read* samarium...
p.51	line 28	interaction are... *should read* interaction is...
	line 30	since they retain their... *should read* since it retains it's...
p.67	line 7	equ.4.1 $\rho = \rho_e(Z/A)_{eff}N_A$ *should read* $\rho_e = \rho(Z/A)_{eff}N_A$
p.73	line 29	Density measurements were found to be... *should read* The error in the density measurements was found to be...
p.74	line 2	NaI... *should read* NaI(Tl)...
p.81	line 2	using calculus can found... *should read* using calculus can be found...
p.97	line 7	trochanter was also used a landmark... *should read* trochanter was also used as a landmark...
p.106	line 11	as kerma During... *should read* as kerma. During...
p.126	line 11	this would only valid... *should read* this would only be valid...
p.152	line 5	which were not... *should read* which had not...

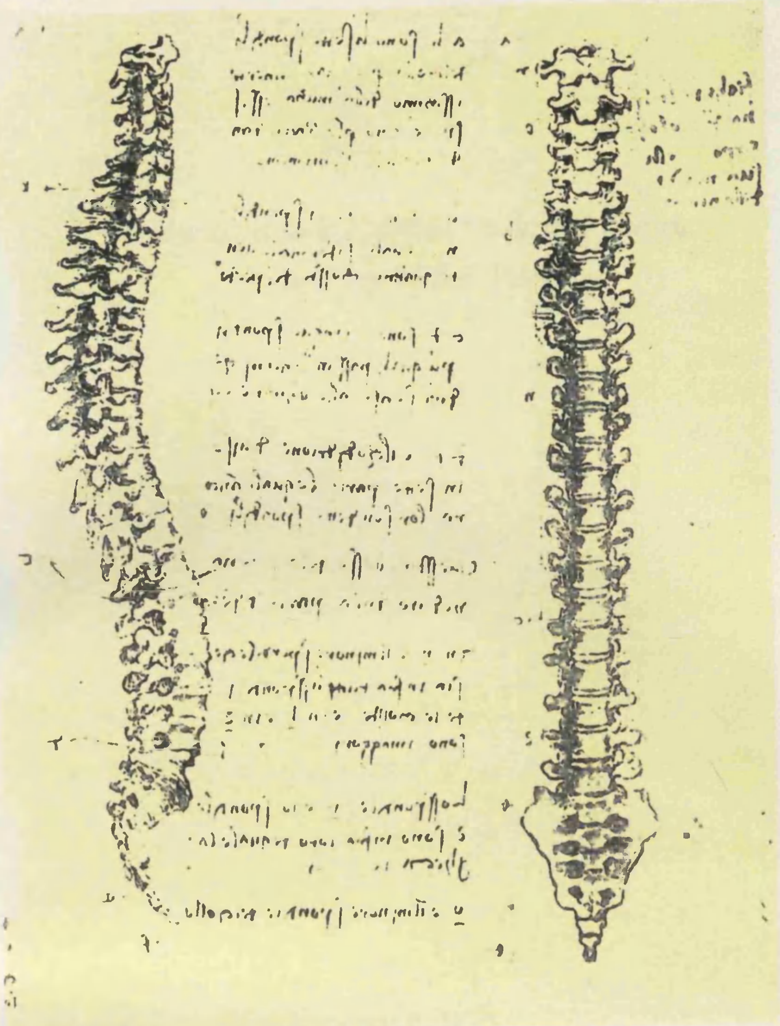

Plate 1. The vertebral column *by Leonardo da Vinci (1452-1519)*

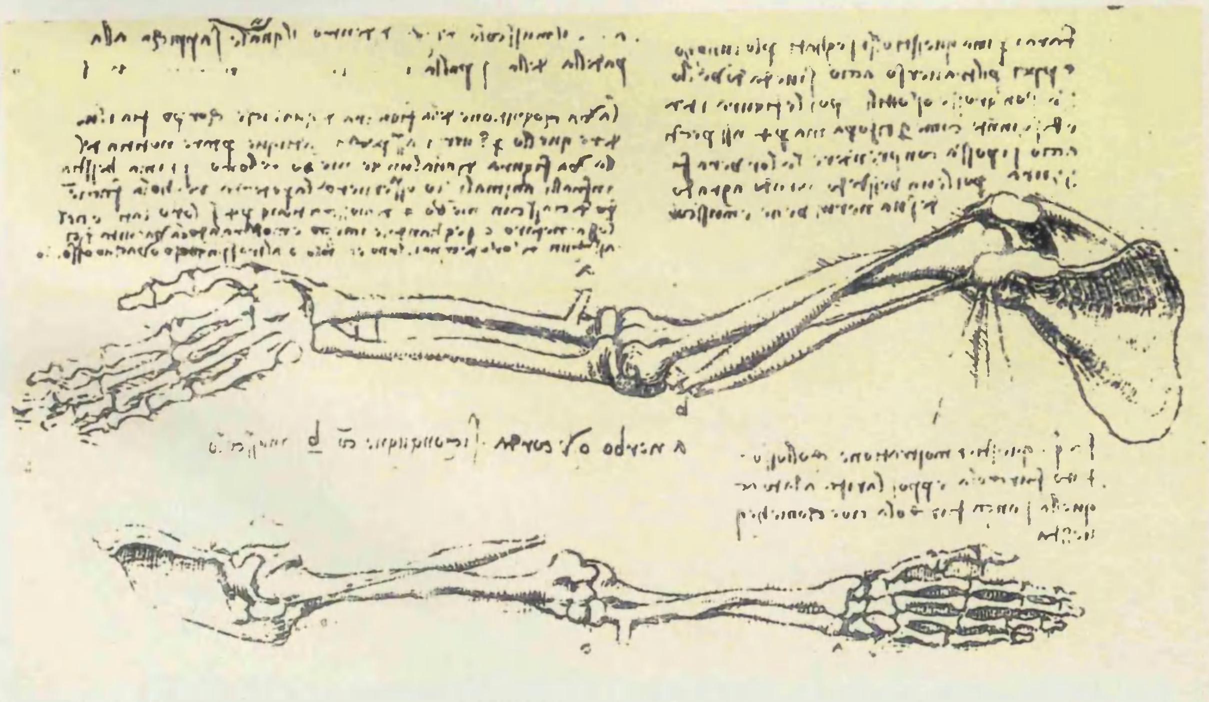

Plate 2. Bones of the arm in supination and pronation, with scapula and bicep *by Leonardo da Vinci*

Dedicated to my parents Philip and Shirley,
and my brother Peter.

A STUDY OF SCATTERED X-RAY RADIATION IN BONE DENSITY MEASUREMENT

Michael Joseph Mooney

University College London

Submitted for
The Degree of Doctor of Philosophy
The University of London

December 1992

Abstract

Various aspects of scatter in bone density measurement are studied. Firstly the detrimental effects of scatter in photon absorption bone mass measurements are assessed, and secondly, the use of scatter as a source of information about bone density is studied and a Compton scatter densitometry (CSD) system described. The detrimental effects of multiply scattered photons in CSD are also investigated.

Photon absorption techniques are frequently used to carry out bone mass measurements. The dual energy analysis used to process the data depends upon scatter-free detector signals. In practice, the detector and source collimation produce high levels of scattered radiation in the detected signal. An analysis of this problem using Monte Carlo based photon transport computer studies is presented. The results indicated that current systems are reasonably insensitive to the scatter contribution except where patient changes occur over a long series of measurements, or where new results taken with dual energy x-ray absorptiometry (DEXA) systems are compared with those taken on older systems such as dual photon absorptiometry (DPA). Inclusion of scattered radiation in the calculation of bone mass can lead to a 0.5% to 3.5% reduction between system types. Patient size changes could lead to a reduction in bone mass of 0.5%[a] to 1.0%[b].

The use of Compton scatter to determine bone density has been described. Experimental and computer simulated data have been used to determine an optimum operating energy of 120 kV_p and an exposure time of 30 s. The detrimental effects of multiple scatter were reduced by the use of energy windows. The remaining effects were corrected by correction factors calculated over a range of measurement sites for the apparatus geometry. Density measurements made over a range of phantoms produced reproducible results with a CV of less than 1%. An effective dose value of 6.9 μSv was found for a femoral neck measurement.

Comparisons of CSD measurements were made with other established bone density measurement techniques. These were found to correlate very well with r=0.90 for quantitative computed tomography and r=0.95 for DEXA.

---

[a] Femoral neck measurement.

[b] Lumbar spine measurement.

Errata

p.38	line 25	radiation can recorded... *should read* radiation can be recorded...
p.40	line 4	NaI... *should read* NaI(Tl)...
p.40	Figure 2.2	gd-153... *should read* Gd-153...
p.41	Figure 2.3	x-ray source *should read* x-ray source filtered with 0.6 gcm^{-2} samarium
p.42	line 27	NaI... *should read* NaI(Tl)...
p.45	line 20	Gadolinium... *should read* gadolinium...
	line 21	Germanium... *should read* germanium...
	line 26	Samarium... *should read* samarium...
p.51	line 28	interaction are... *should read* interaction is...
	line 30	since they retain their... *should read* since it retains it's...
p.67	line 7	equ.4.1 $\rho = \rho_e(Z/A)_{eff}N_A$ *should read* $\rho_e = \rho(Z/A)_{eff}N_A$
p.73	line 29	Density measurements were found to be... *should read* The error in the density measurements was found to be...
p.74	line 2	NaI... *should read* NaI(Tl)...
p.81	line 2	using calculus can found... *should read* using calculus can be found...
p.97	line 7	trochanter was also used a landmark... *should read* trochanter was also used as a landmark...
p.106	line 11	as kerma During... *should read* as kerma. During...
p.126	line 11	this would only valid... *should read* this would only be valid...
p.152	line 5	which were not... *should read* which had not...

Contents

Figures

Chapter 1.

Chapter 2.

Chapter 3

Chapter 4

Chapter 5

Chapter 6

Appendix 1

Tables

Chapter 1

Chapter 2

Chapter 3

Chapter 5

Acknowledgements

I would like to thank Dr. Robert Speller for his supervision and encouragement over the duration of this project and, especially, to Sharmila, Gary, Mike, Nia, Cephas, Arnie and Mercedes for their daily friendship and suggestions.

Thanks also to Ian Cullum for his helpful suggestions and advice, and the Institute of Nuclear Medicine for the use of the Hologic QDR 1000/W. Thanks also to the CT Scanning Unit at University College Hospital for the use of the CT machine, and to Julie Horrocks at St. Bartholomews Hospital for advice and the use of the TLD chip dosimeters.

I must also thank Sam and Helen for their encouragement and being great flat-mates.

Finally, I must thank my parents whose efforts and constant support have enabled me to complete seven years of study at university.

Chapter 1.

Introduction and review

1.0 Introduction

Bone densitometry is the measurement of bone density used in the diagnosis and management of many bone diseases including osteoporosis. This thesis examines various effects of scattered x-ray radiation on bone density measurement techniques. The two most widely used methods of bone densitometry are based on dual photon absorptiometry theory which does not account for secondary x-ray photons scattered into the detected beam by the subject of the examination. The first part of the thesis contains Monte Carlo based computer simulations of these two dual photon absorptiometry techniques, modelled with different clinically relevant measurement sites. Tracing of the photon histories allows the primary and secondary photons to be separated and their effects assessed. Bone density screening programs require regular measurements over a long time period and consequently patient size changes are also modelled. Results from all the simulations are presented and the effects of scatter on these bone density measurements are discussed.

The second part of the thesis describes how scatter can be used as a source of information about bone density. The development of a measurement system which utilises the density dependence of Compton scattered x-ray photon intensity is described. Results of density measurements on various bone substitute and bone-tissue-containing phantoms, and on a simulated patient are presented. A Monte Carlo simulation of this Compton scatter densitometry system was made to calculate correction factors for multiply scattered x-ray photons in the detected beams. Measurements of the absorbed dose that would be received by patients during a typical scan were also made. A comparison of these results with results from measurements made on other current clinical bone density measurement systems is shown.

This chapter will describe the general anatomy of bone, especially at three clinically relevant sites, and the changes in bone associated with normal aging and with the disease state. A more detailed description of osteoporosis is included here, as this is pertinent to the main aim of the thesis. A review of current measurement techniques is also presented.

1.1 General Anatomy of Bone

Bone is an organ that provides several essential functions such as; form to the body, protection to internal organs, locomotion and many biochemical and metabolic functions. Bone tissue consists of a complex collagen fibre matrix embedded with various minerals in high concentrations. Mature bone mineral is predominantly hydroxyapatite (HDA), $3\text{-}Ca_3(PO_4)_2Ca(OH)_2$, in various degrees of hydration, together with small amounts of magnesium and traces of sodium and fluoride. Bone is a metabolically active tissue, continually being formed and resorbed by bone cells whose activity can be modified by many factors including disease.

Bones are classed as either long, short, flat or irregular in shape. This thesis primarily considers long bones and also vertebrae (classed as short bones).

A typical long bone is composed of the central diaphysis, the metaphysis where growth occurs, and the epiphysis. The outer surface of the bone is a hard dense tissue known as cortical (compact) bone which contributes approximately 80% of the skeletal mass. Cortical bone forms a strong outer sheath which encloses the trabecular (cancellous) bone. Trabecular bone consists of narrow fibres and lamellae which join to form a reticular structure which braces and strengthens the bone. This structure enables the long bones to withstand the large stresses imposed from bearing weight and from movement. The relative quantity of compact and cancellous bone varies from bone to bone and also within a bone. Marrow tissue is contained within the bone cavities and in the trabecular structure spaces. In infancy this marrow is red, contains haematopoietic cells, and is 75% water. As aging occurs this red marrow retreats to the bone ends and is gradually replaced by yellow marrow which consists of

96% fat (Gray, 1988).

1.1.1 Anatomical sites of interest : the forearm

The forearm is made up of two parallel bones, the ulna and radius. The ulna is prismatic in form and gradually narrows from the top down to the wrist joint. The radius is shorter than the ulna and gradually widens from the top down to the wrist where it makes up the bulk of the wrist. The radius is distal and the ulna is proximal.

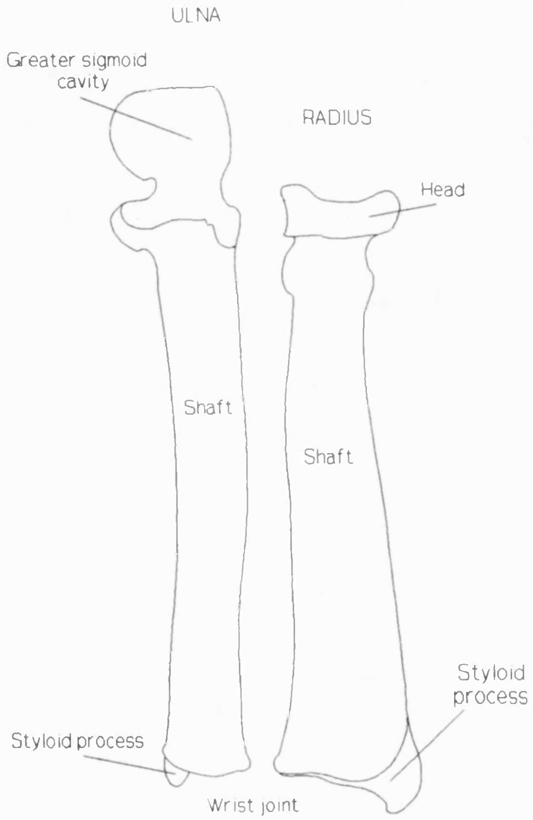

Figure 1.1 Schematic anterior view of radius and ulna.

1.1.2 The lumbar spine

The lumbar vertebrae are the largest segments of the spinal column.

There are five lumbar vertebrae which are situated between the dorsal vertebrae and the sacrum to form part of the anterior convex curve of the spine. A lumbar vertebra is characterised by a large body which is roughly elliptical in section with spinal and transverse processes attached. The body comprises of trabecular bone covered with a thin coating of cortical bone, whereas the arch and processes are almost completely cortical bone. The vertebrae are separated by lenticular discs of intervertebral substance which consists of fibrous tissue and fibro-cartilage laminae, surrounding a soft pulpy centre.

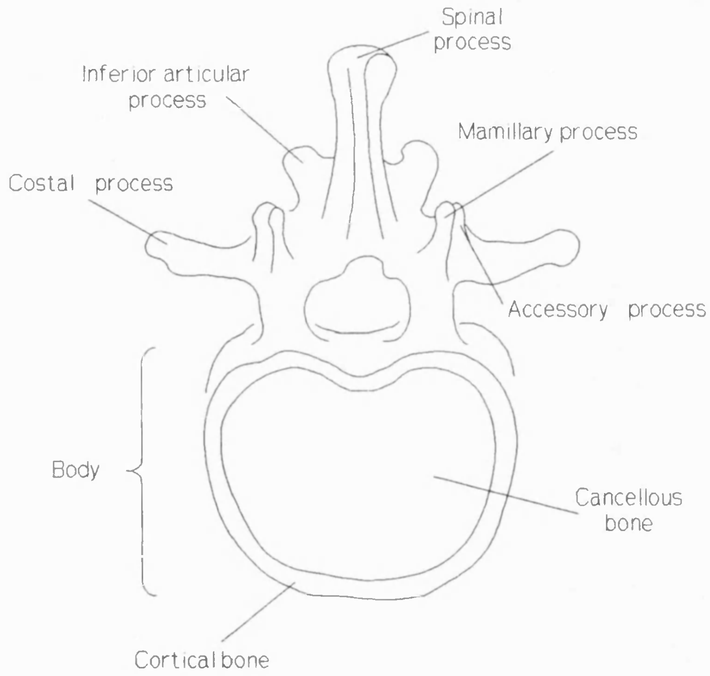

Figure 1.2 Schematic superior view of a lumbar vertebra.

1.1.3 The femur

The femur forms the upper leg and is the longest and strongest bone in the body. The upper extremity consists of a head, a neck and a greater and lesser trochanter. The head is articulated with the os innominatum, and the neck joins the head with the shaft of the femur. The trochanters are prominent bone processes which function as muscle attachment points. The femoral shaft is a cylinder of cortical bone which is narrowest in the middle region and widens at the extremities. As the bone widens the shaft walls become thinner as the bone divides into layers to form trabecular bone. The arrangement of the trabeculae is highly structured in the upper end of the bone and is essential for the bone to withstand the stresses of weight bearing and muscle traction. In the head of the bone the planes of the trabeculae are curved to withstand pressures induced from body movement in any direction.

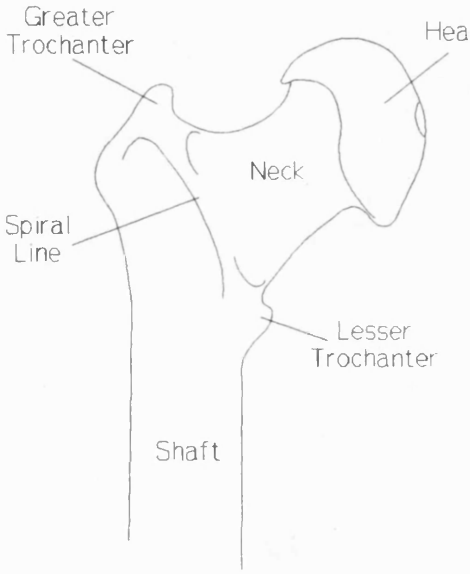

Figure 1.3 Schematic anterior view of right upper femur.

1.2 Normal bone changes

As aging occurs bone mass is gradually lost from the body. This is a universal phenomenon occurring in both sexes, in all races and from pre-history to the present day. Skeletons in neolithic long-barrows have been shown to have suffered age-related bone loss (Woolf & Dixon, 1988).

Although the composition of bone remains relatively constant among normal subjects (Dequeker, 1973), there is a general decrease in the amount of trabecular and cortical bone in the body as aging occurs. The cortical bone becomes thinner and more porous while there is thinning and even some loss of trabeculae from the trabecular bone. The loss of bone together with the conversion of red marrow to the less dense yellow marrow produces an overall drop in bone density. The effects of bone loss are more apparent in women than in men. Women have a lower peak bone mass and a greater aging loss rate than men (Nilas and Christiansen, 1987). Premenopausal women have approximately 15% less compact bone, corrected for bone size, then men. As aging occurs this difference becomes more pronounced. Bone loss is mostly influenced by age and declining ovarian activity but is also affected by race, heredity, physical activity and diet. In the premenopausal years trabecular bone loss seems to exceed cortical bone loss although the age at which this begins is not known. Riggs *et al* (1982) believe that trabecular bone loss is linearly related to age, whereas Krølner *et al* (1980) believe that trabecular loss is accelerated after menopause. More recently Hansson and Roos (1986) show that there is no clear acceleration of bone loss around menopause. Reported rates of bone loss in normal subjects, using various measurement techniques, show a large variation. Riggs *et al* (1981), Krølner and Nielsen (1982), Riggs *et al* (1982) and Riggs *et al* (1986), Hansson & Roos (1986), all measured the rate of bone loss and reported no accelerated loss after menopause. More recent investigations, Cann *et al* (1985) and Pacifici *et al* (1987), using different measurement techniques, report a greater loss rate after menopause. Hedlund and Gallagher (1989) found a three-fold decrease in bone mineral density (BMD) at the femoral neck and a ten-fold decrease in the trochanteric region in the first 6 years of menopause compared with pre-menopause loss rates. They propose that the early post-menopause years are the most critical years as there is a 17% BMD decrement in the femoral neck and a 36% decrement in the trochanteric region during this period. Block *et al* (1989) conducted a quantitative computed tomography (QCT) study of trabecular bone mass and found a small loss of trabecular bone in premenopausal women with a continuation of bone loss through old age following a rapid loss at menopause. Nilas and Christiansen (1987) demonstrate characteristic menopausal hormone changes coinciding with biochemical signs of increased bone turnover with a significant drop in fore-arm and spinal bone mass.

Compston *et al* (1988) show that bone loss rates also depend on the geographical location of the subjects, although Pocock *et al* (1988) propose that ethnic group is the significant factor rather than population centre. A summary of the reported loss rates in normal women, measured with various techniques, is shown in table 1.1.

1.3 Disease related bone changes

The normal growth and remodelling of bone is dependent on many physical and physiological factors apart from aging. Changes in bone mass can occur for a variety of reasons. These include deficiencies in key elements such as calcium, phosphate and fluoride. Hormonal deficiencies are associated with low bone mass and sex hormones are especially relevant in this circumstance. Mechanical bone loading is an important factor in maintaining strength and mass, and long periods of immobilisation or weightlessness cause rapid loss of bone mass.

Metabolic diseases of the bone are usually characterised by a marked decrease in bone mass. Osteomalacia is a failure of mineralisation in the bone matrix leading to a decrease in bone density. Hyperparathyroidism, myeloma and metastatic cancer, renal failure (renal osteodystrophy) and osteoporosis all result in a loss of bone mass. Paget's disease is characterised by excessive bone resorption coupled with greatly increased bone formation, and leads to an overall increase in the bone density.

1.4 Osteoporosis

Osteoporosis is the commonest disease of the skeleton and is characterised by a lower bone mass than would be expected for the subject's age and sex. This leads to a greatly increased chance of bone fracture which is usually the first indication of the disease. Clinically there are two types of osteoporosis; senile osteoporosis which is the age-related loss of bone mass, and post-menopausal osteoporosis which is the accelerated loss of bone mass after menopause. Both types of osteoporosis are usually described together as involutional osteoporosis. Mazess *et al* (1988) state that a 10% decrease in BMD increases the risk of bone fracture by 2 or 3 times. They have demonstrated that a 30-35% decrement of BMD in the spine and a 45% BMD reduction in the femoral neck is common in osteoporotic patients. This manifests as a risk of fracture 20-30 times greater than normal young women and 10-20 times greater than age-matched controls. DeSimone *et al* (1989) report that hip fracture is less likely in black women than in white women and that osteoporosis is less common in obese than non-obese women. Skeletal examinations have shown that black women generally have a higher bone density than age-matched white women. They summarise that bone mass density is increased with body weight at all sites for black and white women and that BMD is decreased with age at all sites for black and white women independently.

Long bone fractures in elderly patients have serious effects in both human and economic terms. Femoral fractures often require surgery with an accompanying increase in morbidity and mortality. A long hospital stay is usually required together with physiotherapy and after-care. Serious fractures can remove the independence of elderly people and place the burden of care on relatives and the community. In 1988, Balseiro *et al* reported that hip fractures in the United States cost health services greater than US$7 billion *per annum*.

Although it is necessary to measure bone strength in order to assess fracture risk, this is at present impossible *in vivo*. Bone mass and bone strength are highly correlated (Speller *et al*, 1989) and measuring bone mass is at present the best available indicator of fracture risk.

Osteoporosis usually becomes apparent when a fracture of the affected bone occurs. The commonest sites for these fractures are the vertebral bodies which suffer crush fractures, the distal radius and the femoral neck which usually fracture as a result of trauma.

Riggs *et al* (1982) showed that osteoporosis affects a large subset of early post-menopausal women who exhibit an increased rate of bone loss in addition to the normal bone loss. Thomsen *et al* (1986) went on to show that this could be attributed to oestrogen deficiency having a negative effect on the skeleton. A summary of loss rates in osteoporotic women is shown in table 1.1. Trabecular bone is nine times metabolically more active than cortical bone which indicates that demineralisation will be faster in trabecular bone (Parfitt, 1983). Riggs *et al* (1981) showed that trabecular bone is a better indicator of osteoporosis than cortical or total bone.

Some researchers have hypothesised the existence of a fracture threshold, which is a value of BMD or bone mineral content (BMC) below which fractures due to low trauma will occur. Hansson and Roos (1986) show that vertebral compression fractures with a minimal trauma was apparent when the BMC fell below 3.08 g/cm.

Thus, the early detection of osteoporosis requires a measurement technique which can detect long term losses in bone density with a precision of <1% during longitudinal studies and which would ideally measure the bone density in the trabecular region only.

Normal Percentage Loss Rate [per year]	Osteoporotic Percentage Loss Rate [per year]	Measurement Technique	Measurement Site	Number of Subjects	Authors
1.1		SEQCT	L_1-L_3	129	Compston *et al* (1988)
1.14	1.62	SEQCT	T_{12}-L_3	133	Pacifici *et al* (1987)
1.03	1.17	DEQCT	T_{12}-L_3	133	
1.2	39% mean decrement	SEQCT	T_{12}-L_3	203	Cann *et al* (1985)
1.32 † ¶		DPA	L_1-L_4	139	Riggs *et al* (1987)
0.97 ‡ ¶		DPA	L_1-L_4	139	
0.58		DPA	L_1- L_4	123	Riggs *et al* (1982)
0.81		DPA	Femoral Neck	123	
1.4 ‡	4.4 *and* 16% mean decrement	DPA	L_2-L_4	70	Krølner & Nielsen (1981)
0.68	19.6% mean decrement	DPA	L_1-L_4	105	Riggs *et al* (1981)
~1.1 ‡	20% mean decrement	DPA	L_2-L_4	13	Krølner *et al* (1980)

† - Pre-menopausal loss rate
‡ - Post-menopausal loss rate
¶ - Not statistically different

SEQCT - Single Energy Quantitative Computed Tomography
DEQCT - Dual Energy Quantitative Computed Tomography
DPA - Dual Photon Absorptiometry

T_{12}-L_3 is the region from the 12th thoracic vertebra to the 4th lumbar vertebra.

Table 1.1 A summary of normal and osteoporotic bone loss rates.

1.5. Measurement techniques

This section describes the development and current status of bone mass measurement.

1.5.0 Conventional radiographs

As bone mass decreases the vertebral bodies become gradually more transparent to x-rays. As vertebral osteoporosis develops there is a loss of density in the centre of the vertebrae and this is apparent in an x-radiograph. Kruse and Kuhlencordt (1983) developed a spinal index based on radiolucency and bone deformation to grade bone mass loss and Kleerekoper *et al* (1985) graded the change in shape of the vertebral body.

Empirical indices, such as the Singh index, have been used to grade the trabecular pattern within the proximal femur which indicates the loss of structure within the trabecular bone. However, this technique has proved not to be a reliable indicator of bone mass loss.

1.5.1 Radiogrammetry

A simple measurement of the cortical volume of a bone section can be made by taking measurements of the cortical thickness from x-radiographs. These radiographs have to be of good quality using a fine grain x-ray film and without using fluorescent screens. Metacarpal bones are most commonly considered and the cortical volume is reported to correlate well with the amount of bone present (Barnett and Nordin, 1960). The main drawback of radiogrammetry is that the measurement is performed on peripheral bones and may not be representative of a site of greater clinical interest e.g. the femoral neck. There are also difficulties in repositioning for serial measurements which can lead to poor long-term precision.

1.5.2 *In Vivo* Neutron Activation Analysis (IVNAA)

This technique involves the irradiation of the whole body with moderated fast neutrons. Calcium-48 is converted to radio-active calcium-49 which then decays by γ-ray emission with a half-life of 8.8 minutes. By detecting the γ-ray emission, a measurement of the total calcium content in the body can be made and hence the total skeletal mass.

However this technique is limited to the few centres equipped to perform total body irradiation. Another major drawback is the very high dose received by the patient which excludes this technique from long-term screening. Although IVNAA shows good precision it has poor accuracy as it cannot distinguish between bone and other calcium containing tissues.

1.5.3 Quantitative Computed Tomography (QCT)

In quantitative computed tomography (QCT) an image of a thin transverse slice of the body is produced by taking x-ray profiles at various orientations around the patient. A reconstructed image can then be displayed on a computer. A CT number is assigned to each pixel comprising the image and an excellent correlation exists between the pixel CT value and the linear attenuation coefficient of the imaged tissue (Speller *et al*, 1981). At the x-ray energies used in CT the majority of the photon interactions are due to Compton scattering and so the linear attenuation coefficients will be those associated with the Compton interaction. Therefore the measured attenuation values will be dependent on the physical density of the tissue. A comprehensive review of this technique in bone density measurement is given by Cann (1988).

One of the main advantages of QCT is the ability to select the trabecular bone independently of the cortical bone. The mean CT value within a selected region can be calculated and compared with carefully selected calibration materials. The BMC can then be calculated by interpolation. The usual site for measurement is the lumbar spine between L_1 and L_4, although measurements have been made on the femoral neck (Sartoris *et al*, 1986) and also on the distal radius (Ruegsegger *et al,* 1981 & 1984).

One of the inherent errors in QCT is the relocation of the measurement site in 3-D space during serial measurements although recent improvements in image data manipulation software has greatly reduced this error. Age-related conversion of red to yellow marrow produces a large error into the BMC calculation although the use of dual energy QCT can reduce this significantly (Pacifici *et al,* 1987). As the image is produced by a polychromatic x-ray source, corrections must be made for beam hardening and non-exponential attenuation. Scatter of the x-ray beam is also a source of error especially from the cortical bone regions.

Although QCT provides a reliable measure of BMC it has the drawback of being a relatively high dose technique (see table 1.2), especially from dual energy scans, which would exclude QCT from long term screening programs. A second drawback is the high cost of QCT and the heavy workload of clinical CT departments.

1.5.4 Compton scattering

Compton scattering has the same ability as QCT to distinguish between trabecular and cortical bone. A clinical system for bone density measurement has been described by Webber and Kennett (1976). The intensity of Compton scatter depends on the electron density of the target material, which in turn is dependent on the physical density of the target. To measure the density a finely collimated x-ray beam and a finely collimated detector are placed either side of the target. A critical volume is formed where the two beam cones coincide, and it is the density of the material within this volume which is finally measured. To compensate for the variation in tissue thickness around the critical volume two x-ray beams and two detectors are used to measure the density (Koligliatis, 1990). The detectors record either the transmitted count or scattered count from each source in turn when the critical volume is correctly positioned within the trabecular bone region. The density is proportional to the square root of the scatter to transmitted ratio and the final bone density value must be corrected for multiple scatter effects (Speller and Horrocks, 1988).

This method forms the basis of much of the work presented in the second part of this thesis. A fuller description of the technique and the results from new measurements and computer simulations are presented in chapters 4 and 5.

1.5.5 Photon absorptiometry

Radiographic methods of bone mass measurements are subject to poor precision because of the variable conditions under which radiographs are processed. In photon absorptiometry these problems are largely overcome. Unlike QCT and Compton scatter, however, photon absorptiometry measures the whole bone mineral content within the radiation beam i.e. the trabecular bone region cannot be specifically selected. The advantages of photon absorptiometry are it's accessibility, low cost and relatively low radiation dose, while still providing good precision and accuracy. For these reasons it has become the most widely used method of bone density measurement.

Consideration of the effects of scattered radiation during photon absorptiometry measurements form a large part of this thesis. A fuller description of the technique and the results of scatter measurements and simulations with their associated effects on bone density are presented in chapters 2 and 3.

1.5.5.0 Single Photon Absorptiometry (SPA)

Cameron and Sorenson (1963) describe a method of bone mineral measurement by photon absorption based on the law of exponential attenuation called single photon absorptiometry (SPA). A highly collimated beam of γ-ray photons from an isotope source is measured by a collimated detection system. This is usually an energy sensitive detector such as a scintillation detector. The beam is traversed across the measurement site to provide attenuation measurements through soft tissue only and soft tissue containing bone. To correct for differences in soft tissue thickness the measurement site is submerged in water which provides a constant thickness soft tissue equivalent. Consequently measurements are usually made on the radius and ulna bones in the fore-arm. However this site is not considered to be representative of the axial skeleton sites where the effects of osteoporosis are more clinically relevant (Mazess *et al*, 1984). Large variations in the distribution of trabecular bone in the radius and ulna also makes this site very susceptible to repositioning errors.

1.5.5.1 Dual Photon Absorptiometry (DPA)

Dual photon absorptiometry (DPA) is similar in principle to the SPA technique, but in this case the radiation beam contains two distinct photon energies. These are produced from either combined isotope sources or from dual energy emitting sources. Transmission measurements are made with an energy sensitive detector and the transmitted counts separated by electronic windowing or by dual detectors.

A dual energy analysis proposed by Roos and Sköldborn (1974) removes the effect of soft tissue[c] thickness variation. Submerging the site in water is unnecessary and measurements can be made on any relevant site on the body. The beam is scanned across the bone and the bone mineral content (BMC) expressed in grammes. The BMC can be divided by the unit width of the bone to give mass per unit length (gcm^{-1}) along the radiation path. More commonly though, an area of bone, or a region containing bone is scanned and the BMC divided by the bone area to give mass per unit area (gcm^{-2}) known as bone mineral density (BMD). Hansson *et al* (1980) show that BMC correlates better with disease severity than BMD. They also conducted biomechanical tests that demonstrated BMC found by DPA correlated well with spine strength. However, BMD has a lower precision error which is more suitable for longitudinal studies.

Commercial scanners are readily available and there is a large literature reporting on their performance in various aspects of *in vivo* and *in vitro*

---

[c] Soft tissue consists of adipose and muscle tissue.

performance. Some values for the precision, accuracy and dose are quoted in table 1.2

As photon absorptiometry integrates the transmission through the thickness of the measurement site it is susceptible to errors from extraosseous tissue variations. Bone mass may be exaggerated osteoarthrosis, extraosseous calcification notably aortic calcification, and vertebral compression fractures. One or two fractures in the L_2-L_4 lumbar region increased BMD by an average of 3% in a 0% to 10% range (Pouilles *et al,* 1988).

DPA measurements are reliant on photon flux and attenuator thickness. Variation in the BMD attributable to the source strength has been variously reported (Dunn *et al,* 1987; Shipp *et al,* 1988; Dawson-Hughes *et al,* 1989). These have been attributed to systematic errors in the software algorithms and is especially marked for weak sources and thick attenuators. This source of error has not been entirely eliminated by software revision.

Gotfredsen *et al* (1988) have reported poorer BMD precision than expected due to miscalculation of the bone area by edge detection routines which try to exclude bone processes in the lumbar spine.

1.5.5.2 Effects of fat on DPA measurements

Mazess *et al* (1989) conducted a series of *in vitro* experiments showing the variation of BMC with the proportion of fat in marrow tissue. BMC was found to be correct when fat to marrow ratio was 2:1 which is the normal *in vivo* ratio. Halving the fat content produced a 5% overestimate of HDA content and a 5% underestimate of HDA when fat content was doubled.

QCT and dual energy x-ray absorptiometry (DEXA, §1.5.5.3) evaluations of BMC are also susceptible to fat content variation errors. A 10% change in BMC for every 100 mg/cm^3 of fat change is reported (Mazess *et al,* 1989), in QCT at 120 kV$_p$. This is double the magnitude of the DEXA evaluation.

Gotfredsen *et al* (1988) relate that extra and intravertebral soft tissue composition has an important effect on the accuracy of DPA lumbar bone mass measurements. Wahner *et al* (1985) by successively extracting fat from vertebrae that a 10% change in intraosseous fat produces a 0.6% error in BMC. Roos *et al* (1980) report the fat content of the kidney capsules introduce a non-systematic inaccuracy lumbar measurements. Hansen *et al* (1990), demonstrate the influence of fat both inside and outside the bone give BMD errors. They show a 10% change in marrow fat produces a 1% change in BMD. They also show that DPA was less susceptible to absorber thickness errors than the new DEXA technique, which suggest that DEXA may be prone to error from abdominal gas and other tissue inhomogeneities.

1.5.5.3 Dual Energy X-ray Absorptiometry (DEXA)

A recent development in dual-photon absorptiometry has been the introduction of dual energy x-ray absorptiometry (DEXA). This method also involves a dual energy analysis but the γ-ray source has been replaced by a polychromatic x-ray tube source. The dual energy components of the beam are produced either by k-edge filtering or by kV_p switching. An x-ray tube source produces a far higher photon output with a subsequent improvement in counting statistics. Collimation of the beam can be made finer which gives better spatial resolution and hence improves accuracy (Mazess *et al,* 1988). An energy discriminating detection system is required for the k-edge filtered beam but is not required for the kV_p switched beam.

DEXA has shown improved precision over DPA systems (Cullum *et al,* 1989; Mazess *et al,* 1988) and looks set to become the new standard of BMC measurements. However, like all photon absorptiometry techniques there are still inherent errors to be overcome such as scattered radiation and the uneven distribution of fat around the measurement sites (Tothill *et al,* 1988).

Measurement Technique	Measurement Site	*In Vivo* precision [% CoV]	*In Vivo* accuracy [% CoV]	Dose to Subject
Radiographic	various			<1 mSv
Radiogrammetry	metacarpals spine	7.25 5.74 [Barnett & Nordin, 1960]		~0.4 mSv
In Vivo Neutron Activation Analysis	whole body	2.9	1.5	2.8 to 20 mSv † [Cohn *et al*, 1972] [Nelp *et al*, 1970]
SEQCT	lumbar vertebrae	>1	6 to 9	10 mSv
DEQCT	lumbar vertebrae	3	3 to 6 [Cann *et al*, 1988]	20 mSv
Compton scattering	lumbar vertebrae	1 to 3 [Webber & Kennett, 1976]		0.1 mSv
SPA	forearm	1 to 2 [Christiansen & Rødbro, 1977]	2 to 4	50 μSv
DPA	lumbar vertebrae	1.3 to 1.5 [Krølner & Nielsen, 1980]	1 to 2.5 [Peppler & Mazess, 1981]	0.15 mSv
DEXA	lumbar vertebrae	>1 [Cullum *et al*, 1989]		0.11 mSv

† - radiation weighting factor of 10.

SPA - Single Photon Absorptiometry
SEQCT - Single Energy Quantitative Computed Tomography
DEQCT - Dual Energy Quantitative Computed Tomography
DPA - Dual Photon Absorptiometry
DEXA - Dual Energy X-ray Absorptiometry

Table 1.2 Summary of bone density measurement techniques.

Chapter 2.

Simulation of scatter effects in Photon Absorptiometry

2.0 Introduction

DPA is currently the most common form of bone mineral measurement although DEXA systems are rapidly gaining popularity. During DPA, a highly collimated dual-energy γ-ray beam is traversed across the measurement site and the subsequent attenuation measured by an energy sensitive detector. The measurement site is assumed to be made up of two components; soft tissue surrounding a bone. The number of transmitted photons, of each of the two energies, depends on the attenuation coefficients and thicknesses of the tissues. Measurement of the dual-energy beam transmission can be used to calculate a value for bone mass M_b using a dual energy analysis. Roos and Skøldborn (1974) first proposed an analysis based on the exponential law of attenuation (equation 2.1):

$$I - I_o \, e^{-\mu m} \qquad 2.1$$

2.0.0 Dual energy analysis

In a patient or phantom there will usually be a layer of fat and soft tissue surrounding the bone. Although the basic theory only assumes two tissue components this analysis can account for the contribution of fat tissue if the fat is evenly distributed. Assuming that the beam passes through all three types of tissue then:

Solving equations 2.2 and 2.3 for m_b gives

$$I^l = I_o^l\, e^{-\mu_s^l m_s}\, e^{-\mu_f^l m_f}\, e^{-\mu_b^l m_b} \tag{2.2}$$

$$I^h = I_o^h\, e^{-\mu_s^h m_s}\, e^{-\mu_f^h m_f}\, e^{-\mu_b^h m_b} \tag{2.3}$$

$$m_b = \frac{\mu_s^h \ln\left(\frac{I_o^l}{I^l}\right) - \mu_s^l \ln\left(\frac{I_o^h}{I^h}\right) - \left(\mu_s^h \mu_f^l - \mu_s^l \mu_f^h\right) m_f}{\left(\mu_s^h \mu_b^l - \mu_s^l \mu_b^h\right)} \tag{2.4}$$

where

I	transmitted intensity with bone
I_o	transmitted intensity without bone
$\mu_f\ \mu_s,\ \mu_b$	mass attenuation coefficients of soft tissue, fat and bone [cm^{2}g^{-1}]
$m_f\ m_s,\ m_b$	mass of material in radiation path [gcm^{-2}]

symbols with a superscript *h* are for the high energy beam component

symbols with a superscript *l* refer to the low energy beam component

Equation 2.4 can be further simplified by introducing three more constants

$$D_{sb} = \mu_s^h \mu_b^l - \mu_s^l \mu_b^h \tag{2.5}$$

$$D_{sf} = \mu_s^h \mu_f^l - \mu_s^l \mu_f^h \tag{2.6}$$

$$N = \mu_s^h \ln\left(\frac{I_o^l}{I^l}\right) - \mu_s^l \ln\left(\frac{I_o^h}{I^h}\right) \tag{2.7}$$

From equation 2.4 a value for the bone mass m_b can then be calculated -

$$m_b = \frac{N - D_{sf} m_f}{D_{sb}} \tag{2.8}$$

For each point on the transverse scan the value of *N* is calculated and plotted. The presence of bone produces a positive increase in *N* which clearly delineates the bone. On either side of the bone where there is only soft tissue and fat then;

$$m_b = 0 \qquad 2.9$$

$\therefore$

$$N = D_{sf} m_f \qquad 2.10$$

A line drawn across the base of the bone contribution through the values of N, produced by soft tissue and fat only, defines an area A. The values of $D_{sb}m_b$ are found by subtracting the base line ($D_{sf}m_f$) from the values of N in the bone region. Integrating the area A above the base line and below the bone values of N produces a value which is related to the BMC by equation 2.11. This technique approximates the contribution of fat assuming the distribution of the fat is even. The positions of the base line and of area A are shown in figure 2.1.

$$A = \int_{p_1}^{p_n} D_{sb} m_b \, dx = D_{sb} \int_{p_1}^{p_n} m_b \, dx = D_{sb} M_b \qquad 2.11$$

where

A	area under N versus position curve [cm^3g^{-1}]
M_b	mass of bone along measurement path [gcm^{-1}]

2.0.1 Effect of scatter in analysis

This dual energy analysis assumes that the detected photon counts, I and I_o, are primary photons which have not undergone any scattering process. In a clinical bone densitometer this would not be the case. Instead, collimation of the detectors is such that a significant scattered radiation flux would enter the detectors, contributing to the signal that is used in the analysis to calculate the bone mass. Chapters 2 and 3 of this thesis describe the investigation and analysis of the magnitude of this effect and the consequent changes in bone density or mass that would be attributed to the patient. This has been accomplished by simulating various DP measurement systems and following individual photon histories using a Monte Carlo based computer model. This model allows photons to be classified according to their history and therefore primary and secondary radiation can be recorded separately. Section 2.2 briefly describes the Monte Carlo computer code.

During a clinical scan the detected signal, containing primary and secondary radiation, would have the effect of scatter reduced by calibration. However, if the calibration conditions differ from the clinical measurement conditions then errors will be introduced due to the change in the scatter component. Bone density measurements require serial measurements taken over a long time period during which a patient may significantly change in size, consequently altering the volume of tissue irradiated. Alternatively, if comparisons are made between different systems, the scatter effect will be different according to the irradiation geometry and photon source.

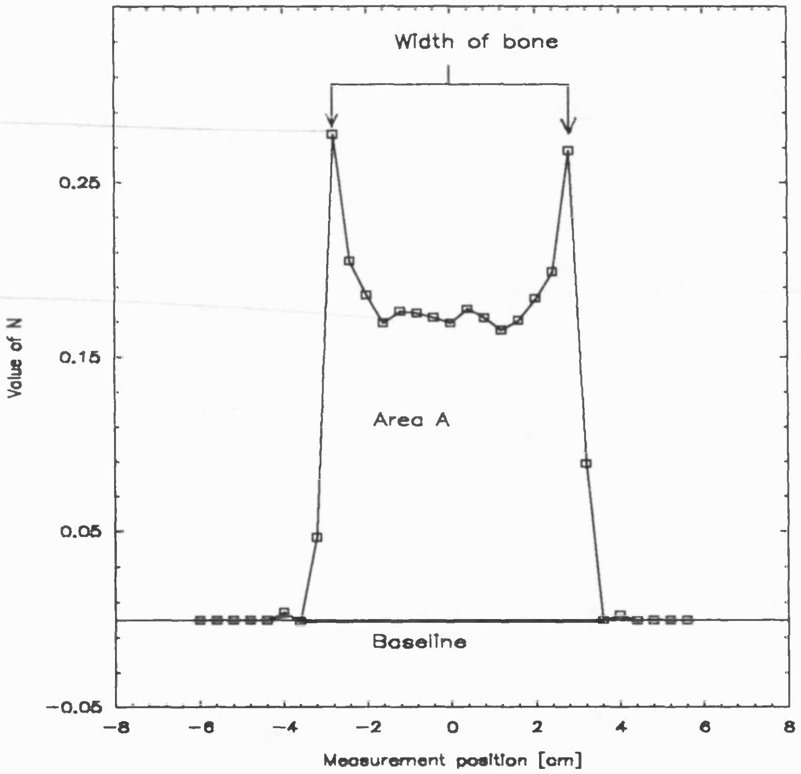

Figure 2.1 Shows an example plot of N versus scan measurement position. Also marked are the positions of the baseline and area A.

2.1 Computer simulation of DP systems

The program was designed to simulate a dual energy measurement on a femoral neck or lumbar spine site which are the two most clinically relevant measurement sites. The DPA simulation geometry was based on the Norland 2600 DPA scanner which uses a Gd-153 source, and the DEXA simulation was based on the Norland XR26 DEXA scanner which uses a k-edge filtered x-ray source and dual sodium iodide (NaI) (Tl) crystal detector. Schematic diagrams of the two systems are shown in figures 2.2 and 2.3.

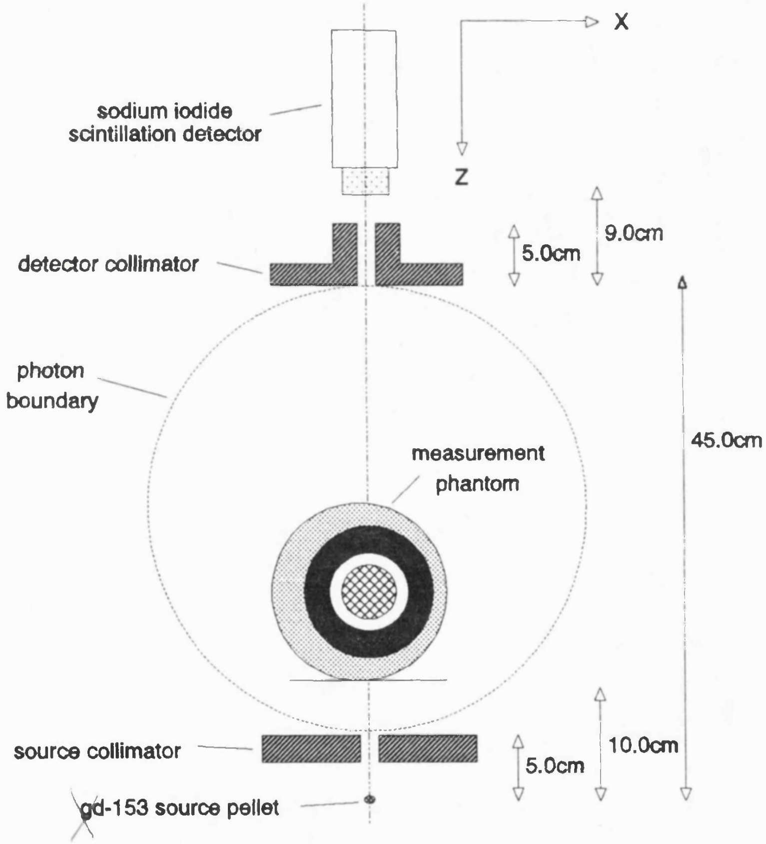

Figure 2.2 Schematic diagram of DPA measurement geometry used in the computer simulations. A four component leg phantom measurement site is shown.

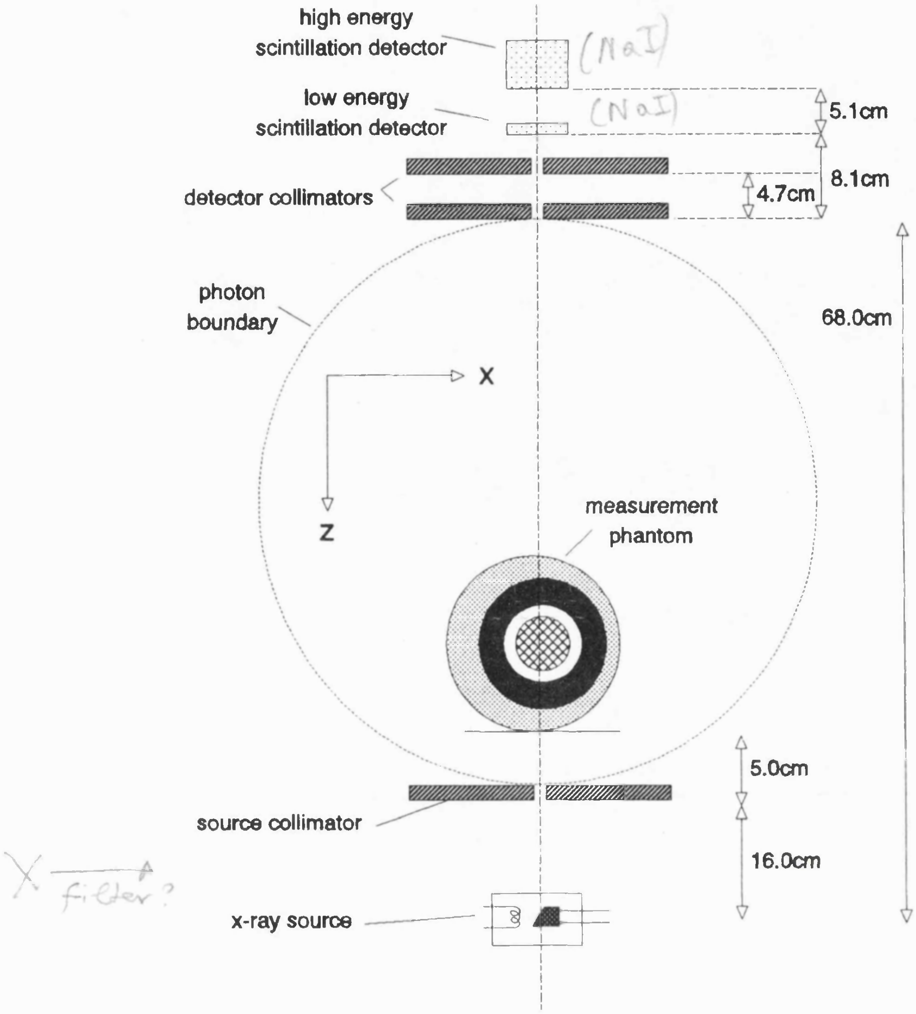

Figure 2.3 Schematic diagram of DEXA geometry used in the computer simulations. A four component leg phantom measurement site is shown.

By following the photon histories it was possible to produce values for I^l and I^h, and then separate the scattered photons from the true primary transmitted photons. Measurements of I_o^l and I_o^h were also made with the bone removed from the phantom models used in the simulation. Bone masses were calculated both with and without the scatter contributions and then compared. The thicknesses of the tissues surrounding the bone were varied to simulate changes in patient size and the proportion of fat to soft tissue was kept constant.

2.2 Program description

The basic principles of Monte Carlo simulations applied in medical radiation physics are reviewed by Raeside (1976) and Andreo (1991). The Fortran code used in the simulation employed the basic scattering and absorption routines from the PS3 code described by Koligliatis (1990). To simulate the densitometer scanning motion photons were traced from the source placed at 0.4 cm intervals across the measurement site, with the first point 6.0 cm to the left of the bone centre and the final point 6.0 cm to the right of the bone centre. At each point 2 x 10^6 photon histories were traced. Measurements beyond +6.0 cm or -6.0 cm were not necessary as no further useful information was gathered outside this range because of the narrow collimation of the photon beams.

Individual photons were traced from either the x-ray or the γ-ray source, through the source collimator, and into the measurement site phantom. Photons were tracked using cartesian coordinates and the direction of travel computed with direction cosines. The position and type of photon interaction was decided by random selection from attenuation data and relative interaction probabilities. The changes in energy and direction of the photons were calculated from random sampling of cumulative probability distributions (CPD). The CPD files were determined from the differential cross-sections of the relevant type of photon interaction.

After emerging from the phantom the photon history was followed until it reached a 'cut-off' perimeter at the same distance from the phantom as the detector collimator. If the photon was in front of the detector collimator face and within the angle of acceptance of the collimator it was scored as a detected photon. All detected photons were classified by energy and stored in arrays, they were then further divided into primary or scattered photons. In the case of the DEXA simulation a dual NaI crystal was used as the detector. A short routine was written based on exponential attenuation within NaI to determine if the photon was stopped in either the thick crystal or thin crystal. The thin crystal was positioned in front of the thick crystal and detected the low energy photons without impeding the high energy photons, which were finally stopped within the thick crystal. The photon was then scored appropriately. A flow-diagram summarising the program is shown in figure 2.4.

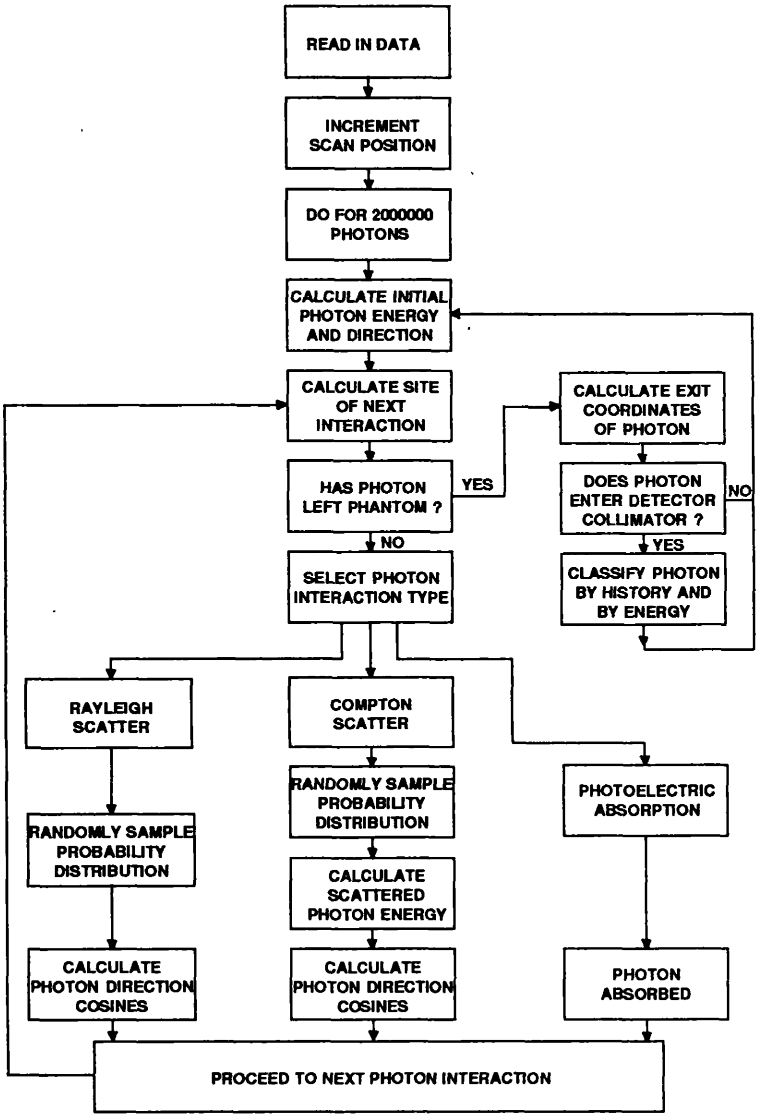

Figure 2.4 Pseudocode chart diagram showing main routines in the Monte Carlo photon absorptiometry computer simulations.

2.2.0 Compton scatter

In a Compton scatter event the incident photon is scattered by a weakly bound peripheral electron through an angle θ. The energy of the recoil electron and the scattered photon is dependent on the initial photon energy and the scattering angle. At x-ray energies in the diagnostic range most of this energy remains with the scattered photon (Barrett and Swindell, 1981). The Klein-Nishina formula for the differential cross-section of Compton events describes the probability of the initial photon being scattered into the solid angle $d\Omega$.

$$\frac{d\sigma}{d\Omega} = \left(\frac{r_o^2}{2}\right)\left(\frac{\lambda'}{\lambda}\right)^2\left(\frac{\lambda'}{\lambda}+\frac{\lambda}{\lambda'}-1+\cos^2\theta\right) \qquad 2.12$$

where

r_o^2	classical electron radius
λ	incident photon wavelength
λ'	scattered photon wavelength
θ	scattering angle

This interaction was simulated in the computer model using rejection sampling of the CPD derived from the Klein-Nishina equation. This method was described by Raeside (1976) and has been shown to give very good agreement with experimental evaluations of Compton scatter profiles. Testing of this routine has been described by Koligliatis (1990).

2.2.1 Rayleigh scatter

In a coherent scattering event the incident photon is scattered in a forward direction but retains the same initial energy. The coherent or Rayleigh scatter differential cross-section is a modification of the Thomson formula and is shown in equation 2.2. Form factors are introduced to account for the interference of the scattered waves from adjacent electrons.

$$\frac{d\sigma_{coh}}{d\Omega}(\cos\theta,\alpha,Z) = r_o^2\,F^2(x,Z)\,\frac{(1+\cos^2\theta)}{2} \qquad 2.13$$

where

r_o^2	classical electron radius
ζ	scattering angle
α	incident photon energy
Z	atomic number
F^2	form factor~~s~~ squared

and $x = 29.1445.\alpha.(1\text{-}\cos\theta)$

[29.1445 is a conversion factor for amu]

Rayleigh scatter is sampled from the CPD produced from the coherent scatter differential cross-section. Sampling this probability distribution with conventional rejection techniques has proved to be very inefficient. An improved method using an inversion-rejection technique described by Williamson and Morin (1983) has been used in the program.

2.2.2 Photoelectric absorption

Any photon which underwent a photoelectric interaction was assumed to be annihilated, and the photoelectrons produced were assumed to be locally absorbed. Any photon with an energy below 10 keV was automatically absorbed via a photoelectric interaction and the photon history terminated at that point.

2.2.3 Input data

For the DPA simulation the input spectral data was derived from a g~~G~~adolinium-153 source. The spectrum was measured on a planar high purity g~~G~~ermanium detector with a Canberra System 100 multi-channel analyser (MCA). The data was corrected for detector response and the calibrated channel data converted into a cumulative probability distribution.

For the DEXA model theoretical data for a 100 kV_p x-ray spectrum was taken from the HPA Spectral Data Catalogue (Birch *et al*, 1979). In the DEXA densitometer this beam is filtered with 0.6 gcm^{-2} of s~~S~~amarium to produce a k-edge filtered dual energy x-ray beam. Linear attenuation data for s~~S~~amarium taken from Storm and Israel (1970) was used in the exponential attenuation equation and multiplied with the spectral data to produce the final spectrum used in the program.

Both models used attenuation coefficient data calculated by the method of mixtures using coefficients from Storm and Israel (1970). Momentum transfer data and form factor data was calculated for the phantom component tissues using atomic form factors (Hubbell, 1969) and the method of mixtures. Tissue density values were taken from Woodard and White (1986). Interaction cross-sections were also taken from Storm and Israel (1970) for photoelectric absorption, Compton and Rayleigh scatter.

2.2.4 Measurement site phantoms

The measurement sites were represented by a series of different sized mathematical phantoms. These were based on two anthropomorphic tissue substitute phantoms which had been previously constructed in this department and are described in section 4.3. Two basic phantoms were used; a semi-infinite circular phantom containing the femoral neck and a lumbar spine phantom which approximated the geometry of the tissue substitute phantoms by using semi-infinite elliptical tissue segments. Both phantoms consisted of four components: an outer layer of adipose tissue, a thick layer of soft tissue and a bone consisting of cortical and trabecular bone. Schematic diagrams of both types of phantoms are shown in figure 2.5. Information on the elemental composition and densities of the four phantom components were taken from Woodard and White (1986). One of the aims of the simulation was to see the effect of changing patient size. To achieve this five different sizes were simulated for each of the two sites. A description of the different sizes modelled in the simulation appears in table 2.1.

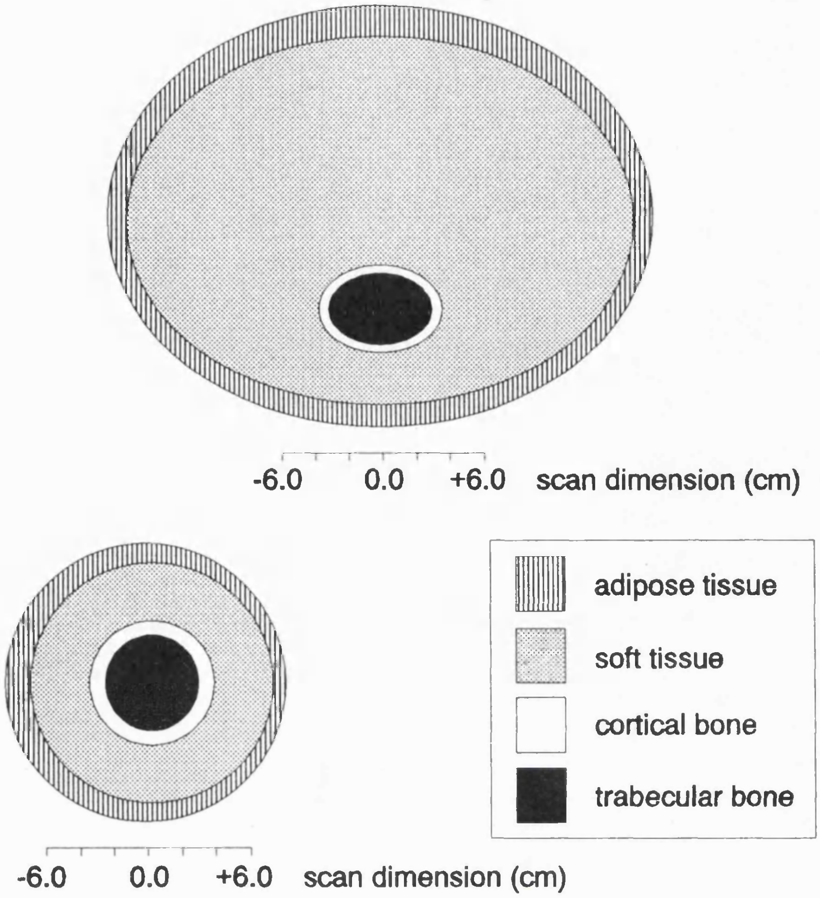

Figure 2.5 Schematic diagram of measurement phantom cross-sections. The upper phantom represents the lumbar spine measurement site, the lower phantom represents the femoral neck site.

Femoral neck site measurement phantoms								
Phantom	Adipose tissue		Soft tissue		Cortical bone		Trabecular bone	
	x [cm]	z [cm]	x [cm]	z [cm]	x [cm]	z [cm]	x [cm]	z [cm]
1	5.25	5.25	3.98	3.98	3.25	3.25	2.75	2.75
2	6.25	6.25	4.73	4.73	3.25	3.25	2.75	2.75
3	7.25	7.25	5.49	5.49	3.25	3.25	2.75	2.75
4	8.25	8.25	6.25	6.25	3.25	3.25	2.75	2.75
5	9.25	9.25	7.01	7.01	3.25	3.25	2.75	2.75

Lumbar spine site measurement phantoms								
Phantom	Adipose tissue		Soft tissue		Cortical bone		Trabecular bone	
	x [cm]	z [cm]	x [cm]	z [cm]	x [cm]	z [cm]	x [cm]	z [cm]
1	13.00	9.79	11.96	8.67	3.20	2.10	3.00	1.90
2	14.00	10.55	12.88	9.33	3.20	2.10	3.00	1.90
3	15.00	11.30	13.80	10.00	3.20	2.10	3.00	1.90
4	16.00	12.05	14.72	10.67	3.20	2.10	3.00	1.90
5	17.00	12.80	15.64	11.33	3.20	2.10	3.00	1.90

Table 2.1 x and z half-axis dimensions of the tissue components in the femoral neck and lumbar spine phantoms used in the photon absorptiometry computer simulations.

2.2.5 Random number generation

A crucial aspect of Monte Carlo computer simulation is the quality of the random numbers. A set of random numbers must be uniformly distributed. All of the random numbers used in the simulations were generated using the NAG library G05CAF routine. As the simulations were very CPU intensive the models were run on different computers within the department. Each machine handles floating point operations slightly differently so statistical tests on the random number generator were implemented on each computer. Three sets of 10^5

random numbers were used in a frequency test, a serial test and a correlation test. These tests are fully described in Morin *et al* (1979) and Knuth (1969). The frequency test uses a chi-squared statistical test to assess the equidistribution of the random numbers. The serial test checks that successive pairs of numbers are uniformly distributed independently of each other. Finally the correlation test calculates the serial correlation coefficient of the random number sequence. This coefficient is always between -1 and +1, where a value close to or equal to zero implies no linear dependence. Table 2.2 summarises the results for each of the machines used for the simulations. All of the machines passed the statistical tests described above.

Computer	**Type of processor**	**Correlation Coefficient**	**Frequency test**		**Serial pairs test**	
			V	**χ^2percentage†**	**V**	**χ^2percentage†**
SUN 4	SPARC	-0.00184	85.2	80-90	119.3	5-10
		-0.00041	102.4	40-50	74.1	97.5-99
		-0.00112	95.1	50-60	109.1	20-30
SPARCstation IPC	SPARC 1+	-0.00127	72.8	97.5-99	109.8	20-30
		-0.00372	99.1	50-60	101.4	40-50
		-0.00521	96.4	50-60	90.6	70-80
SPARCstation SLC	SPARC 1+	0.00253	105.9	30-40	131.1	2.5-1
		0.00741	105.5	30-40	91.4	70-80
		0.00390	92.1	70-80	89.0	70-80

† - percentage points of the χ^2-distribution taken from Lindley and Scott (1984)

Table 2.2 Results of three statistical tests on the random number generator G05CAF run on each of the computer workstations used in the photon absorptiometry Monte Carlo computer simulations.

Chapter 3.

Evaluation and discussion of Photon Absorptiometry simulation results

3.0 Introduction

The previous chapter has described the problem of scatter during PA bone density measurements. This chapter presents the results for the computer simulations of the DPA and DEXA bone density scans described in chapter 2, and discusses the consequent effects of scatter on the calculation of the bone mass M_b.

3.1 DPA and DEXA computer simulation results

Each computer simulation produced a value for the number of photons transmitted and scattered within the energy windows at each measurement point across the scan. Each model was simulated both with and without the bone being present in the phantom to generate values of I and I_o. An example of the data produced is presented in figure 3.1, which shows the transmission counts from a DPA femoral neck scan. All the scans showed a significant increase in counts when the scatter contribution was included, which would be the case in a clinical measurement. As the scan traversed the phantom an increase in absorption was apparent as the tissue thickness increased. A sharp decline in transmitted counts down to a minimum value occurred at the bone edge, due to cortical bone absorbing photons more effectively than the soft tissues. As the scan crossed the bone, which contained both cortical and trabecular bone tissue, there was also a variation in counts which reflected the bone thickness changes. Absorption gradually increased as the scan moved towards measurement position 0.0 cm, but overall was less than the absorption at the bone edges where the radiation path encountered cortical bone only. Figure 3.1a shows a closer view of the variation of absorption as the beam was scanned across the bone.

In the femoral neck phantom the soft tissue and bone components were not centrally positioned within the fat layer, and this produced an asymmetrical distribution of both scatter and transmitted counts about measurement position 0.0 cm. In the lumbar spine phantoms the bone was positioned centrally along the z-axis producing a symmetrical plot about position 0.0 cm.

Figure 3.2 shows the variation of scatter counts from the same scan simulation as figure 3.1. Detected counts in the low energy window exhibited a larger proportion of scattered photons and this is more clearly shown in figure 3.3, which depicts the variation of the scatter fraction for these scans. Simulation of the DEXA scans showed a higher proportion of scatter from the high energy window, as there were a large number of high energy photons incident from the initial polychromatic spectrum. Similar results were produced for both the DPA and DEXA scans respectively with phantoms of both types and of all sizes. The edges of the bone contained cortical bone only and corresponded to a large increase in the scatter fraction at these points. This may be attributable to two main effects: firstly there were more transmitted photons attenuated which effectively increases the scatter fraction, and secondly the higher density of cortical bone increased the amount of Compton and Rayleigh scatter. Figure 3.3a shows the variation of the Compton and Rayleigh scatter fractions across the measurement phantom. This figure shows that Rayleigh scatter was the dominant scatter interaction. This was expected as the detector collimator accepted transmission photons and photons forward scattered at small angles. Also a photon that has undergone a single coherent scattering interaction ~~are~~ is more likely to escape from the phantom than an incoherently scattered photon, since ~~they~~ it retains ~~their~~ its original energy, and the small scattering angle results in a shorter path length. This effect has been described by Chan and Doi (1985). The scatter fractions were calculated separately as the total Rayleigh scatter or

Compton scatter detected divided by the total counts detected. This is confirmed by the scatter profile in figure 3.2 which has similar width dimensions of the bone and phantom as the transmission profile (figure 3.1) which would indicate that forward scatter is the dominant interaction being detected. This would also seem to imply that multiple scattering is a small component of the detected scatter which is confirmed by the computer simulation data.

Figure 3.2 indicates that the interaction cross-section dependence on atomic number Z for low energy scatter for both Compton and Rayleigh produced a variation which clearly marked the bone. At higher energies the dependence of interaction probability on energy became the dominant term and the variation of scatter across the phantom became more uniform. This effect was not so obvious in the DEXA simulations since the effective energy of the high energy part of the spectrum was significantly lower than the high energy components of the DPA initial spectrum.

Scatter fractions were calculated to show the amount of scatter relative to the number of transmitted photons since the amount of absorption determines the number of photons available for scattering and also the number of scattered photons which are themselves transmitted.

Generally the results all exhibit similar behaviour although the proportion of scatter to transmission does vary between phantoms and systems. The proportion of scatter for the DPA system ranges from 7% to 25%, and for the DEXA system ranges from 6% to 20%.

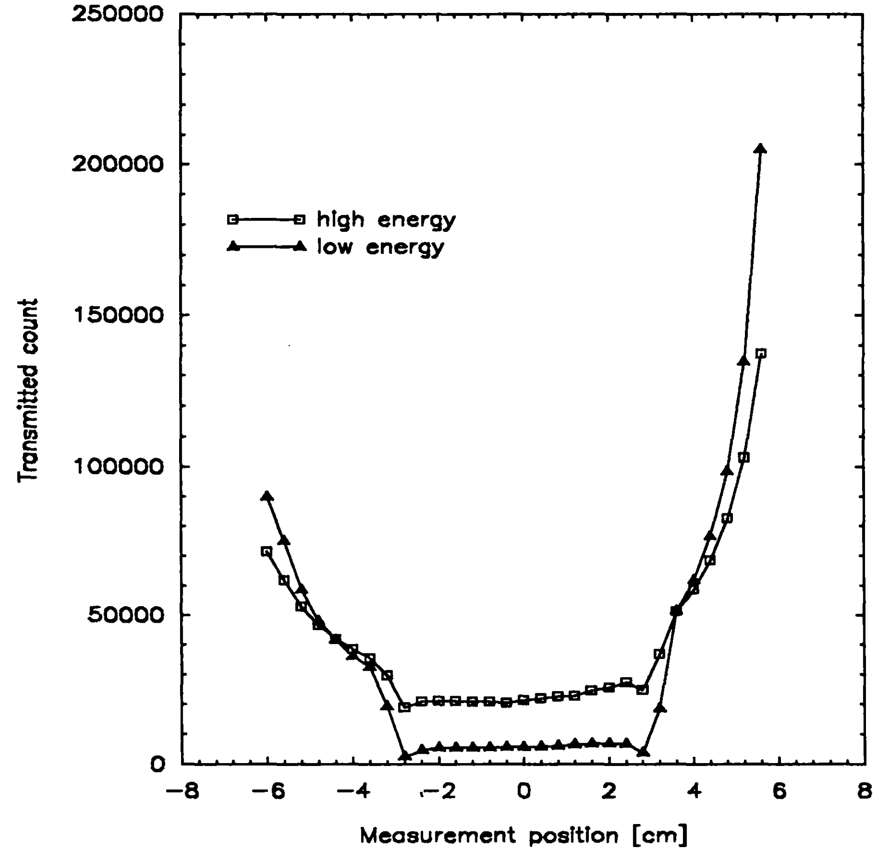

Figure 3.1 Graph of transmitted photons versus measurement position. Simulation is a DPA scan of a size 3 femoral neck measurement site phantom.

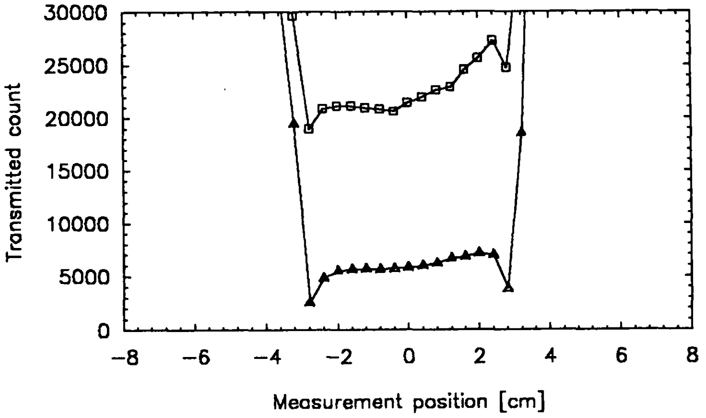

Figure 3.1a Feature from figure 3.1 showing detail of transmitted counts through the bone.

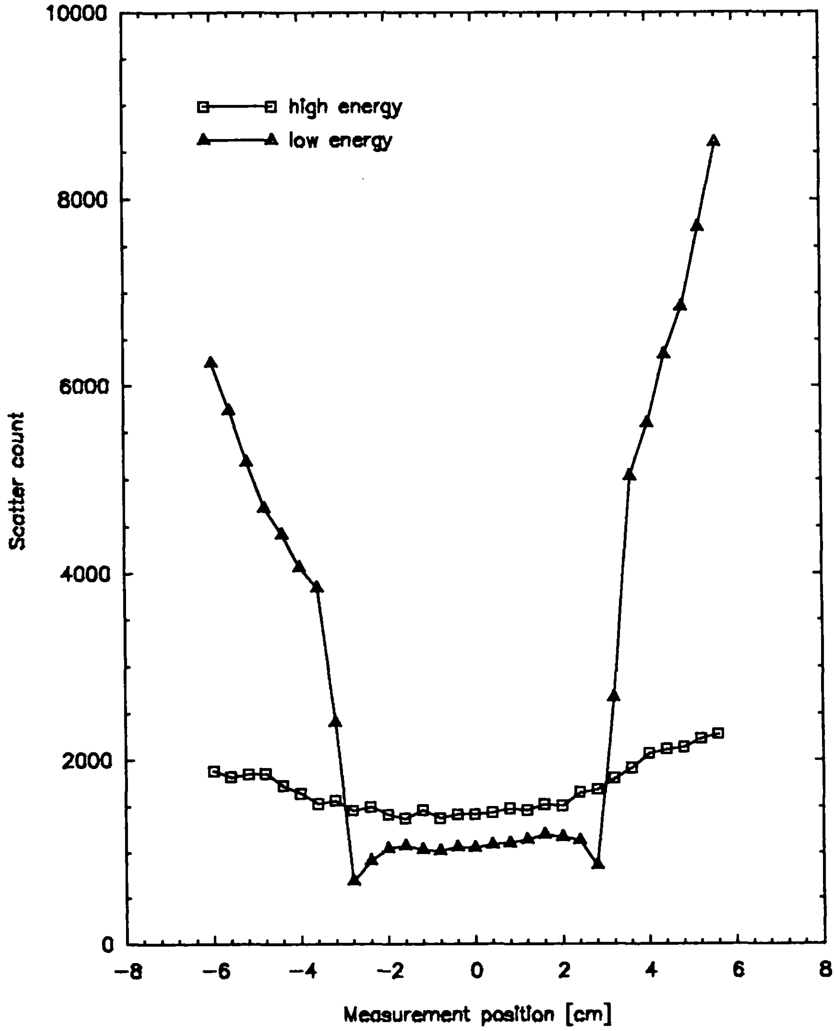

Figure 3.2 Graph of scattered photons versus measurement position. Simulation is a DPA scan of a size 3 femoral neck measurement site phantom.

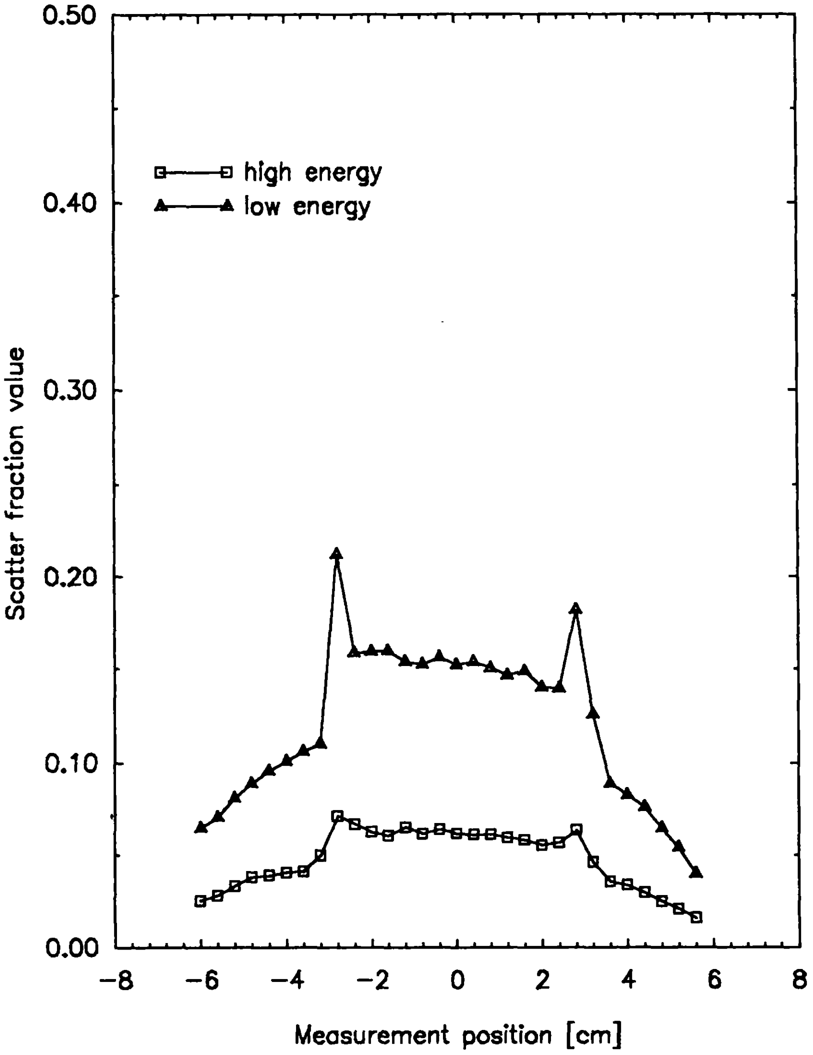

Figure 3.3 Variation of scatter fraction with measurement position. Simulation is DPA bone density scan of size 3 femoral neck measurement site phantom.

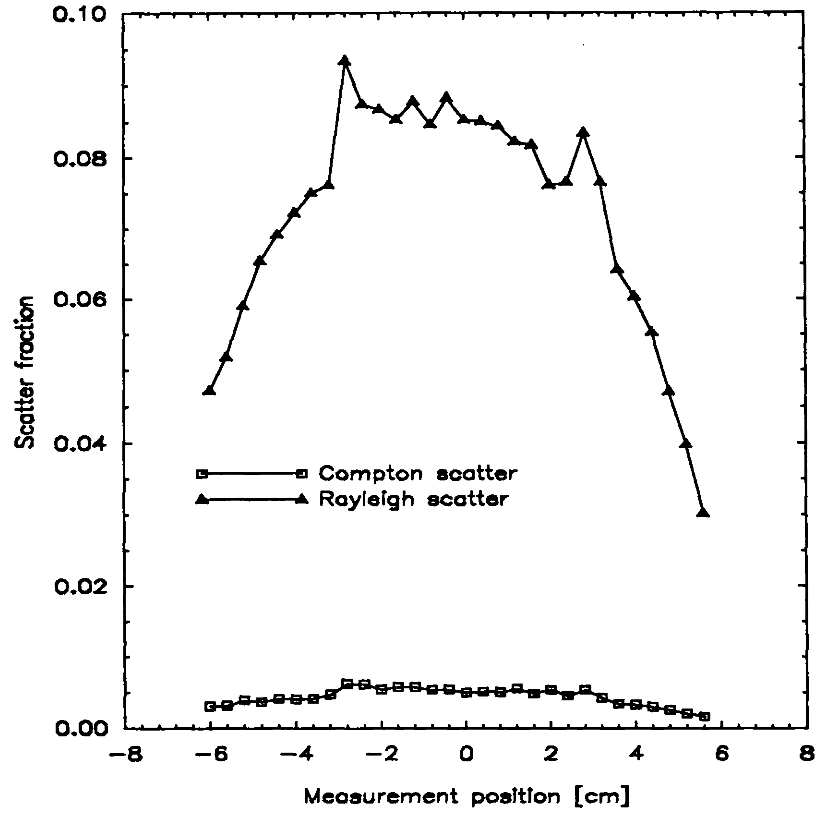

Figure 3.3a Graph showing scatter fractions of total Compton scatter and total Rayleigh scatter.

3.2 Calculation of M_b

Values for M_b were calculated from the computer simulation data using the theory described in section 2.0. Two sets of calculations of $ln\ I_0^l/I^l$ and $ln\ I_0^h/I^h$ were made at each scan point, one set included the scatter component and the other set excluding the scatter. The bone extremities, which consisted of cortical bone only, are easily recognisable as well defined troughs (figure 3.1 and 3.1a) corresponding well to the phantom dimensions. A decrease in transmitted counts at these points increases the values of $ln\ I_0^l/I^l$ and $ln\ I_0^h/I^h$, of which an example is shown in figure 3.4. Values of N were calculated at each scan point and plotted. A baseline was manually fitted between the outer edges of the bone values defining the area A (figure 2.1). An algorithm based on the trapezium rule was used to calculate a value for A. The constants D_{sf} and D_{sb} were determined from the attenuation coefficient data (section 3.2.0) and a value for M_b computed. All values of M_b were determined assuming a unit width of the transverse bone section.

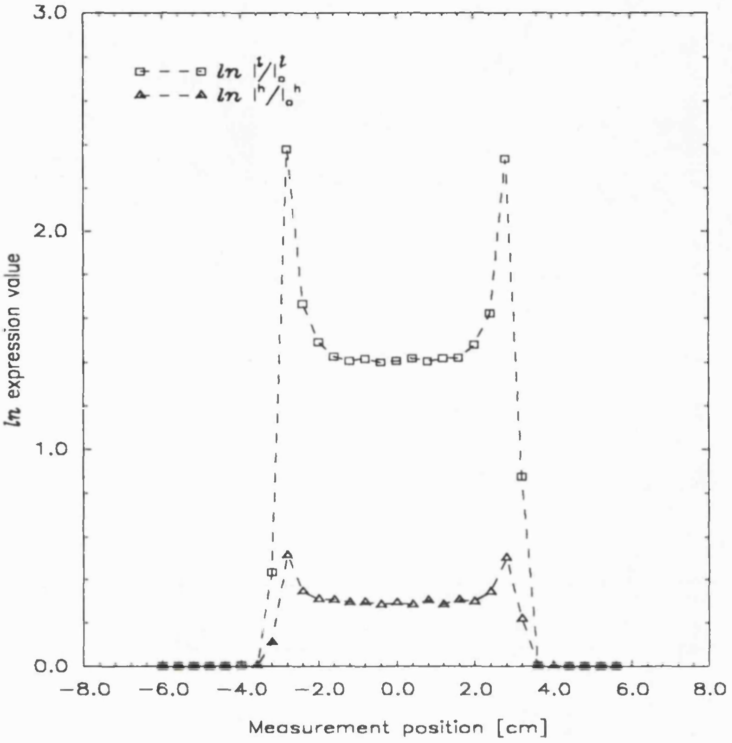

Figure 3.4 Graph showing *ln* expression values for the femoral neck phantom (size 1) without the scatter component. The two peaks are due to the bone edges.

3.2.0 Attenuation Coefficients

Calculation of N from the *ln* terms in equation 2.7 required accurate mass attenuation coefficient values. For the DPA simulation the values used were -

$\mu_s^l = 0.218\ cm^2g^{-1}$ $\mu_s^h = 0.152\ cm^2g^{-1}$ $\mu_b^l = 0.710\ cm^2g^{-1}$ $\mu_b^h = 0.210\ cm^2g^{-1}$

These coefficients were calculated from attenuation measurements of Gadolinium-153 γ-rays through water and hydroxyapatite made by Tothill *et al* (1983). The ratio of μ_s^h/μ_s^l is 0.697 and is close to that reported by other workers. These values are commonly used in clinical situations and are used here in order to simulate a clinical situation as closely as possible. They differ from the values used in the Monte Carlo simulation by approximately 1%-2% which had a negligible effect on the final value of M_b.

For the DEXA measurement the mass attenuation coefficient values were:

$\mu_s^l = 0.248\ cm^2g^{-1}$ $\mu_s^h = 0.187\ cm^2g^{-1}$ $\mu_b^l = 0.413\ cm^2g^{-1}$ $\mu_b^h = 0.214\ cm^2g^{-1}$

These were calculated from the effective energies of the low energy and high energy parts of the x-ray spectrum calculated with respect to water. The attenuation coefficients for these two effective energies were computed by interpolation from attenuation coefficient data from Storm and Israel (1970) utilising the mixture rule as described by Baba-Hamed (1990), and are the same values as used in the Monte Carlo simulation.

Values of N were plotted at each scanning point for transmitted only and transmitted + scattered photons. However, before a final value of M_b could be calculated some of the statistical errors in the simulation data had to be reduced.

3.2.1 Error Reduction

In order to avoid impractical computing times only $2x10^6$ photon histories could be followed at each scanning point. For the larger phantoms increased absorption led to lower counts resulting in higher statistical errors. Increasing counts and reducing the error without an increase in computing time is known as variance reduction. One technique employed was the averaging of corresponding data points in symmetrical data sets. This could only be performed on the lumbar spine simulation data sets which were symmetrical about the z-axis.

3.2.2 Baseline Selection

Another inherent source of error was the positioning of the baseline on the plot of the N values prior to the calculation of the area A. Errors from this source have been shown to be significant in patient measurements because of the inhomogeneity of the fat deposits around the examination site (Roos *et al*, 1980). In the mathematical phantoms employed in the computer simulations there were no inhomogeneities present in the tissues examined, and so the baseline position was found with a relatively small error. The position of the baseline was evaluated from the average value of the measurement points on either side of the bone.

3.2.3 Values of M_b

Values for the area A, D_{sb} and of D_{sf} were used to calculate M_b, the total bone mass. To avoid errors due to edge effects near the cortical and trabecular bone boundary only the mass of the central part of the bone was considered. To normalise the results between bone sizes the bone mass was divided by a unit width of the central transverse part of the bone. These values are shown in tables 3.1 and 3.2 and have been normalised to a reference value of 1.000 gcm^{-1} in order to show comparative changes clearly. A graph showing the change in M_b with phantom size is shown in figure 3.5. Measurement site phantom sizes are shown in table 2.1.

The absolute values of bone mass differ between the DPA and the DEXA evaluations even though the density of the bone in the computer models was the same. This is attributable to several factors. Primarily the different incident spectrum and instrument geometry produce very different values for the low and high energy transmission and scatter counts, especially relevant is the relative proportion of low to high energy counts. In addition to this different mass attenuation coefficient values had to be used to calculate the bone mass values.

Similarly the different proportions of scatter generated from DPA and DEXA are attributable to the different initial spectra and to the instrument geometry. This had the effect of producing different absolute values of bone mass calculated with scatter for DPA and DEXA. This was apparent with the DPA values of M_b being lower than the DEXA values of M_b when calculated with scatter.

The results showed a decrease in the bone mass M_b when scatter is included in the calculations. As this is the situation in a clinical measurement it is apparent that a bone density measurement will produce a value of M_b lower than the true value. The difference between M_b with scatter, and M_b without scatter is not constant but changes with phantom size. Calibration with a single standard size phantom before measurements will not be sufficient to negate the effects of the scatter contribution if the patient changes size during long term serial measurements.

	Dual Photon Absorptiometry		**Dual Energy X-ray Absorptiometry**	
Phantom size	M_b no scatter [gcm^{-1}]	M_b with scatter [gcm^{-1}]	M_b no scatter [gcm^{-1}]	M_b with scatter [gcm^{-1}]
1	1.001 ± 0.001	0.985 ± 0.001	1.001 ± 0.002	0.993 ± 0.002
2	1.000 ± 0.001	0.985 ± 0.001	1.001 ± 0.002	0.991 ± 0.002
3	1.000 ± 0.001	0.984 ± 0.001	0.999 ± 0.002	0.990 ± 0.002
4	1.001 ± 0.001	0.985 ± 0.001	1.001 ± 0.002	0.991 ± 0.002
5	1.001 ± 0.001	0.985 ± 0.001	1.000 ± 0.002	0.990 ± 0.002

Table 3.1 Values of M_b for the femoral neck measurement site phantom calculated both with and without the scattered beam component.

	Dual Photon Absorptiometry		**Dual Energy X-ray Absorptiometry**	
Phantom size	M_b no scatter [gcm^{-1}]	M_b with scatter [gcm^{-1}]	M_b no scatter [gcm^{-1}]	M_b with scatter [gcm^{-1}]
1	0.998 ± 0.002	0.976 ± 0.001	0.997 ± 0.002	0.985 ± 0.002
2	1.001 ± 0.002	0.973 ± 0.001	1.003 ± 0.002	0.986 ± 0.002
3	1.003 ± 0.002	0.972 ± 0.001	1.000 ± 0.002	0.984 ± 0.002
4	1.001 ± 0.002	0.970 ± 0.001	1.001 ± 0.002	0.983 ± 0.002
5	0.997 ± 0.002	0.966 ± 0.001	1.000 ± 0.002	0.980 ± 0.002

Table 3.2 Values of M_b for the lumbar spine measurement site phantom both with and without the scattered beam component.

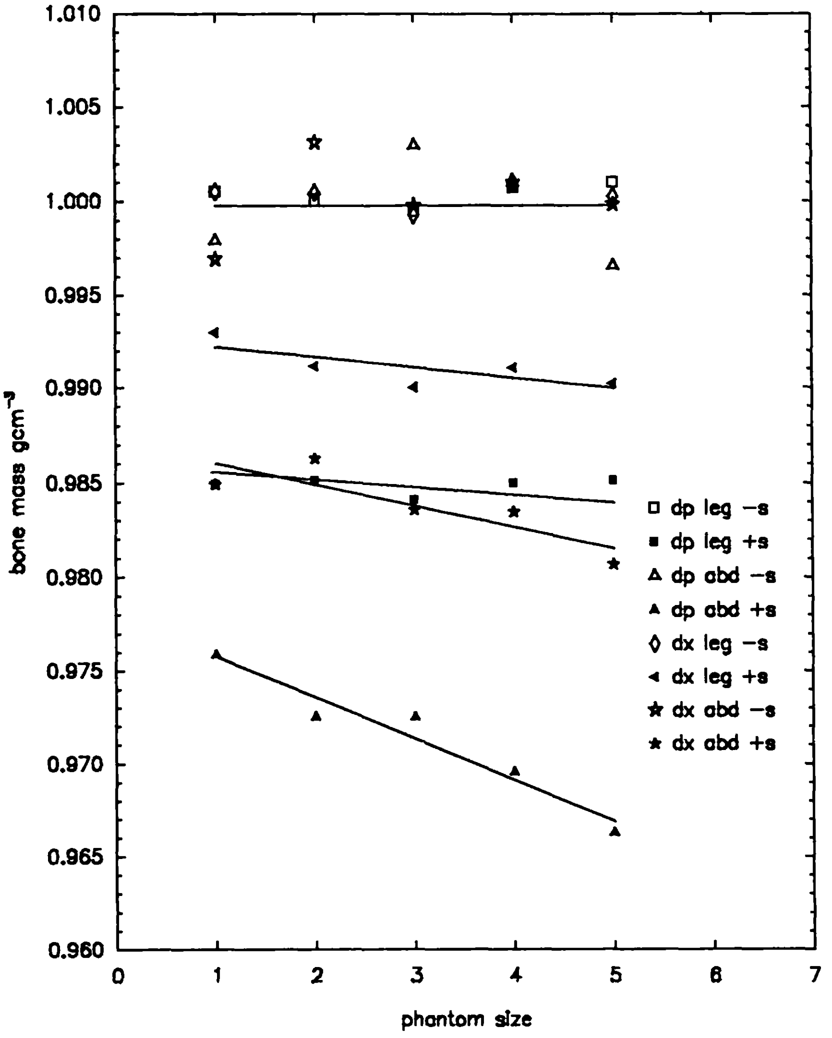

Figure 3.5 Values of M_b calculated for different systems, phantom sizes and measurement sites. Values are shown for narrow beam and clinical conditions.

dp=DPA; dx=DEXA; leg=Femoral neck site; abd=Lumbar spine site; +s indicates scatter is included; -s indicates scatter is excluded.

3.3 Discussion and conclusions

Inclusion of scatter in M_b calculations not only produced a lower value of bone mass for a measurement site, but decreased the bone mass value with respect to phantom size. For a DPA femoral neck site scan there was only a slight decrease of bone mass as patient size increased. The DPA scan on the lumbar spine site showed a decrease of bone mass of 0.15 ± 0.03 % per patient size increase.

For the DEXA scans the loss rates were 0.07 ± 0.03 % per size increase for the femoral neck site, and 0.11 ± 0.03 % per size increase for the lumbar spine site. The larger loss rates for the abdomen sites were due to the larger scatter fractions produced during the scans. This could be attributable to the larger tissue volume being irradiated during a scan producing a larger proportion of scatter.

Although these values of bone mass loss are smaller than errors derived from tissue calcification, bowel gas or tissue inhomogeneities, account should be taken of patient size variation during long term longitudinal bone mass measurements. The values of bone mass loss were also calculated under ideal conditions; with a calibration phantom exactly the same size and composition as each of the measurement sites. This would not be the case during a clinical scan.

Since absolute values of bone mass are rarely used and since base levels in most systems are normalised by the use of a calibration phantom, it is the variation between measurements when the patient size changes that is generally important. Several aspects of the results obtained from the DPA and DEXA computer simulations should be considered. This may include serial measurements on any single type of system and the effects of patient changes, comparative measurements between different systems, or differing calibration conditions.

3.3.0 DPA and DEXA comparison

The primary difference between the DPA and DEXA systems are their radiation sources, which produce different values for the low and high energy transmission and scatter counts on identical measurement sites. Especially relevant is the relative proportion of low to high energy counts. In addition, the DPA system has a less rigorous detector collimation in order to maintain high count rates and so the detected signal contains a higher proportion of scatter counts. Figure 3.5 shows the variation in bone density estimates for identical phantom conditions using the two different systems. This graph shows that for the phantom range both DPA and DEXA, within statistical limits, give the same results when only primary radiation is considered. When scatter is included in the calculations the measured bone density is reduced and the magnitude of the reduction is dependent on the system and the phantom size. A 0.5%-3.5% reduction can be expected between system types. If comparisons between measurements on different systems are being made, part of this deficit would still be present even if the scatter in an individual system had been corrected for by calibration. From figure 3.5 the remaining deficit would be 0.8% for the femoral neck or 0.9%-1.5% for the abdomen. This effect would be apparent when comparing DEXA bone density measurements with a previous DPA database for example.

3.3.1 Effect of phantom size

Serial measurements, separated by 3-4 months, are taken during patient studies. During this period the patient may lose or gain weight with a corresponding change in patient dimensions. Figure 3.5 shows the variation in bone mass estimates when changes occur in phantom size with no change in bone density. Even if the 'scatter effect' has been removed by calibration with a phantom of known density, the effect that would be introduced by a calibration phantom of different size to the patient would still remain. Figure 3.5 indicates this may range from 0.5% (DEXA femoral neck) to 1% (DPA abdomen).

Dual energy absorptiometry is the most frequently used method for estimating bone density. If absolute bone mass values or changes in measured values are to be used then the measurement conditions become important in defining the degree of bias introduced due to the effect of scatter. It has been shown that the systems studied are not very sensitive to the degree of scatter and are likely to introduce errors of the order of 1%. However, since density changes reflect bone strength changes by a factor of two greater it is thought that a change of 3% could be significant (Mosekilde *et al*, 1987; Britton and Davie, 1990). Thus, when making serial measurements patient size should be taken into account or when comparing measured values with previously obtained data sets the conditions of measurement should be considered.

Chapter 4.

Theory and method of Compton Scatter Densitometry

4.0 Introduction

Scattered photons as a useful source of information is a concept epitomised by x-ray diffraction techniques, which have been widely used in the study of chemical and biological molecular structures. This technique has been recently extended into the characterisation of tissues by small angle scattering (SAXS) using polychromatic spectra from diagnostic x-ray sources with energy sensitive detectors (Royle and Speller, 1991).

Compton Scatter Densitometry (CSD) utilises the proportional relationship of Compton scatter intensity to physical density in order to find the physical density of various body tissues. Applications of this technique have included the determination of skeletal bone density and the measurement of lung tissue density (Hanson *et al,* 1984).

Electron densities of tissue volumes within tissue masses have also been determined using dual-energy Compton scattering employing isotopic sources (Huddleston and Sackler, 1984). A further application extends the principles of dual energy Compton scattering to dual energy Compton scatter imaging which uses the concepts of transmission computed tomography to obtain slice images of subjects (Harding and Tischler, 1986).

A method which combines the density dependence of Compton scatter with the dependence of coherent scatter on the product of density and the square of the effective atomic number has been described by several authors (Kerr *et al,* 1980; Puumalainen *et al,* 1982). Measurement of the coherent to Compton ratio avoids the need for corrections due to attenuation within the subject and has been shown to be related to bone mineral content.

A review by Speller and Horrocks (1991) provides a more detailed reference to the uses of scatter in biological and medical applications.

This chapter will describe the development of a CSD system using *in vitro* techniques in preparation for *in vivo* measurements of bone density. The assessment of optimum operating conditions for this system are made theoretically and experimentally, and the method for taking measurements on phantoms containing known density solutions and bone tissue samples are described. The procedures and results obtained from these measurements are presented in this chapter.

4.0.0 Use of computer simulations

This chapter contains data collected from Monte Carlo based computer simulations. The use of these simulations allows information to be extracted which is not obtainable from experimental data, for example, the relative proportions of scatter in a detected beam. Direct or indirect verification of the data from these models has been made experimentally wherever possible and the sets of data compared.

4.1 Theory of CSD

CSD was primarily conceived as a method for non-invasive measurements of tissue density *in vivo*, and has been extensively used for the determination of bone density for the diagnosis of osteoporosis. CSD was first applied using isotopic monochromatic radiation sources (Clarke and Van Dyke, 1973) and consequently suffered from large statistical errors, lengthy counting times and a poor spatial resolution which reduced the accuracy of the technique.

A theoretical description which employed polychromatic x-ray tube sources, in order to reduce the statistical error and improve spatial resolution, was first described by Duke & Hanson (1984). The techniques described in this chapter are based on these theories and a brief summary is presented in the following paragraphs.

The Compton interaction involves the weakly bound outer electrons of the atom which are assumed to be free and stationary. The probability of Compton scatter is determined by the number of scattering sites in the material irradiated (Knoll, 1979), which is described by the electron density. The electron density can be related to the physical density by the effective ratio of the atomic number to atomic weight.

$$\rho - \rho_e \left(\frac{Z}{A}\right)_{eff} N_A \tag{4.1}$$

where

ρ	physical density [gcm^{-3}]
ρ_e	electron density [e^{-1}cm^{-3}]
N_A	Avogadro's number
$(Z/A)_{eff}$	effective ratio of atomic number to atomic mass
	$= \sum a_i \, (Z/A)_i$ where a_i is the fractional content of electrons for each element in the material

The number of Compton scatter photons S can then be shown to be

$$S \propto \frac{1}{(N_A \left(\frac{Z}{A}\right)_{eff})} \rho \tag{4.2}$$

This relationship can be used to find the density of a material in a volume defined by the collimated beams of a source and detector. However, this relationship is only true if there is no attenuation of the incident and scattered photon beams within the material. Using the exponential attenuation law an expression can be formed which accounts for the attenuation of the incident beam and the scattered beam in the tissues of the measurement site (Duke and Hanson, 1984). If the critical volume is not positioned in the centre of the measurement site or if the measurement site has an asymmetrical cross-section producing different radiation path lengths, then two incident beams and two detectors must be used. The incident beams are arranged at an angle to each other which defines a volume at the intersection of each of the source and detector beams (figure 4.1).

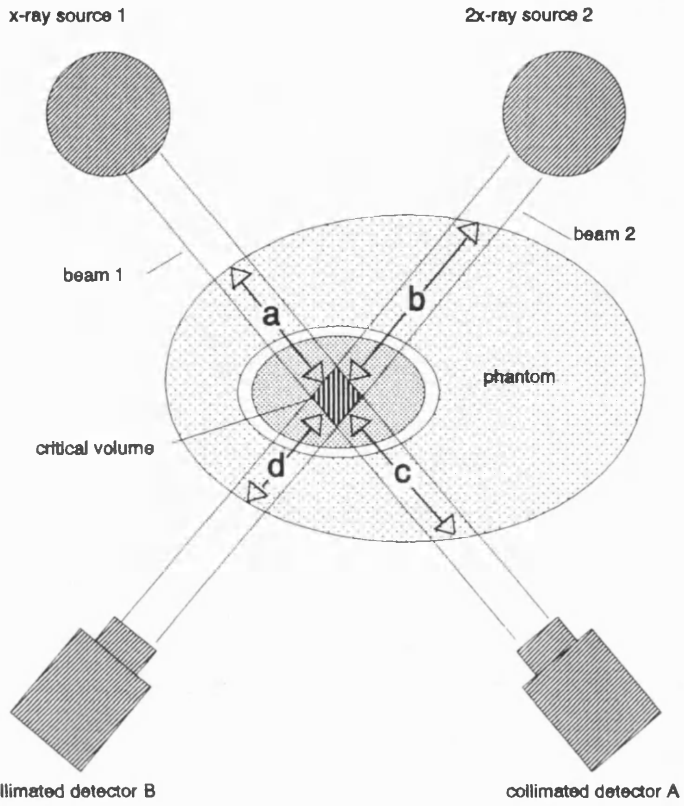

Figure 4.1 Schematic diagram of CSD geometry showing intersection of beams and the radiation path lengths (*a,b,c,d*).

Beam 1 is activated and the transmission counts detected at detector A and the corresponding scatter counts at detector B. Beam 1 is turned off and beam 2 activated, whereupon detector B counts the transmission and detector A counts the scatter. This geometry dictates that the transmitted and scattered beams share the same radiation paths through the measurement site. This allows an expression to be formed which relates the physical density of the defined volume, known as the critical volume, to the ratio of transmitted and scattered photons.

$$\rho = k\left(\frac{S_1 S_2}{T_1 T_2}\right)^{\frac{1}{2}} bcf(a,b,c,d,\theta,E_{spec}) \qquad 4.3$$

where

ρ	physical density of critical volume [gcm^{-3}]
k	calibration constant
S_1, S_2	scattered counts at detectors 1 and 2
T_1, T_2	transmitted counts at detectors 1 and 2
bcf	bias correction factor; a function of radiation path lengths, scattering angle and incident energy spectrum

The *bcf* term in equation 4.3 corrects for several errors introduced by beam polychromacity and measurement geometry. Differential attenuation due to the Compton shift of the scattered photons produces significant errors if the mean free path change of the scatter is large or if the attenuation coefficient of the materials increases rapidly with energy. In the geometry described this effect is small, as the mean free path change is small and the attenuation coefficient change of biological materials with energy is small. A finite geometry error is also corrected for by the *bcf*, this is a small error attributable to the finite range of the dimensions *a,b,c,d* produced because the critical volume occupies a finite volume. A simple geometrical model of the attenuation through the scattering volume using a monoenergetic beam reveals that a volume of finite dimensions introduces a density error of <1% and should be considered negligible. These results has been confirmed by the work of Kennett and Webber (1976) which also assumes a monoenergetic beam.

The errors described above have been shown to be negligible (Koligliatis, 1990) when calculating bone density from CSD measurements using polyenergetic sources on the experimental gantry described in this chapter.

The contribution that these components of the *bcf* represent are found to be at least an order of magnitude smaller than the error introduced by the detection of multiply scattered photons by the scatter detector (Duke and Hanson, 1984; Speller and Horrocks, 1988). These are photons which have been scattered more than once inside the tissues of the measurement site, have entered the scatter beam and have been counted as single scatter. This is considered the significant part of the *bcf* in this thesis and is referred to as the multiple scatter correction factor (*mcf*). Part of the work of this thesis is the calculation of *mcf* values for the CSD system under consideration and their application to the experimental data collected from it. (§4.4). By considering only the multiple scatter element of the *bcf* to be significant then equation 4.3 can be written as

$$\rho = k\left(\frac{S_1 S_2}{T_1 T_2}\right)^{\frac{1}{2}} . mcf \qquad 4.4$$

where

mcf correction factor for multiple scatter

4.2 Apparatus

The CSD apparatus has been previously constructed and described by Koligliatis (1990), and the results for some phantom measurements presented. The precision of these measurements was found to be within the range 1-3%. One of the aims of this present thesis was to improve the precision and ensure the measurements are reproducible. This has involved some of the following work; computer simulations of a wide range of incident beam kV_p values have been made, in order to optimise performance, and confirmed with experimental measurements. Similarly, the reduction of detected multiple scatter by energy windowing has been modelled. A new set of *mcf* values have been calculated for the gantry geometry described in this section and applied to the CSD measurement data. A study of the critical volume geometry has been made and CSD measurements have been performed on biological samples.

The work presented in the following chapters was a continuation and development of the work presented by Koligliatis (1990). One of the main aims of this present thesis was to produce a CSD device which would provide reproducible bone density measurements with sufficient accuracy and precision to allow measurements to be made on a patient population. A schematic diagram of the apparatus and the electronic components are shown in figures 4.2 and 4.3. A photograph of the gantry is shown in figure 4.5

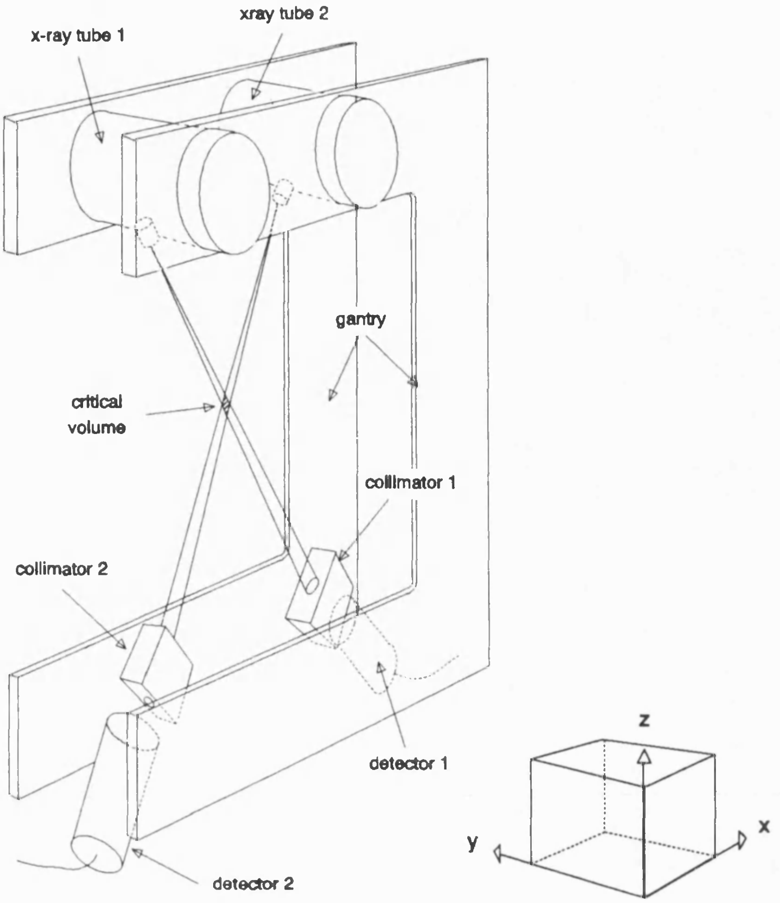

Figure 4.2 Schematic three-dimensional diagram of CSD apparatus described in section 4.2.

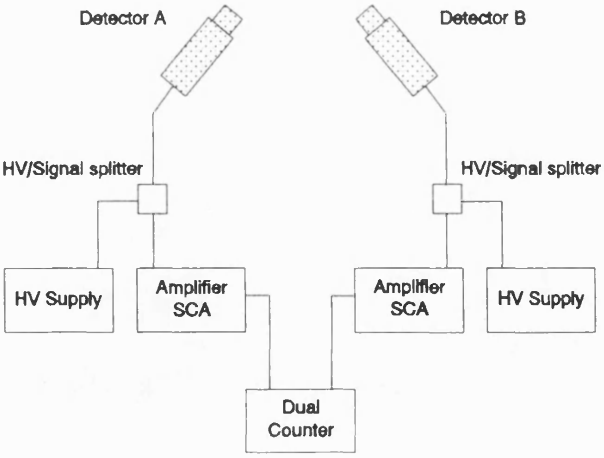

Figure 4.3 Schematic block diagram showing electronic components used for the CSD measurements.

4.2.0 Apparatus development

One of the crucial aspects of the apparatus was the alignment of the x-ray beams with the detector collimators and the intersection of the beams to form the critical volume. Periodic checks were made on the beam alignments using x-ray sensitive film. A stack of film-badge emulsions was placed at the critical volume position and exposed to both beams. The films provided images of sections through the critical volume, and the coincidence of the two beam spots on the films showed the intersection of the beams. An example set of these films is shown in figure 4.4. Single films were placed over the detector collimators to verify the intersection of the beams with the collimator openings.

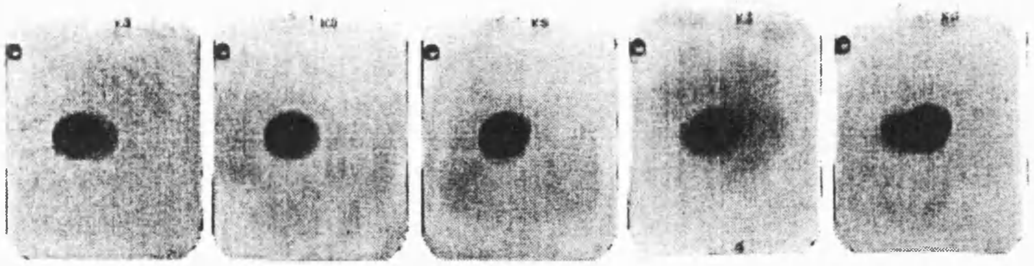

Figure 4.4 Stack of dental x-ray films exposed at position of critical volume on CSD apparatus. Films show intersection of beam spots from x-ray tubes A and B.

New sodium iodide scintillation detectors [Hilger Analytical, model P6401.Mk1] with matched resolutions were fitted to the gantry as detectors A and B (figure 4.3). Resolution measurements of the detectors were made on the gantry and were found to be 12.6 ± 0.4 % for detector A and 12.3 ± 0.4 % for detector B at 59.5 keV. The response of the detectors to count rate has been measured by Koligliatis (1990) and has shown a difference in response at low (~100-3000 cps) and high (~5000-20000 cps) count rates. Detector response to count rate is important as the scatter and transmission count rates differ greatly and a change in response may need to be corrected. If a uniform detector response gradient is assumed, for both scattered and transmitted counts, the measured density ρ will be higher than expected since the recorded transmitted count will be less.

Previously reported measurements of density (Koligliatis, 1990) have been made with large thicknesses of copper foil used as transmission filters in order to reduce the transmission count rate. This avoids detector saturation and moves the transmission detector response to count rate towards the same region as the scatter detector. However, this filtration had the effect of hardening the transmitted beam spectrum after transmission through the phantom, and also of producing large amounts of multiple scatter within the thickness of copper. These copper filters have been substituted with a 100µ diameter Au/Pt (90%/10%) pinhole diaphragm (Degussa, Germany). This had the beneficial effect of reducing the transmission count rate into the same region of response as the scatter detectors, without hardening the transmission beam and without producing more multiple scatter. The pinhole introduced a new bias into the measurements since the scattered photon beams would not be following the exact same path as the transmitted photon beams, although the path length would be the same the beam path diameters would be different. This would not affect the size of the critical volume as this is defined by the intersection of the transmitted beam from the source and scattered beam detector collimation. A simple geometric model indicated that the error introduced by reduction of the transmission detector collimator diameter is less than 1% and can be considered negligible. The model considered the attenuation of the beam through the different radiation path lengths introduced by the reduction of the transmission detector collimator. This was confirmed by Kennett and Webber (1976) who made measurements of the error introduced by finite geometry change by altering the diameter of the incident photon beam. Density measurements were found to be below 1% and consequently this source of error was considered negligible.

The x-ray spectra under consideration in these experiments ranged between 80 kV_p to 120 kV_p which produced a range of interest between 50 keV to 91 keV. For NaI(Tl) detectors the absolute quantum detection efficiencies in this energy range is approximately constant (Knoll, 1979).

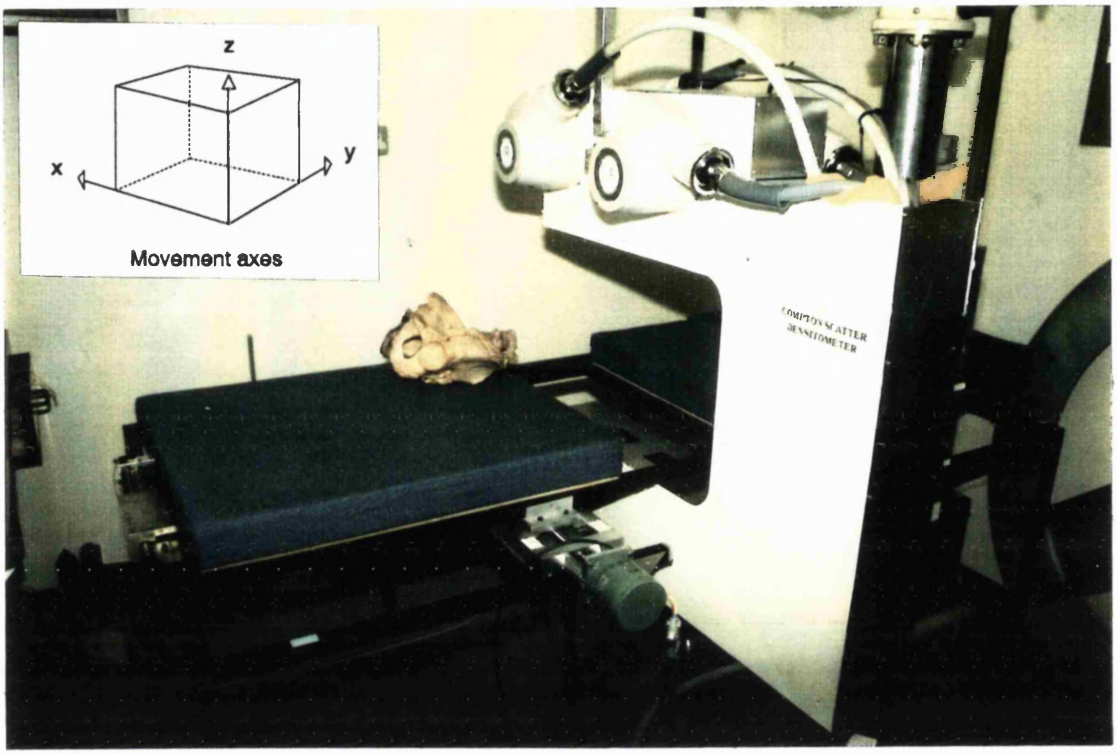

Figure 4.5 Photograph of CSD apparatus described in section 4.2. Motor driven patient bed with pelvis bone sample is also shown.

4.2.1 Assessment of optimum incident spectrum kV_p

An important consideration in CSD is the choice of the incident x-ray spectrum. This sub-section describes the methods used in the choice of incident spectrum based on theoretical predictions from computer simulations and experimental measurements.

4.2.1.0 Computer simulation of CSD gantry

The angular distribution of Compton scatter intensity is described by the

Klein-Nishina equation (§3.3.0) and is a function of incident photon energy. An important factor in the success of CSD is the choice of incident beam kV_p. A prediction based only on the Klein-Nishina distribution of scatter intensity would not account for intrinsic factors such as the attenuation of incident and scattered beams within the measurement site. There is no published work available to indicate the best polychromatic spectrum to use for CSD bone densitometry, although Webber and Kennett (1976) propose an optimum monoenergetic energy of 90 keV, which allows good precision with an acceptable radiation dose based on their analytical calculations.

A Monte Carlo simulation of the CSD gantry geometry was used to find the incident x-ray spectrum which would emit the highest number of single Compton scattered photons from the critical volume when measured at the scatter detector.

This computer simulation used the photon interaction routines described in section 2.2. The geometry was identical to the CSD experimental apparatus described in this section (§4.2), and was comprised of a highly collimated x-ray tube at an angle of 25° to the vertical placed diametrically opposite a collimated sodium iodide scintillation detector (transmission detector). The scatter detector was placed at an angle of 65° below the horizontal between the x-ray tube and transmission detector. CSD requires a single stationary measurement with the critical volume centrally positioned within the trabecular region. The phantom used in this simulation was the circular size 3 phantom. Figure 4.6 shows a schematic diagram of the simulation geometry.

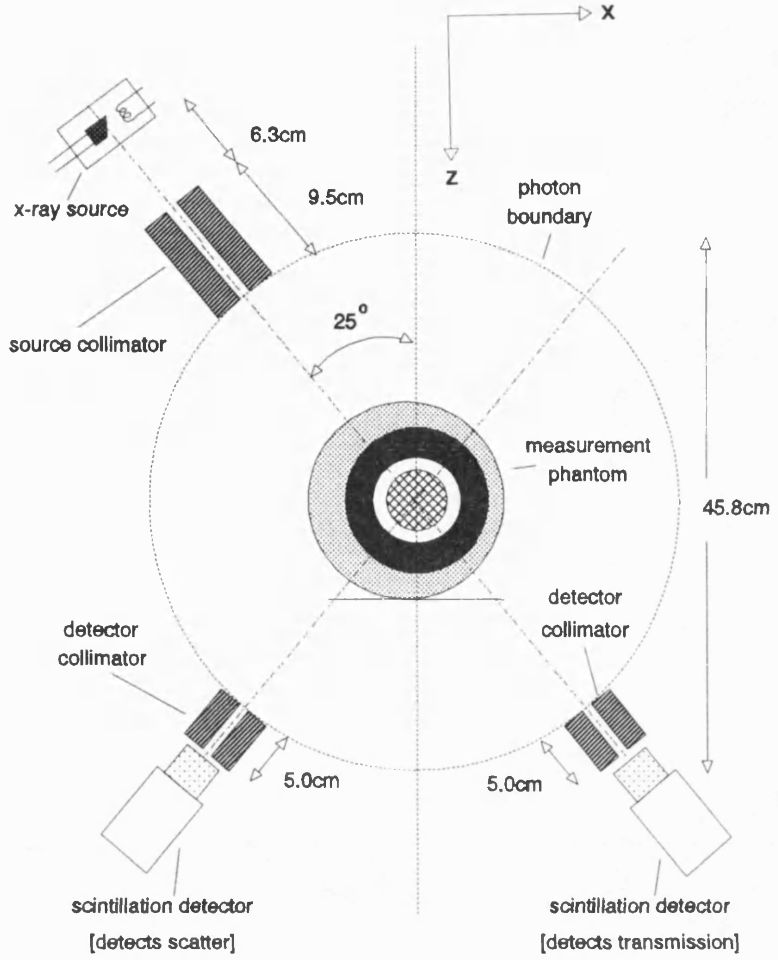

Figure 4.6 Schematic diagram of CSD computer simulation geometry used to assess optimum incident kV$_p$. Source coll. Ø 0.15cm; detector coll. Ø 0.30cm.

4.2.1.1 CSD computer simulation input data

X-ray source spectral data was taken from the HPA Spectral Data Catalogue (Birch *et al*, 1979) and attenuated with 0.33 mm thickness of copper to simulate the filtration used on the gantry. This filtration was used to remove the low energy component of the incident spectrum in order to reduce the dose to the patient. Copper attenuation data was taken from Storm and Israel (1970). Attenuation coefficient data and relative interaction data for the phantom materials were the same as the photon absorptiometry (PA) simulation data in section 2.3.3.

4.2.1.2 CSD computer simulation results

Photons were traced until intersection occurred with the cut-off boundary, a circle defined by the front faces of the collimators. A photon was scored if it intercepted the boundary within the collimator opening and was also within the collimator acceptance angle. Photon scoring was categorised according to several criteria; photons transmitted, photons scattered once and photons scattered more than once. Multiply scattered photons included multiple Compton scatter, multiple Rayleigh scatter and combined Compton and Rayleigh scattering.

Results showed a large transmission count together with a small scatter count at the transmission detector, and a scatter only count at the scatter detector. The variation of single and multiple scatter at the scatter detector with incident spectrum kV_p is shown in figure 4.7, where the scatter count is plotted as a percentage of the incident number of photons. The data was also plotted as the ratio of single to multiple scatter, as in figure 4.8, which was considered as a signal to noise ratio which required optimisation.

The graph in figure 4.7 shows single Compton scatter to be the dominant effect detected at the scatter detector. As kV_p increases the relative incidence of single scatter increases although the rate of increase declines towards the higher kV_p values. This trend is reflected in a rise in the single to multiple scatter ratio, which shows a beneficial increase in the signal to noise ratio.. At higher kV_p values the rate of increase of this ratio decreases with a smaller variation between the 140 kV_p and 200 kV_p spectra.

The increase in single scatter as kV_p rises at the scattering angle at which the detector is positioned is not predicted analytically from collision differentials since Compton scatter becomes more forward scattered as incident photon energy increases. However, the increased energy of the incident photons allows more photons to penetrate the tissue layers and interact in the critical volume. This result is confirmed by Battista and Bronskill (1978) for monoenergetic beams where they demonstrated a net increase in the single scatter fraction because the decrease in attenuation was larger than the decrease in scattering probability. Multiple scatter shows a gradual increase with kV_p at the scatter detector but has a lower rate of increase than the single scatter. This may be due to a larger flux of photons penetrating the phantom, and the higher mean energy of the multiple scatter permitting more photons to escape the phantom and be detected. The increase in scattering events with incident photon energy within a phantom has also been described by Chan and Doi (1986).

These results imply that a higher incident kV_p will result in more single scatter at the scatter detector and an optimised single to multiple scatter ratio. Figure 4.8 also suggests that an incident spectrum between 160 kV_p and 200 kV_p would only produce a slight increase in the single to multiple scatter ratio. Incident spectra within this range would be less susceptible to error introduced by kV_p shifts during a measurement. 5/5

Therefore a high kV_p is desirable for CSD as this increases single scatter with the consequent reduction in statistical error. This is accompanied by an optimised signal to noise ratio. Production of kV_p within the range 130 kV_p to 200 kV_p is limited by the equipment available as these energies are in the radiotherapy range of x-ray production. The x-ray tubes on the CSD gantry are diagnostic equipment with a maximum energy production of 120 kV_p, which would indicate this was the choice of operating kV_p for the CSD evaluations of density. The effect of incident beam kV_p on CSD precision and the experimental confirmation of the Monte Carlo prediction of high incident beam kV_p values are described in section 5.1.1.

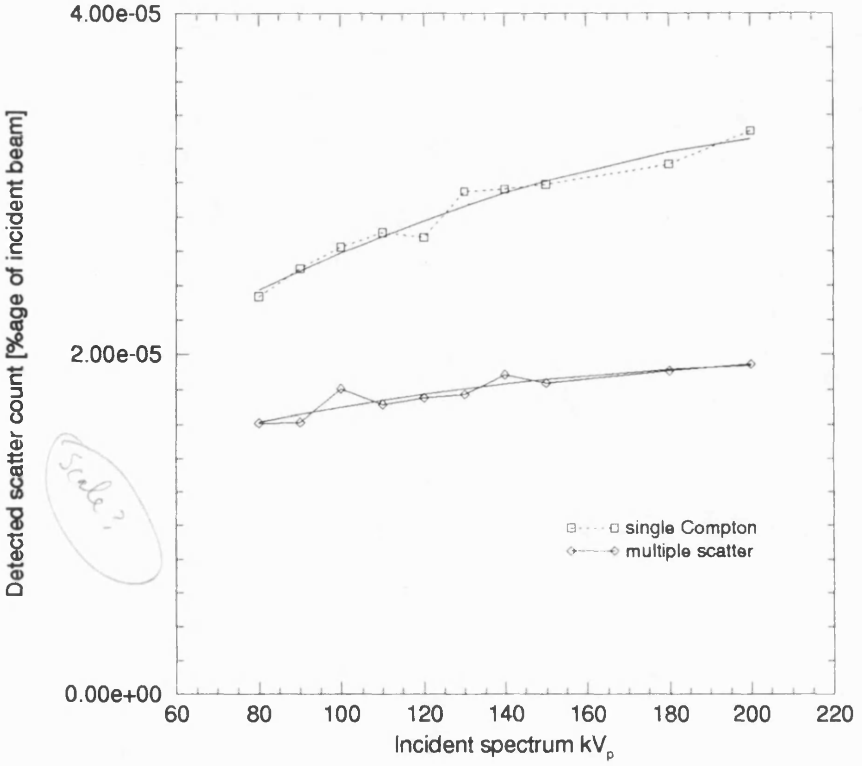

Scale?

Figure 4.7 Computer simulation results showing variation of scatter with kV$_p$ at scatter detector for circular phantom size 3.

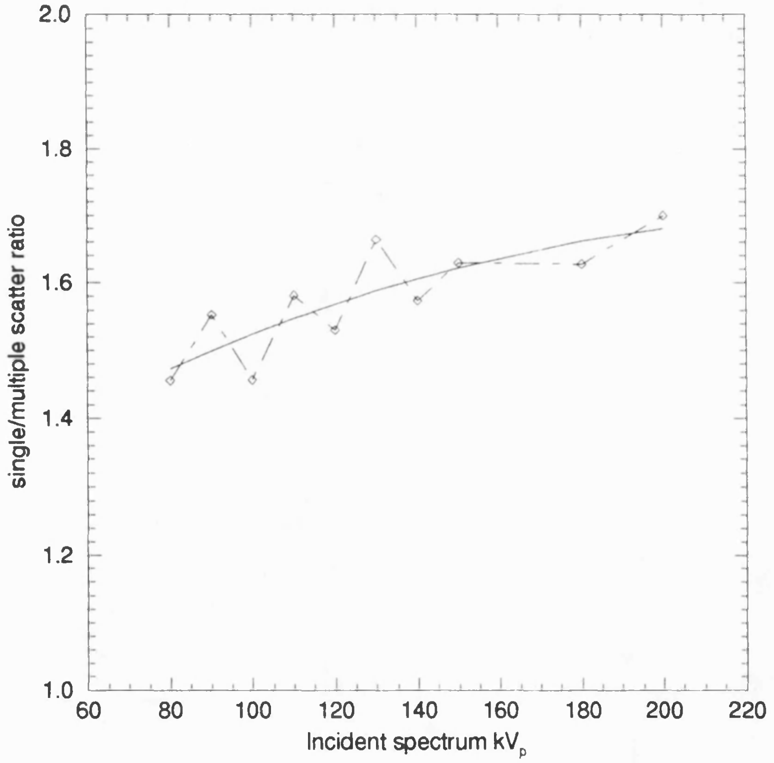

Figure 4.8 Results of computer simulation showing single to multiple scatter ratio variation with kV$_p$

4.2.2 Dimensions of the critical volume.

For CSD in inhomogeneous materials the electron density determined within the critical volume represents an average of the singly scattered photon fluences of all the materials within the volume (Huddleston *et al*, 1979). The size of the critical volume is determined by the collimation of the x-ray tube and scatter detector collimators. A larger diameter x-ray tube collimator will allow a higher count rate and a consequent improvement in counting statistics. However, the size of the critical volume is important in relation to the size of the structures in the trabecular bone region. A volume that is too small will not yield reproducible results as the volume could occupy a marrow space or bone fibre, in which case a small change in positioning will change the CSD bone density value. The requirement for a successful measurement is an average value of density over a sample of trabecular bone fibres and marrow tissue. A critical volume which is too large will introduce errors from poor spatial resolution and may incorporate portions of the outer cortical casing of the bone. Therefore the optimum volume size must be a large enough to encompass a sample of trabeculae and marrow tissue and small enough to remain within the trabecular bone region of the measurement site.

The size of the critical volume has been found from a geometrical analysis using calculus. Physical measurements of the beam spot diameters were also made to confirm the critical volume dimensions.

The critical volume is defined by the intersection of the collimated incident x-ray beam and the collimated beam of single scattered photons entering the scatter detector. The volume of intersection of the two beam cones can be approximated as a volume of intersection of two cylinders where the mid-point of the cylinders coincides with the centre of intersection of the cones. A cylindrical approximation of the incident x-ray beam truncated cone section within the trabecular bone region, as illustrated in figure 4.9, produces a volume error of -0.56% for the densitometer gantry geometry. For the scatter beam cone a cylindrical approximation produces an error of +1.4%.

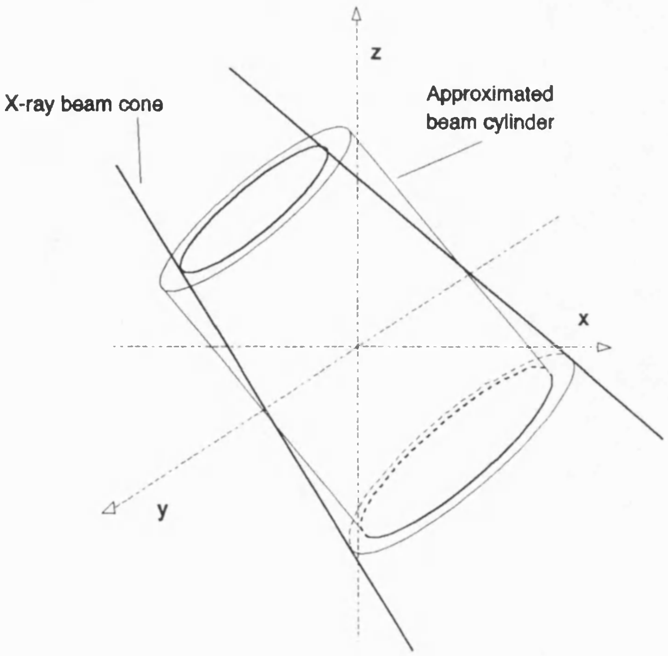

Figure 4.9 Diagram illustrating the approximation of a beam cone section by a cylindrical section.

The calculation of the common volume using calculus can found by using the method of Hubbell (1964). The volume integral is formed -

$$V(r_1,r_2,\beta) = \int_{-r_1}^{r_1} 2\left(r_2^2-x^2\right)^{\frac{1}{2}} . \frac{2\left(r_1^2-x^2\right)^{\frac{1}{2}}}{\sin\beta}\, dx \qquad 4.5$$

where

r_1	radius of cylinder 1 [cm]
r_2	radius of cylinder 2 [cm]
β	axes intersection angle

which can be rendered as a geometric series -

$$V(r_1,r_2,\beta) = \frac{4\pi r_2^3}{\sin\beta} \sum_{n=1}^{\infty} \binom{\frac{1}{2}}{n} \binom{\frac{1}{2}}{n-1} \left(\frac{r_1}{r_2}\right)^{2n} \qquad 4.6$$

Assuming a focal spot of 0.05 cm diameter, the radii of the two cylinders were calculated at the point of intersection by using similar triangles. The source beam radius was 0.33 cm and the detected beam radius was 0.84 cm at this point. Using these values in equation 4.6 produced a volume of 0.57 cm^3 which is an equivalent volume to a sphere of 0.52 cm radius. This is a significant improvement, in terms of spatial resolution, on previous monoenergetic CSD devices for example Webber and Kennett (1976) whose critical volume spherical equivalent radius was quoted as 1.26 cm.

These dimensions were calculated from the gantry geometry and were checked by taking measurements from the x-ray dental film stack used to check the critical volume alignment (§4.2). The film stacks were digitised on a 256 grey-level scanner and displayed on an image processing package (diagram 4.4). The x-ray tubes have a focal spot of 0.05 cm diameter and produce film spots with an umbra and penumbra. The diameter was taken at the point in the penumbra equal to half the maximum film density. The beams were positioned at an angle to the film stacks and so the spots are elliptical in shape, but the short dimension of the ellipse should remain independent of the beam angle and this was the diameter measured. The incident beam spots diameters agreed fairly well with the theoretical values but may indicate a slightly more extended focal spot diameter -

Tube	Theoretical spot diameter [cm]	Measured spot diameter [cm]
A	0.66 ± 0.01	0.71 ± 0.04
B	0.66 ± 0.01	0.68 ± 0.04

Table 4.1 Showing theoretical incident beam spot diameter compared to measured spot diameter at centre of CSD gantry geometry.

The small difference in measured beam spot diameter between tube A and tube B may indicate a slight difference in alignment of the collimator bores with the tube focal spots. Using these values in equation 4.5 to calculate critical volume sizes for beams A and B produces volumes of 0.66 ± 0.07 cm^3 and 0.61 ± 0.07 cm^3 respectively. An average value of 0.64 ± 0.04 cm^3 (equivalent volume to a sphere of 0.54 cm radius) was used as these values did not differ within the limits of measurement.

The size of this critical volume will allow it to be positioned centrally within the trabecular bone region of the lumbar spine and femoral neck without incorporating an unwanted signal from the cortical bone. The radius and ulna measurement sites would not be as suitable because of their small diameter.

4.3 Phantom measurements

Phantoms have been used extensively to test the variation of experimentally evaluated density with the density of known trabecular bone substitutes. They provide a useful and accurate method of simulating the small bone density changes characteristic of osteoporosis.

4.3.0 Solution-containing phantoms

The phantoms had been previously constructed from epoxy resin based materials mixed with mineral powders and particulate fillers (Royle and Speller, 1992). They have been designed to be anthropomorphic substitutes for the lumbar spine and femoral neck measurement sites. A circular phantom was also used for ease of data analysis. Substitutes for fat, soft tissue, cortical bone and trabecular bone were used in the construction as described by Woodard and White (1982).

i. *Circular phantom* : A series of concentric circular phantoms constructed with layers of muscle substitute material over a thin layer of aluminium used as a cortical bone substitute. Trabecular bone substitutes of known density can be inserted into the aluminium tube.

ii. *Femoral neck phantom* : A phantom modelled from the femoral neck region, constructed with a slightly offset outer layer of fat tissue over a thick layer of muscle substitute. The cortical bone is a tapering hollow cone of cortical bone substitute into which four trabecular bone inserts of different densities can be placed.

iii. *Lumbar spine phantom* : A phantom modelled from the lumbar spine region. This phantom was made up of four adjacent slices (14 mm thick) through the lumbar spine region L_1 - L_3 modelled from CT scans and anatomical atlases. The phantom represents several of the internal organs using the requisite tissue substitutes bound together with muscle substitute. The bone is made up of cortical and trabecular substitute with a circular hole bored through the centre to accommodate trabecular bone substitute inserts.

Schematic diagrams of these three phantoms are shown in figure 4.10 and the dimensions listed in table 4.2.

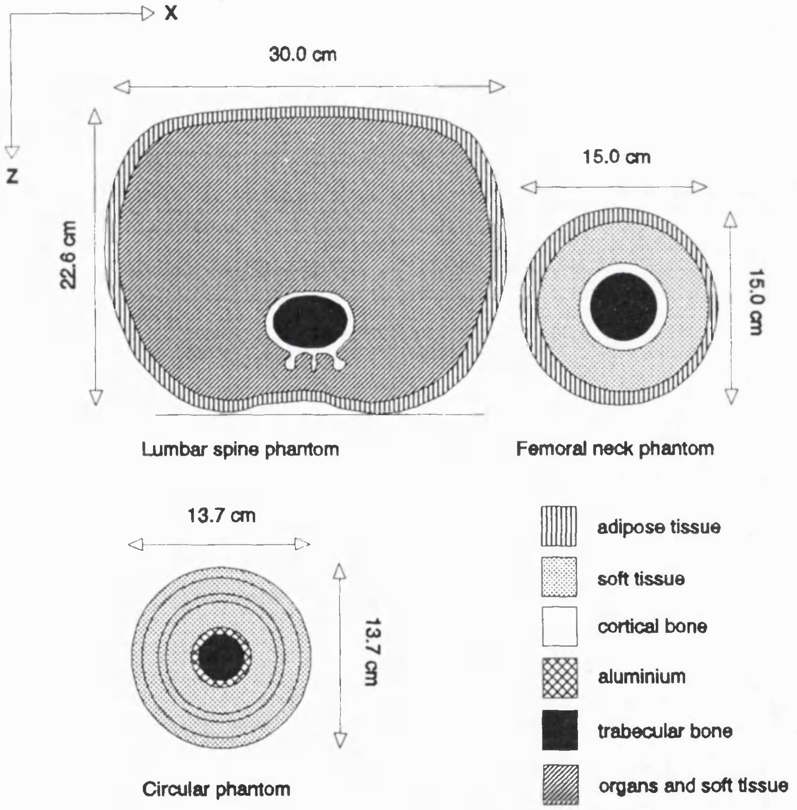

Figure 4.10 Schematic diagram of the solution-containing measurement phantom cross-sections used in the CSD measurements.

Phantom Axis diameter	Circular x[cm] z[cm]	Femoral neck x[cm] z[cm]	Lumbar spine x[cm] z[cm]
Fat tissue	- -	15.00 15.00	30.00 22.60
Soft tissue	6.30 6.30 [1] 7.10 7.10 [2] 10.00 10.00 [3] 13.70 13.70 [4]	11.00 11.00 [b]	27.60 20.00 [a]
Cortical bone	2.00 2.00	6.50 6.50	6.40 4.20
Trabecular bone	1.80 1.80	5.50 5.50	6.00 3.80

[1 2 3 4] refer to different circular phantom sizes

[a] contains internal organ tissue substitutes; offset in the z direction by 0.1cm

[b] offset in the x direction by 0.4 cm

Table 4.2 Showing x and z dimensions of the phantoms used for CSD measurements.

The materials and construction procedure are described in detail by Royle and Speller (1992). The trabecular bone substitutes used were solutions of di-potassium phosphate (K_2HPO_4) dissolved in twice distilled water at room temperature and contained in 20 ml plastic syringes (∅ 18 mm). The density of the solutions was confirmed by measurement in a refractometer which compares the refractive index *n* of the solution with solutions of standard *n* and density.

The relationship of liquid density to *n* is given by -

$$d \propto n - 1 \qquad 4.7$$

where

d physical density [gcm^{-3}]

n refractive index

This expression is valid if the change in *n* is small (Houston, 1943). Figure 4.11 shows the results of the refractometer measurements. This graph confirms that the density of the trabecular substitute solutions measured by the refractometer matches the density predicted by weighing the water and the powders.

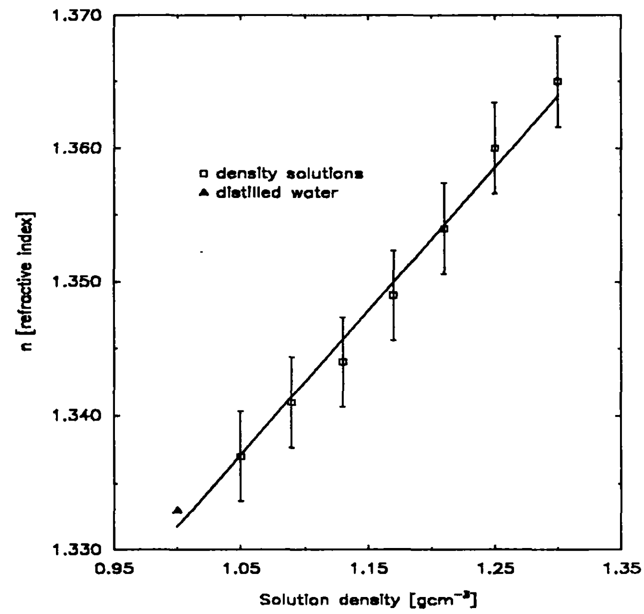

Figure 4.11 Graph of refractive index *n* of phantom trabecular substitute solutions verses solution density.

4.3.1 Bone-containing phantoms

Density measurements on the solution-containing phantoms were limited in their usefulness as they contain an homogeneous trabecular bone substitute. Trabecular bone is an inhomogeneous material subject to variation over small intervals. Density measurements using clinical samples of bone tissue were necessary to measure the precision of the CSD technique. This is especially relevant for the critical volume dimensions and for repositioning errors. A set of phantoms containing bone samples were constructed for this purpose.

These phantoms were fabricated using similar methods to the construction of the femoral neck phantom. Real bone tissue was used in place of the cortical and trabecular bone substitute materials. The bone tissue had been surgically removed from elderly female patients diagnosed as suffering from rheumatoid arthritis and receiving artificial hip replacements. The bone samples had been preserved during transit in formalin, were rinsed with water and allowed to dry for ten minutes before being encased in muscle substitute material, which simulated the surrounding tissue at the femoral neck site. The construction is described by Royle (1992). Five phantoms were made which fitted within an outer layer of soft tissue substitute which simulated the soft tissue and adipose tissue of the upper leg. The following dimensions were used.

Phantom tissue	**Diameter**	
	x [cm]	z [cm]
Soft tissue collar	14.5	14.5
Soft tissue insert	10.0 [a]	10.0
Bone tissue sample	~4-5	~4.5

[a] offset in x-direction by 0.6 cm

Table 4.3 Showing x and z dimensions of the bone-containing phantom used for CSD measurements.

Results and discussion from all the phantom measurements, solution- and bone-containing, are presented in chapter 5, together with a comparison of measurements from other densitometry modalities.

4.3.2 Processing of detector signals

Another important factor in CSD was the selection of the energy windows on the SCA units for the optimisation of the collection of single scatter and the reduction of the contribution of multiple scatter. This sub-section describes how a computer simulation of the CSD gantry was used to separate the contribution of single and multiple scatter in the detected scatter spectrum. These results were then compared with experimental measurements of the scatter spectrum and the data used to set the SCA windows.

4.3.2.0 Computer simulation of scatter spectrum

A similar computer simulation to the optimum incident spectrum assessment (section 4.2.1) was performed using a circular size 3 phantom (§

table 4.2 for dimensions). This size phantom was selected as representing an average size measurement site. The spectrum of the scatter at the scatter detector was collected from the simulation data. This was achieved by appropriately incrementing 1 keV energy bins when a scattered photon was scored. Two spectra were produced separately; the single scatter spectrum which consisted of singly Compton scattered photons and the multiple scatter spectrum.

For comparison with experimentally collected data the data had to be corrected for the resolution of the sodium iodide detectors. Energy resolution measurements of the gantry detectors were made with a range of monoenergetic sources. The data was collected on an MCA (Canberra S100) and the FWHM of the photopeaks measured. The energy resolution results are shown in figure 4.12. Resolution values were interpolated from the graph for the energy range of the computer simulation. The spectral data was then convolved using a Fast Fourier Transform with a Gaussian detector response function of the appropriate interpolated energy resolution. This would allow a comparison with the spectrum collected on the CSD apparatus detectors. The computer simulation spectra are shown in figure 4.13. The single scatter spectrum shows a range of energies between ~45 keV and ~85 keV. This range is produced by the small range of scattering angles subtended at the scatter detectors and the range of energies of the incident photons. The multiple scatter spectrum shows a broader range of energies from ~30 keV to ~85 keV with a broad peak at ~47 keV. From these spectra it would appear that a portion of the multiple scatter at the low energy part of the spectrum could be excluded without affecting the single scatter spectrum. Placing an SCA energy window between 40 keV and 80 keV would have the desired effect. Placing the windows at higher energies would exclude multiple scatter in preference to single scatter but would reduce the single scatter count rate producing poorer counting statistics, longer counting times and higher patient doses. The contribution of multiple scatter in this case should be corrected by multiple scatter correction factors.

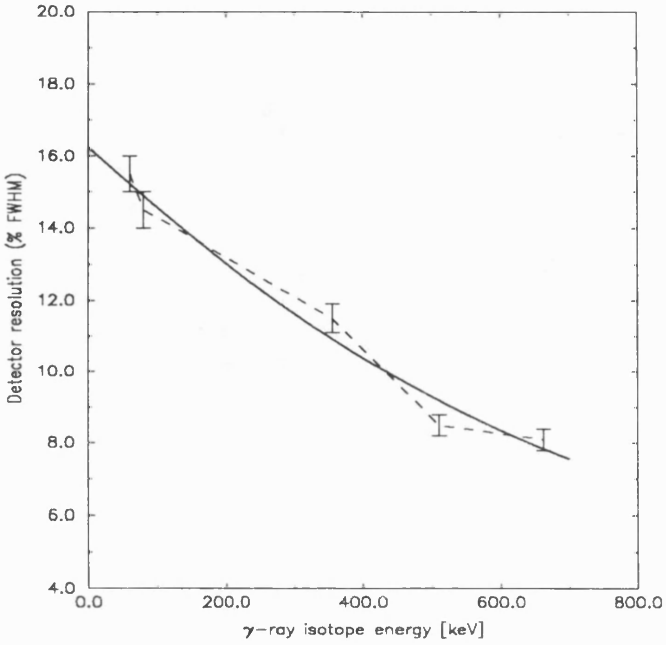

Figure 4.12 Graph showing the energy resolution response of the gantry detectors with energy.

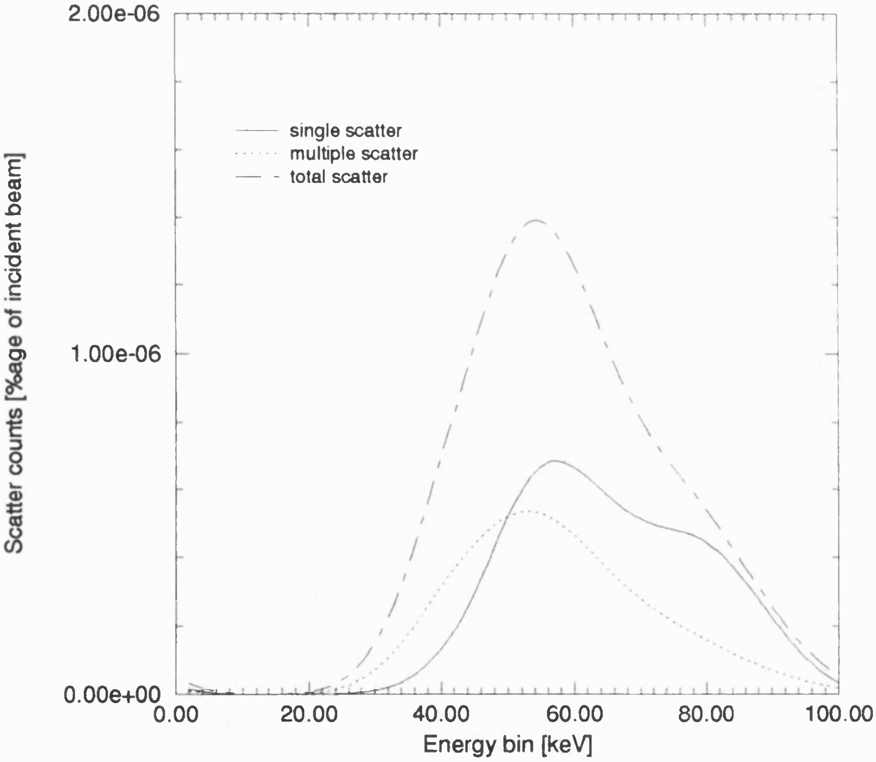

Figure 4.13 Graph showing proportion of single and multiple scatter in scatter spectrum from CSD computer simulation for a circular size 3 phantom for 120 kV_p.

4.3.2.1 Measurement of scatter spectrum on CSD apparatus

The computer simulation spectra were compared with spectra collected from the scatter detectors on the CSD apparatus. Scatter spectra were collected from detectors A and B on an MCA for an exposure period of 60 s. The measurement site used was the size 3 circular phantom containing a 1.17 gcm^{-3} density solution. Both spectra were Wiener filtered (appendix 1) to reduce the noise levels and are shown in figure 4.14. Both spectra exhibited a broad range of scatter photon energies, consisting of single and multiple scatter, with a peak at ~57 keV.

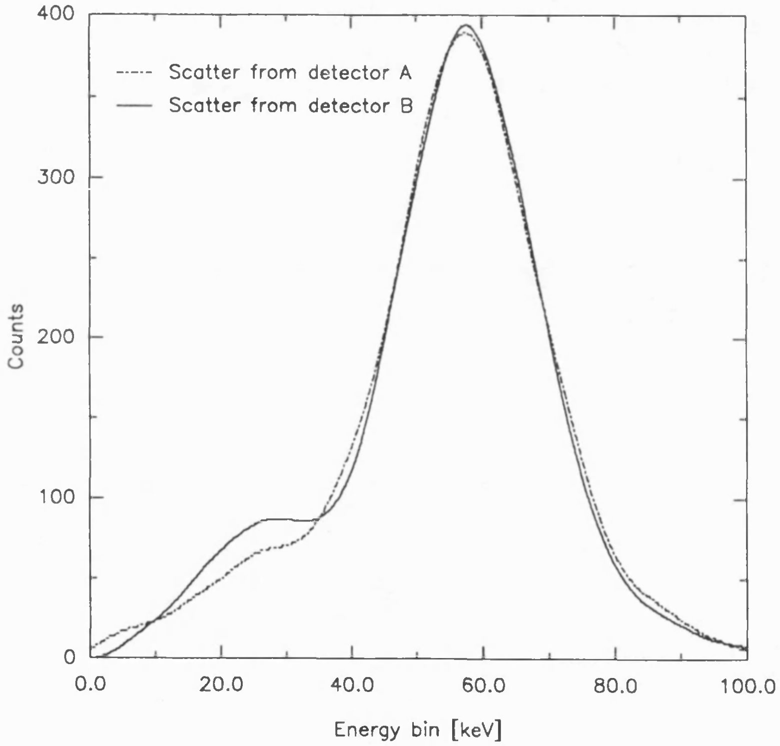

Figure 4.14 Scatter spectra collected from detectors A and B on the CSD gantry. Circular phantom (size 3). Noise level reduced with Wiener filtering.

4.3.2.2 Comparison of simulated and measured scatter spectra

A comparison of the simulated and measured scatter spectra was made in order to assess the correspondence of the simulation with the data collected from the CSD gantry and therefore whether the 40-80 keV SCA window would be applicable. Both sets of data have been normalised for an equal number of counts and are shown in figure 4.15.

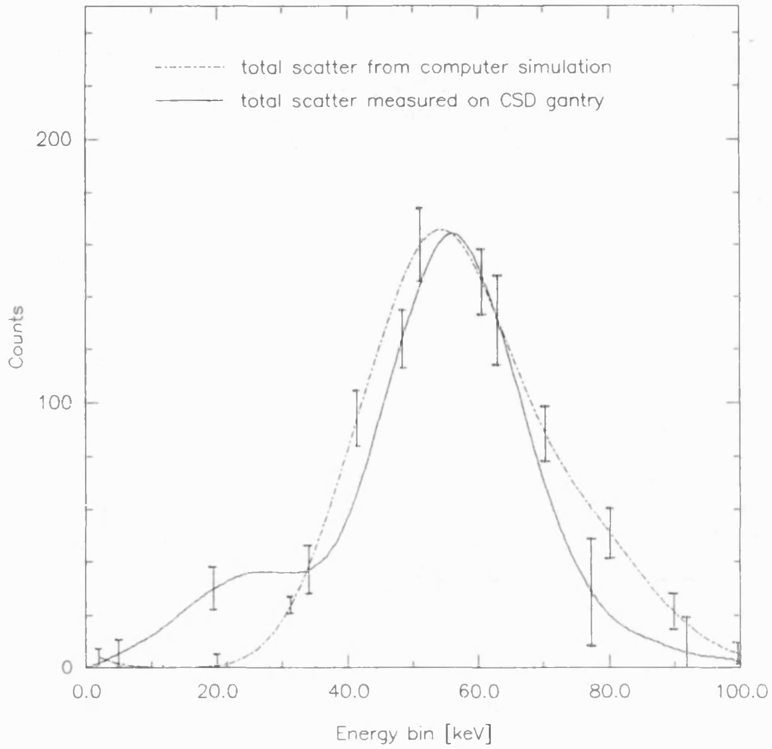

Figure 4.15 Graph showing comparison between the scatter spectrum derived from CSD simulation data and the scatter spectrum collected from the CSD gantry.

This comparison shows the peak of both scatter spectra to be the same within experimental error. The spectrum from the CSD gantry has a low energy component from interactions within the crystal and from scatter from the collimator which were not modelled in the computer simulation. These effects have been documented by De Vries *et al* (1990) for isotopic studies in gamma cameras.

The agreement of the two spectra suggests that the information about the single and multiple scatter spectra provided by the computer model could be used to set energy windows on the SCA units. As expected the energies of the singly and multiply scattered photons overlapped considerably and cannot be separated by these techniques. This was also shown by Battista and Bronskill

(1978). However the energy windows were used to remove the multiple scatter component below the energy of the main single scatter peak.

An energy window was set on each SCA to accommodate the single scatter peak between 40 keV and 80 keV. This was possible by using the SCA output to gate the MCA in order to collect signals from the amplifier which would be admitted by the energy window on the SCA (figure 4.16). This technique allowed the energy window to be visualised on the MCA and figure 4.17 shows an example of the windowed scatter spectrum.

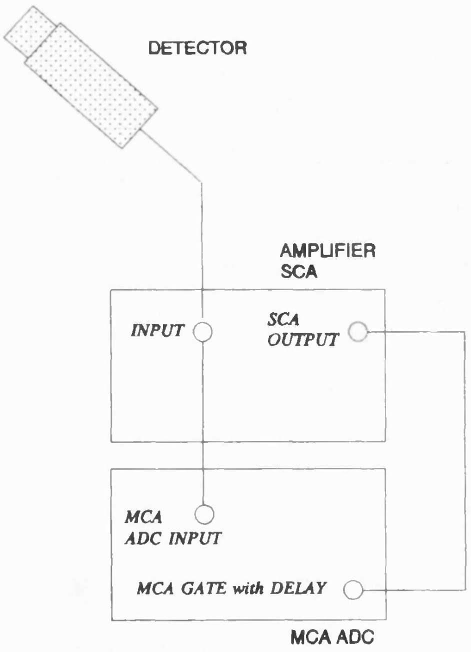

Figure 4.16 Schematic block diagram of electronic elements used to gate MCA for energy window determination.

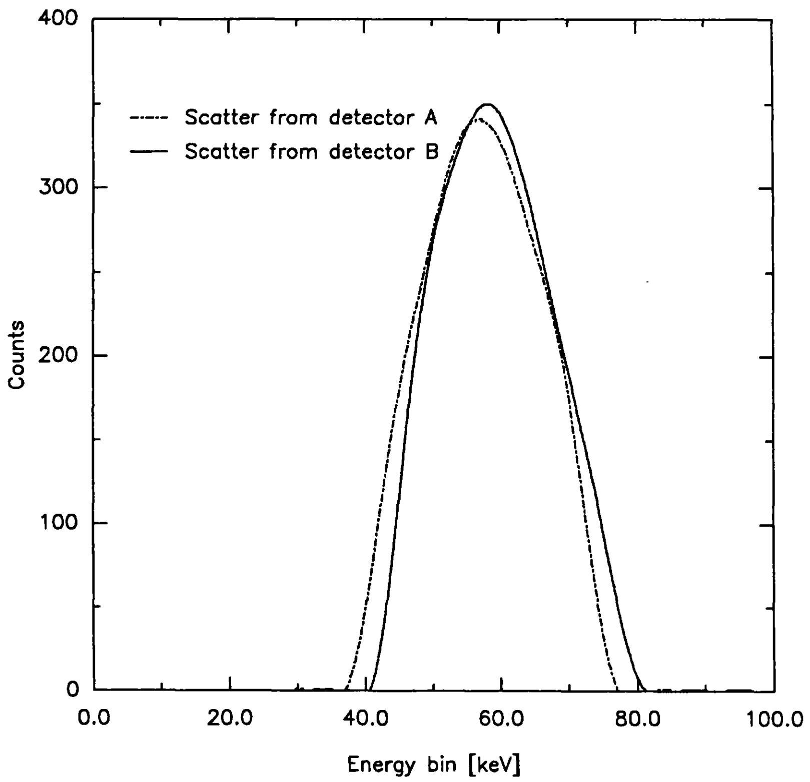

Figure 4.17 Scatter spectra collected from detectors A and B on the CSD gantry. Data collection on the MCA has been gated by the SCA outputs to show energy windowing.

4.3.3 Phantom bone density measurement procedure

Measurements on the circular, femoral neck and lumbar spine phantoms all involved a similar basic procedure. The critical volume location with respect to the gantry had been previously found during the alignment test. A vertical laser beam was positioned to shine through the punctured film spots (§ 4.2.0) which indicated the position of the volume in the horizontal x-y plane. A ruler was used to measure the height to the centre of the volume in the vertical z-x plane (see figure 4.5). The phantom was positioned on supports with the bone centre in line with the laser beam and raised or lowered until the volume was centred in the trabecular substitute region. This technique ensured the critical volume was in the centre of the trabecular substitute region and also enabled accurate repositioning for repeat readings necessary for precise long term measurements. This procedure would not be possible for measurements on patients and a technique for locating the critical volume within the trabecular region of the patient is described in section 4.3.4.

The detectors were calibrated with an Americium-241 [Amersham AMR.151] isotope source spectrum collected on a Canberra PC-based System 100 Multi-Channel Analyser (MCA). The SCA windows were set to the values calculated in section 4.3.2.

Experiments were conducted to find the lowest exposure time which produced an acceptable measurement precision of between 1% and 2%. The results of these experiments are presented in chapter 5. An exposure of thirty seconds was selected from these measurements and used for each x-ray tube during each measurement.

4.3.4 Scout scans

The positioning of the critical volume within the solution-containing phantoms was relatively straight forward as the trabecular substitutes were visible. However, the position of the bone within the bone-containing phantoms and within patients cannot be visualised. A scout scan of the measurement site was made in two directions to locate the bone position. This involved x-ray tube B and detector B on the densitometer gantry and the MCA system set in Multi-Channel Scaling (MCS) mode. The phantom was placed at approximately the correct height on the couch at the start position corresponding to channel 0 on the MCS. X-ray tube B was activated and the MCS collection started. This simultaneously activated the motor driving the scanning couch which moved the phantom along the x-axis through the beam to the stop position. The scan took 10 seconds to move 29.0 cm which ensured the full width of the phantom was scanned. A schematic diagram of the scout scan apparatus is shown in figure 4.18.

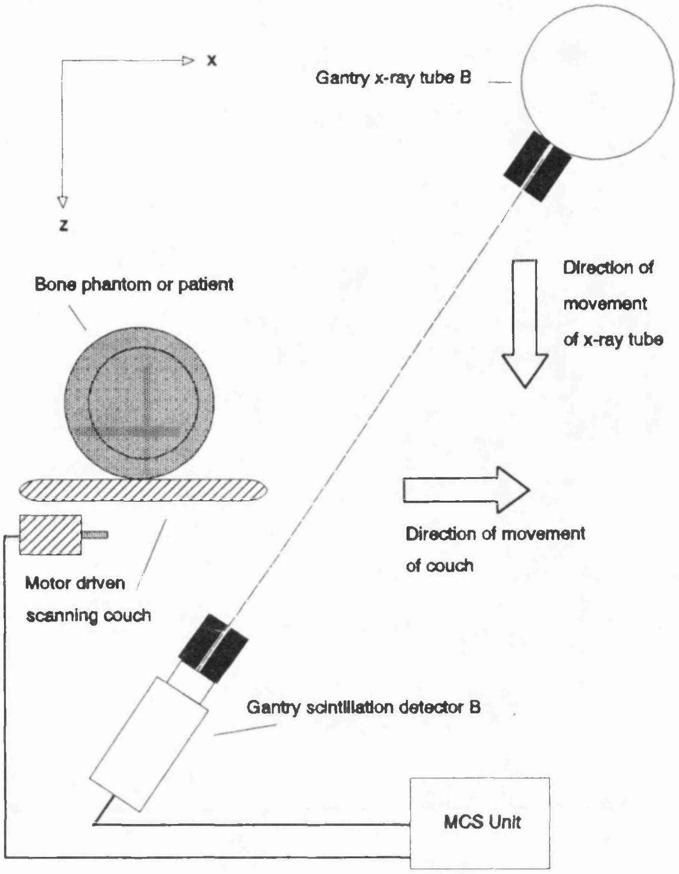

Figure 4.18 Schematic diagram of CSD apparatus components used for scout scans.

The scan from the MCS was plotted out and is shown in figure 4.19. A Wiener filter (appendix 1) was applied in order to reduce the noise. Several features of the phantom are visible in the scan, the most important being the absorption troughs due to the cortical bone shell at the edges of the bone. These troughs clearly mark the bone extremities. By converting the bone position in channel numbers into stepper motor pulses the critical volume could be positioned at the centre of the bone.

The same procedure was then applied to the z-axis of the phantom to produce a two dimensional position for the critical volume. The y-axis position was kept constant at the mid-point of the phantom.

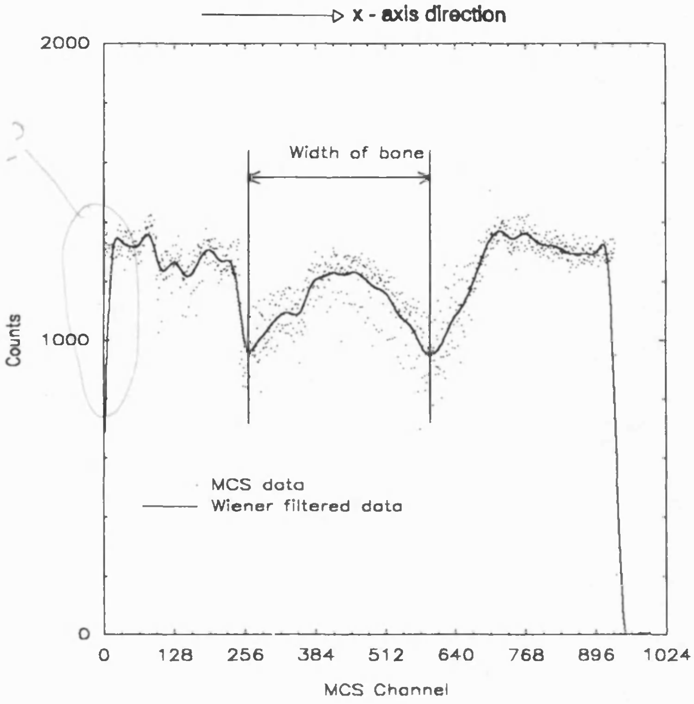

Figure 4.19 Scout scan of femoral neck phantom containing bone tissue sample. Raw data and Wiener filtered data is shown. [Exposure 120 kV_p; 7 mA; 10s]

4.3.4.0 Scout scans of bone tissue

Scout scans of the phantom materials indicated that this technique would be suitable for positioning the critical volume within the trabecular region of the bone. In order to ensure that the technique would be applicable to patients, scout scans of real bone tissue were performed. Also, in patient studies there are other bones present around the measurement site which may hinder the scout scan. To simulate more accurately the bone architecture of a patient, a pelvis and femur were used as subjects for a scout scan (figure 4.20). After several scans along the x-axis direction, using a range of different incident beam kV_p values, it was discovered that a beam of 70 kV_p gave the clearest indication of the bone limits, due to the preferential attenuation of the photons in cortical bone. Scans along the z-axis direction were not so successful due to the limited range of movement of the gantry in that direction. As a result the positioning of the patient in the z-axis direction was accomplished by using the end of the greater trochanter as a landmark, as this can be readily found on a patient. The landmark was aligned with a marker on the gantry to align the centre of the bone with the critical volume position.

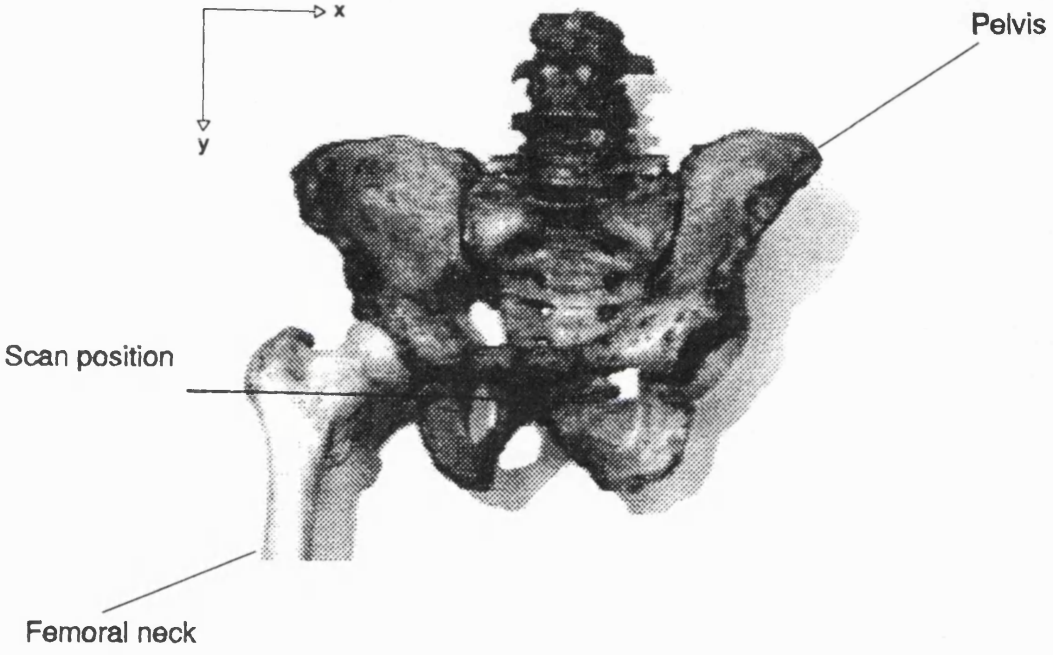

Figure 4.20 Photograph of pelvis and femur bones used in scout scans. Scan position is marked as a solid line.

The top of the greater trochanter was also used a landmark for the positioning of the critical volume along the y-axis direction, as the gantry has no movement in that direction. Finally a scout scan along the x-axis direction is performed in order to finally position the critical volume within the centre of the bone. Figure 4.21 shows typical scans of the upper femur.

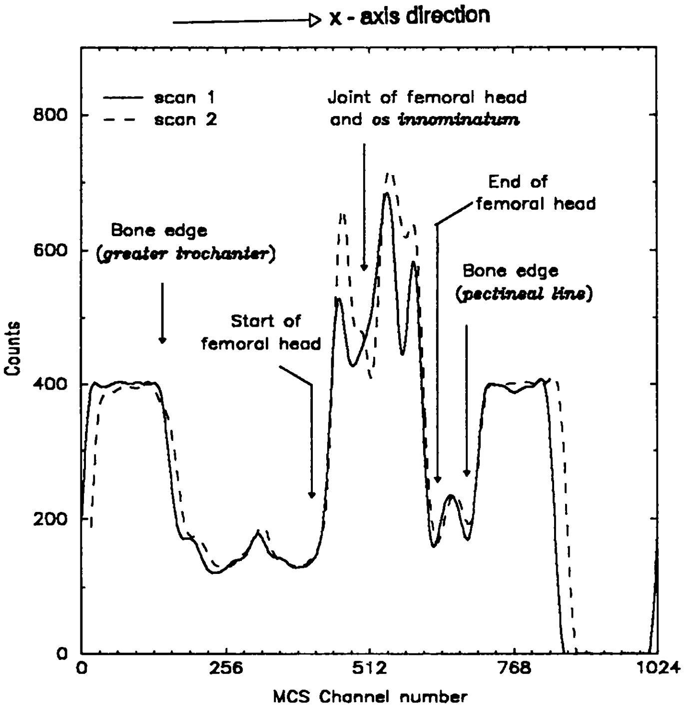

Figure 4.21 Typical Wiener filtered scout scan of the upper femur and pelvic region. Bone limits of the femur are marked. [Exposure 70 kV$_p$; 7 mA; 10 s]

4.4 *bcf* values for the CSD apparatus

The theory of CSD (§4.1) requires a bias correction factor *bcf* to correct for errors introduced by beam polychromacity and measurement geometry. The *bcf* values have been found to vary with sample size, sample density and scattering angle (Duke and Hanson, 1984). Koligliatis (1990) proposed that the corrections for these effects on the CSD gantry are insignificant and can be disregarded. By far the most important source of error in CSD are multiply scattered photons entering the scatter detector (Duke and Hanson, 1984; Speller and Horrocks, 1988). This effect can be resolved by the use of multiple scatter correction factors.

4.4.0 *mcf* theory

Battista *et al* (1977) proposed that a possible technique to assess the contribution of multiple scatter would be to take measurements using the same measurement geometry as the CSD apparatus. The scatter from the critical volume would be excluded by collimation, therefore only allowing multiply scattered photons to enter the scatter detector. Alternatively the multiple scatter from a phantom could be measured when the trabecular region of the phantom is removed, which would detect multiple scatter originating from around the critical volume. However, neither of these techniques could detect multiple scatter originating from or crossing through the critical volume. The advantage of computed *mcf* values is that they are able to include this contribution.

The spectrum of multiply scattered photons spans a wide energy range due to energy degradation following numerous Compton interactions. A large number will have energies identical to those of singly scattered photons. Battista and Bronskill (1978) have calculated spectra which confirm that multiple scatter contamination cannot be eliminated by simple high-resolution spectrometry. However the contribution by multiple scatter below the single scatter energy range can be eliminated by energy windowing the detector signals and has been described in section 4.3.2. Multiple scatter is a complex, highly geometry dependent problem which is best assessed by Monte Carlo computer simulation.

If a single tube and detector CSD system is considered then -

$$\rho = k\frac{S_1}{T_1} \qquad 4.8$$

where

k	calibration constant
ρ	physical density [gcm^{-3}]
S_1	single scatter counts
T_1	transmitted counts

In an experimental situation the detected scatter counts would comprise of both single and multiple scatter, in which case density can be expressed as -

$$\rho = k\frac{(S_1+S_m)}{T_1}.mcf \qquad 4.9$$

where

S_m multiple scatter counts

mcf a factor to correct density for multiple scatter

By combining equations 4.11 and 4.12 an expression can be formed which produces the multiple scatter correction factor (*mcf*).

$$mcf = \frac{S_1}{(S_1 + S_m)} \qquad 4.10$$

Application of this factor should correct for the effects of multiple scatter on experimental CSD measurements. The behaviour of the factor cannot be determined analytically but can be investigated by the use of Monte Carlo simulations of the experimental conditions under which the factor is to be applied.

4.4.1 *mcf* calculation program description

Calculation of the *mcf* values for use on the CSD apparatus were made according to the formula in equation 4.10. This required a Monte Carlo computer simulation of the CSD apparatus which could separate single and multiple scatter. The simulation was similar to those described in sections 4.2.1, 4.2.2 and 4.3.2. The variation of the scatter around the gantry was charted by positioning a detector at 1° intervals around the cut-off perimeter. Photon scoring was sub-divided according to photon history, and were; transmitted photons, singly scattered photons and multiply scattered photons.

Simulations were performed for the three solution-containing phantoms over a range of sizes in order to assess the change in *mcf* values with different size patients, measurement sites and with patient size changes.

Energy deposition at the location of each interaction was also scored according to the region in which it occurred. This information was used to calculate the variation of absorbed energy within the tissues of the measurement site as size varied, and is described in the next section (§4.5).

Figure 4.22 shows the variation of single scatter and the two components of multiple scatter between the scattering angles 200° and 210° as computed by the Monte Carlo simulation. This shows single scatter to be the dominant effect at the scatter detector (angle of 205°). This agrees with the previously calculated data used to assess the optimum kV_p in section 4.2.1.

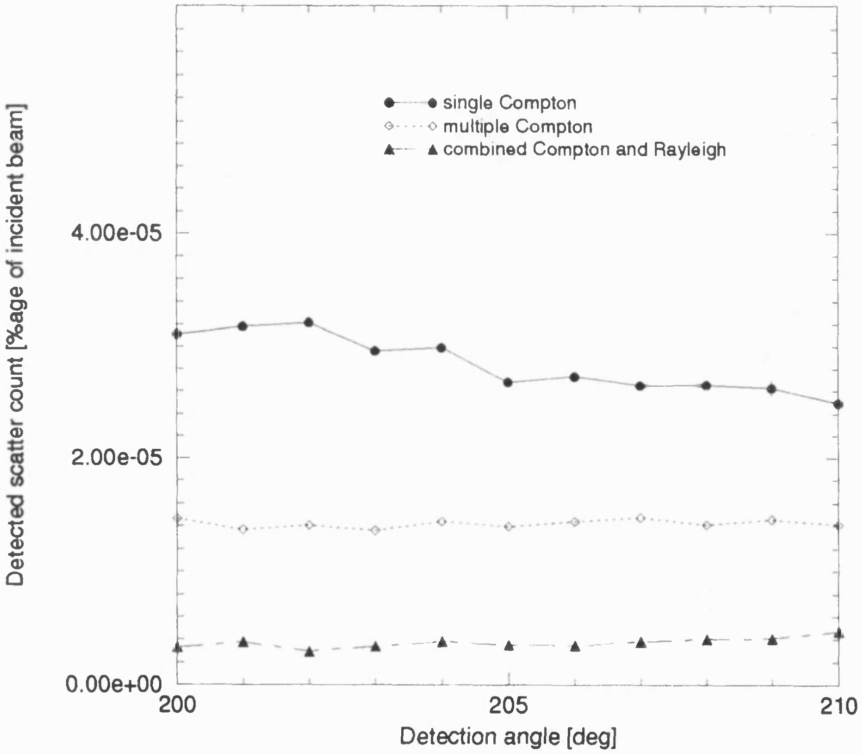

Figure 4.22 Shows variation of different scatter detected around the CSD gantry from the computer simulation. X-ray beam of 120 kV_p incident on a size 3 circular phantom.

The position of the scatter detector on the gantry corresponds to the 205° scattering angle in the computer simulation. The size of the phantom is one of the influencing factors in the amount of single and multiple scatter during a measurement (Battista and Bronskill, 1978). Graphs showing the relative amounts of single and multiple scatter are shown in figures 4.23 to 4.25

These graphs show similar behaviour with detected scatter decreasing as phantom size increases. All the phantoms show single scatter decreasing at a slightly faster rate than the multiple scatter. For the small diameter phantoms the main component of the multiple scatter is multiple Compton scatter. As phantom size increases the proportion of combined Compton and Rayleigh scatter multiple scatter becomes more significant. This due to a larger volume of irradiated tissue being available for scattering interactions to occur which increases the probability of multiple scattering interactions. The increase in multiple scatter events with phantom size has been documented by Chan and Doi (1986).

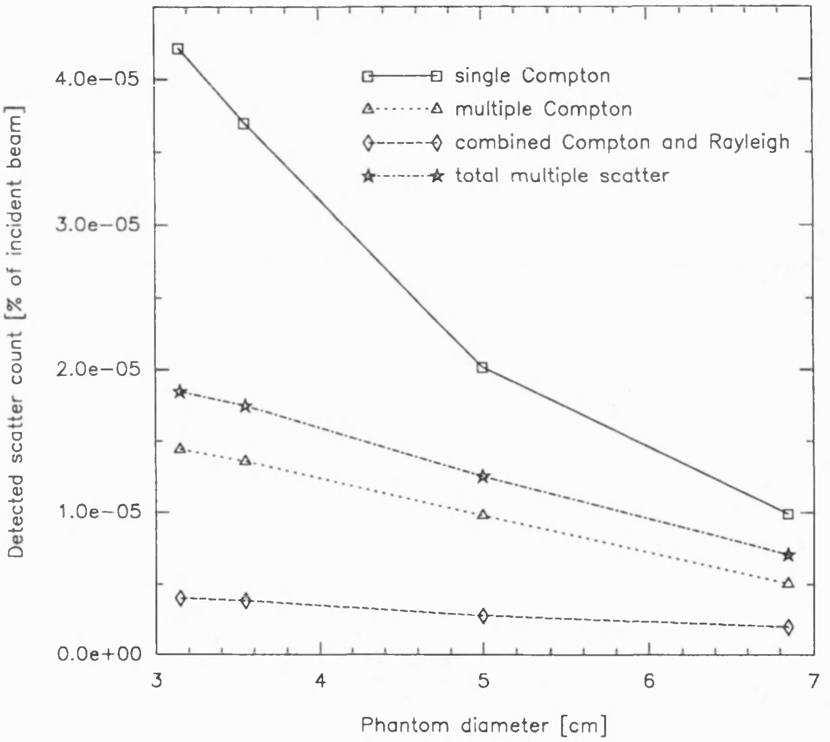

Figure 4.23 Change of incidence of different scatter at scatter detector on CSD gantry (angle 205°) for a circular phantom measurement.

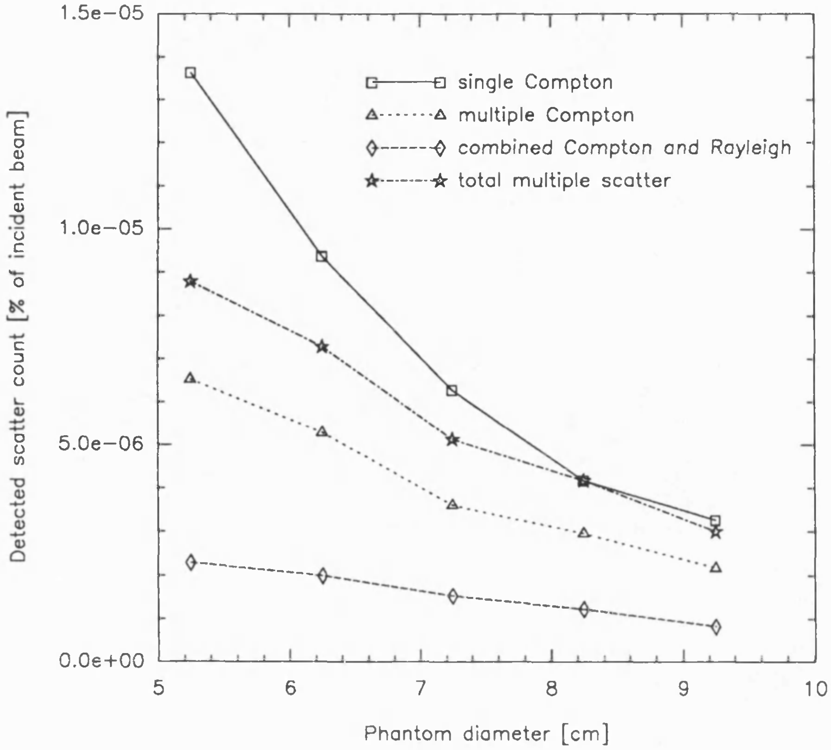

Figure 4.24 Change of incidence of different scatter at scatter detector on CSD gantry (angle 205°) for a femoral neck phantom measurement.

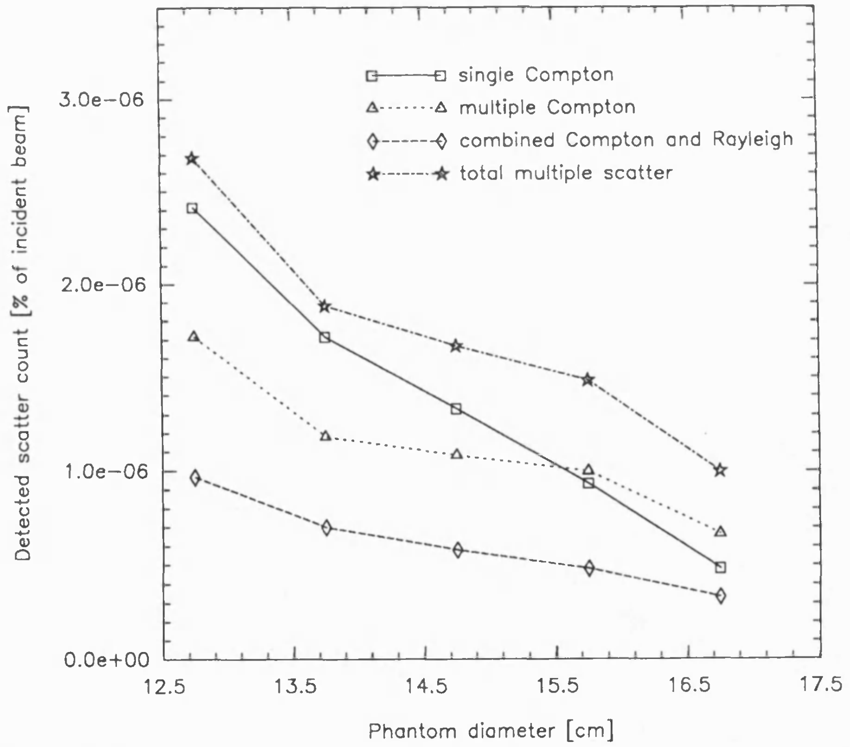

Figure 4.25 Change of incidence of different scatter at scatter detector on CSD gantry (angle 205°) for a lumbar spine phantom measurement.

4.4.2 Computed *mcf* values

In order for the *mcf* values to be applicable for the experimental CSD measurements taken on the gantry the *mcf* values were calculated using photons within the single scatter energy window set on the CSD apparatus (section 4.3.2). Any scatter energies outside these energy thresholds were excluded from detection and did not require correction. Spectral data from the computer simulation was used to calculate the single scatter and multiple scatter counts within the threshold limits. The *mcf* values were then calculated using equation 4.13 and are tabulated in table 4.4. Simulation of a range of phantom sizes allows application of the *mcf* values to a range of patient sizes. This would also allow the correct *mcf* to be applied if the patient size changes during long-term serial measurements which are not corrected for in other current techniques. eg DPA, DEXA (§ chapters 2 and 3).

Circular phantom		Femoral neck phantom		Lumbar spine phantom	
Radius x-axis [cm]	*mcf* value	Radius x-axis [cm]	*mcf* value	Radius x-axis [cm]	*mcf* value
3.15	0.696 ± 0.008	5.25	0.608 ± 0.012	13.0	0.474 ± 0.029
3.55	0.680 ± 0.010	6.25	0.563 ± 0.015	14.0	0.477 ± 0.033
5.00	0.617 ± 0.013	7.25	0.550 ± 0.019	15.0	0.444 ± 0.038
6.85	0.585 ± 0.016	8.25	0.500 ± 0.023	16.0	0.386 ± 0.050
		9.25	0.521 ± 0.026	17.0	0.326 ± 0.062

Table 4.4 Table showing computed *mcf* values for different phantom sizes.

These values show that the smaller diameter phantoms produce a larger proportion of single scatter to multiple scatter. This agrees with the prediction that a larger irradiated volume of tissue will produce a greater proportion of multiple scatter to single scatter, as shown in figures 4.23 to 4.25. Consequently a small diameter phantom has a large *mcf* which steadily decreases as phantom diameter increases. This is apparent in the tabulated values of *mcf* shown in table 4.4.

A graph of the *mcf* values versus phantom size shows the rate of decrease in *mcf* values gradually becomes higher as the phantom diameter increases (figure 4.26). This can be seen especially in the lumbar spine where the range of *mcf* values over a large range of tissue thicknesses is wider than the smaller phantoms where the tissue thicknesses are lower.

These values compare favourably with values computed by Speller and Horrocks (1988) for CSD. At a scattering angle of 50°, the comparable position of the scatter detector in their study; the value for a 15.0 cm x-axis radius lumbar spine is ~0.40 and for a 7.25 cm x-axis femoral neck is ~0.55. These values were computed for an x-ray spectrum of 100 kV_p and the values in table 4.4 are computed for an x-ray spectrum of 120 kV_p. Also the geometry of the CSD apparatus used in their study is different from the experimental apparatus simulated above, and this would account for the slight difference in the values quoted here, although overall they show a good agreement.

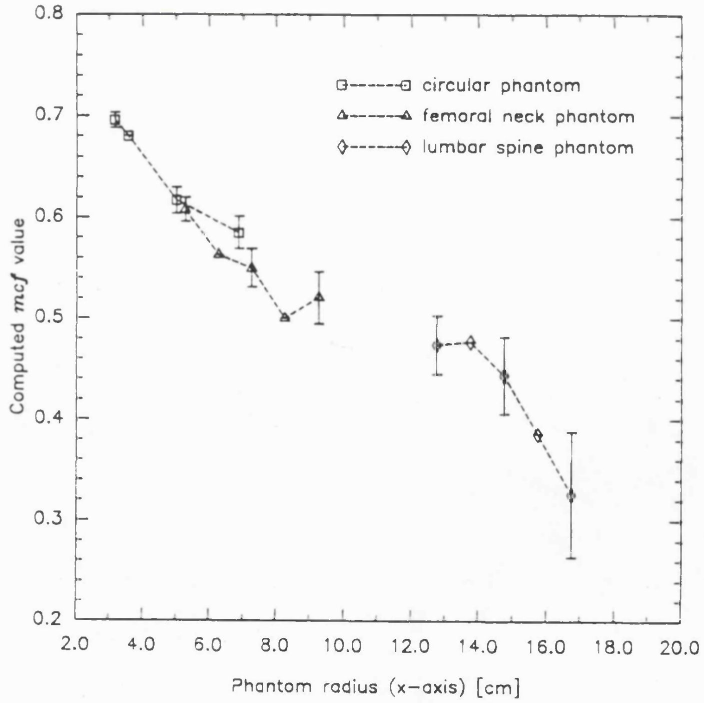

Figure 4.26 Graph showing *mcf* values for the computer simulations of the three measurement phantom simulations.

4.5 CSD dosimetry

The use of CSD for patient measurements requires careful dose measurements to be made before exposing patients. This section describes the estimation of absorbed energy in the tissues of the measurement sites from Monte Carlo computer simulation data. Also described are *in vitro* experimental measurements of exposure and the calculation of absorbed dose in phantoms during a CSD bone density measurement. These measurements were made with TLD chip dosimeters.

4.5.0 Absorbed dose

When directly ionising radiation such as x-ray photons impart energy to tissue there are two stages to consider. The first stage is the release of energy at the point of interaction which is measured as kerma During this process the uncharged particles transfer energy E to the kinetic energy of the subsequent charged particles. Kerma can be defined as -

$$K = \frac{dE_{tr}}{dm} \tag{4.11}$$

where

K	kerma [$\mathrm{Jkg^{-1}}$]
dE_{tr}	sum of the initial kinetic energies liberated [J]
dm	mass of the material [kg]

The second stage is the subsequent imparting of energy to the surrounding tissue which is determined by the range of the charged particles in the material. This process determines the absorbed dose to the tissue which can be defined as -

$$D = \frac{d\bar{\epsilon}}{dm} \qquad 4.12$$

where

D	absorbed dose [Jkg^{-1}]
$d\bar{\epsilon}$	mean energy imparted by ionising radiation [J]
dm	mass of the material [kg]

In the Monte Carlo simulations the kerma was recorded for each tissue region within the phantoms. In the simulations the photoelectrons released during photoelectric interactions and during Compton scatter were assumed to be locally absorbed. At the diagnostic energies which these interactions occurred this was a reasonable assumption and so kerma would be considered equivalent to absorbed dose. However, the mass of phantom material in which the interactions occurred was not accurately known and so absorbed dose estimates from the Monte Carlo data was not possible. An indication of the possible doses could be found by examining the trends of the absorbed energy within the phantom tissues.

4.5.1 Variation of absorbed energy with kV$_p$

The absorbed energy for each region of the phantoms was calculated from the computer simulation data. The graph in figure 4.27 shows the variation of absorbed energy in each phantom material with kV$_p$ expressed as a percentage of the total incident beam energy. A large proportion of the absorbed energy was due to photoelectric absorption in the materials. At low kV$_p$ values the absorption in the cortical region was very high and was also high for the lower Z materials such as soft tissue and trabecular bone. As kV$_p$ increased the energy absorption was lower in all materials but was especially reduced in the cortical region. This was due to a lower incidence of photoelectric absorption at higher photon energies.

not 'soft tissue'!

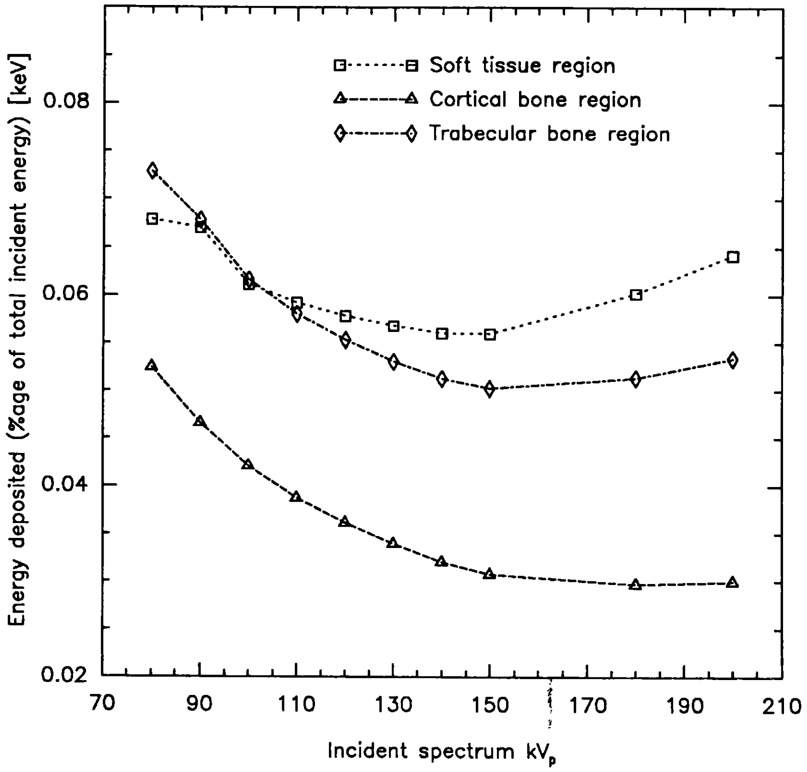

Figure 4.27 Variation of absorbed energy with kV_p in circular phantom size 1

4.5.2 Experimental dose measurements

Absorbed doses reported from CSD devices using x-ray sources (Duke and Hanson, 1984) range from 960 µGy to 100 mGy and are usually below 2 mGy.

Experimental dose measurements were made on four of the previously described test phantoms containing a 1.17 gcm^{-3} density solution. The solution was present to ensure that any back-scatter would be included in the exposure measurement. Measurements were made with TLD chips placed on the surface of the phantoms. The beam entrance point was found using a dental x-ray films attached to the phantom surface. The chips were then positioned at the spot centre and exposed for 30 s with a 120 kV_p x-ray beam filtered with 0.33 mm copper to simulate a density measurement (figure 4.28). This provided a measurement of the exposure the phantom is subjected to during a density measurement. These measurements were repeated three times to eliminate any positioning error. The dose measurements for the scout scans were made by exposing the chips for a 10 s duration.

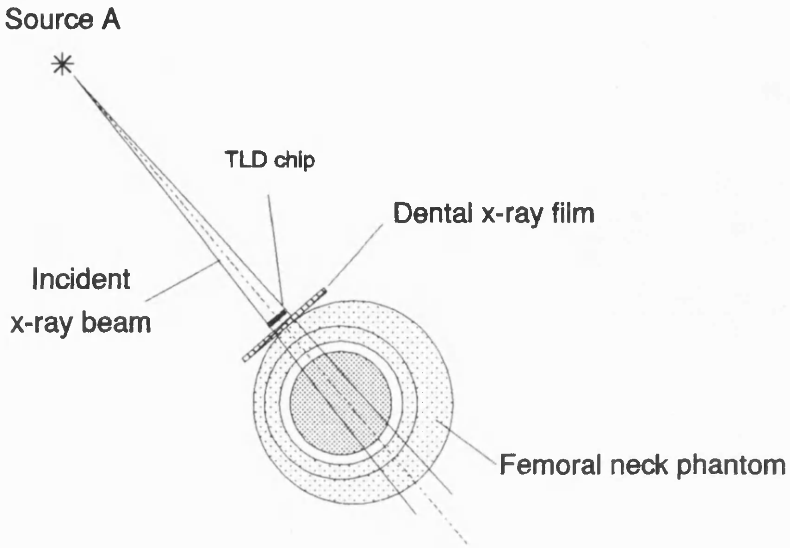

Figure 4.28 Schematic diagram showing position of TLD chips on phantom during dose measurement.

All the TLD chips were read out on a Toledo 654 TLD Reader calibrated for exposure to 120 kV_p x-ray radiation. The variation of the TLD chip response was assumed to be ± 10% together with uncertainties introduced from reading out and calibration errors made an error of ± 20% possible.

To assess the impact of a radiation technique on the exposed organs of the body, an effective dose (E) is usually used to appraise the dose, and is defined in ICRP no.60 (ICRP, 1991). For effective dose the equation describing the equivalent dose is -

$$H_T = \sum_R W_R . D_{T,R} \tag{4.13}$$

where

H_T equivalent dose
$D_{T,R}$ absorbed dose averaged over tissue or organ
W_R radiation weighting factor

In this case the value of W_R is unity as x-ray photon radiation is being considered. The effective dose is then -

$$E = \sum_T w_T . H_T \qquad 4.14$$

where

E	effective dose
W_T	tissue weighting factor the values of W_T are taken from ICRP no.60 (1991) and are; gonads = 0.20, red bone marrow (RBM) = 0.12; bone surface = 0.01.

The beam diameter at entry is ~0.3 cm and ~0.4 cm at exit from the femoral neck phantom. To assess the contribution of scatter to dose within the phantom a series of film exposures were made at 1 cm intervals within a 10 cm block of perspex. A 256-grey scale image scanner was used to view the spots on an image processing package on a Sun workstation. Measurements of the spots indicated no significant film-blackening outside a spot diameter of 0.6 ± 0.05 cm. A slice of tissue of 0.7 cm thickness through the site was assumed for tissue mass calculations.

For the soft tissue a volume of 116 cm^3 is irradiated, therefore the mass irradiated = 0.116 kg.

For the RBM the total organ mass is 1.498 kg (ICRP no.23, 1974). The RBM is assumed to compose 74% by volume of the trabecular bone region. For the trabecular bone a volume of 4.95 cm^3 is irradiated,
therefore the RBM volume = 3.66 cm^3
therefore the RBM mass = 0.0034 kg.

The total organ mass for the cortical bone is 4.0 kg (ICRP no.23, 1974). For the cortical bone, a volume of 1.42 cm^3 is irradiated,
therefore the bone mass = 0.0026 kg.

The surface dose measured by the TLD chips on the femoral neck phantom is 4.4 ± 0.5 mSv. Estimating the average absorbed dose in the phantom from data published by Pye *et al* (1990) gives a value of 3.6 ± 0.5 mSv for the average absorbed dose and for the dose at the phantom mid-line.

	Circular x-axis Ø 13.7cm TLD dose [mSv]	Femoral neck x-axis Ø 15.0cm TLD dose [mSv]	Lumbar spine x-axis Ø 30.0cm TLD dose [mSv]
CSD dose	3.6 ± 0.5	4.4 ± 0.6	5.3 ± 0.7
Scout dose	-	1.5 ± 0.3	1.9 ± 0.3

Table 4.5 Table showing measured surface dose values to the solution-containing phantoms from TLD chip measurements

To find the effective dose for a femoral neck CSD examination (30 s exposure) the following calculation was made using the mean absorbed dose in the phantom;

$$E = \left(3.6\times10^3\times\frac{0.116}{70}\times0.3\right)+\left(3.6\times10^3\times\frac{0.0034}{1.498}\times0.12\right)+\left(3.6\times10^3\times\frac{0.0026}{4.0}\times0.03\right) = 2.8\,\mu Sv$$

For a CSD measurement two stationary measurements of 30 s exposure are required producing an effective dose of 5.6 ± 0.5 μSv. Also required are two scout scans of 10 s exposure. The calculation for the scout scans neglects the bone contribution to the effective dose calculation as this comprises a small proportion of the total scan. One scout scan contributes an effective dose of 0.6 μSv.

Thus, the total effective dose for a CSD measurement is 6.9 ± 0.6 μSv.

This compares with 0.6 μSv for a femoral neck examination on a DEXA [Hologic QDR 1000](Pye *et al*, 1990) and 60 μSv for a chest x-ray examination.

These values indicate that a density measurement imparts a relatively low dose when compared with other common radiographic techniques; the mean entrance skin dose for an AP projection chest x-ray is 0.3 mGy and for an AP projection pelvis examination is 6.6 mGy (NRPB Report R200, 1986).

4.5.3 Reduction of dose

Any reduction in absorbed dose to the patient would involve a smaller photon count which would lower the precision of the technique since the statistical error would increase.

A larger incident beam cross-sectional area would also reduce dose as a larger volume of tissue would be irradiated but this would degrade spatial resolution. The incident spectrum had been optimised to produce a large amount of single scatter from the critical volume as described in section 4.2, which indicated a high energy spectrum kV_p (120 kV_p). The optimal incident spectrum for a reduction in dose seems to be in the same energy range (figure 4.27).

The ideal way to reduce dose would be to collect the available photons more efficiently, which would lead to a reduction in exposure time for the patient. This would involve a design of collimator which would collect more photons around the azimuthal arc of the critical volume. The collimator hole size could also be increased but this would involve a loss of spatial resolution.

Chapter 5.

Results and evaluation of Compton Scatter Densitometry measurements.

5.0 Introduction

This chapter describes the results obtained from CSD measurements of phantoms and patients using the apparatus described in the previous chapter. This chapter also discusses and evaluates the results and assesses the suitability of CSD as a clinical bone densitometer. Comparisons are also drawn between CSD and other current bone densitometry modalities and their relative merits are discussed.

5.1 Phantom results

The following section presents the results of CSD bone density measurements of the solution-containing and bone-containing phantoms made on the CSD gantry as described in the last chapter.

5.1.0 Results from solution-containing phantoms

Results from the Monte Carlo simulations of CSD measurements (§4.4.1) indicated that a high incident beam kV_p was required to maximise detected single Compton scatter from the critical volume. CSD requires an accurate measurement of trabecular density over a range of densities with good precision. The phantoms measured contained density solutions or inserts of a known value (§4.3). An indication of the precision of the technique is to measure the variability of the data points when ρ^d, the statistic obtained from the gantry measurements, is plotted versus the known physical density of the solutions. The precision of the experimental measurements was assessed as the standard deviation of the repeated measurements expressed as a percentage of the mean (coefficient of variation, CV [Cullum *et al,* 1989; Haddaway *et al,* 1992]). The precision of the technique would be determined by the statistical error of the scatter count S_1 and S_2 and by errors introduced by repositioning errors of the critical volume. Best fit lines have been fitted to the data sets using a linear regression algorithm (Press *et al,* 1986).

5.1.1 Effect of incident kV_p on precision

This section experimentally assesses the effect of incident kV_p on the precision of CSD density measurements and compares the results with the theoretical predictions made by the Monte Carlo computer simulation of the CSD apparatus described in section 4.2.1.

5.1.1.0 X-ray generation

The x-ray tubes used on the gantry are diagnostic tungsten anode tubes [Dunlee, USA: Generator - Picker International D35 Mk.2] and are able to produce spectra up to 120 kV_p. A spectrum from the HPA Spectral Data Catalogue (Birch *et al,* 1979) filtered with 0.33 mm of copper is shown in figure 5.1. The spectra from the gantry x-ray tubes detected by the scintillation detectors A and B were measured and are shown in figure 5.2 for comparison.

---

[d] $\rho = (S_1.S_2 / T_1.T_2)^{1/2}$

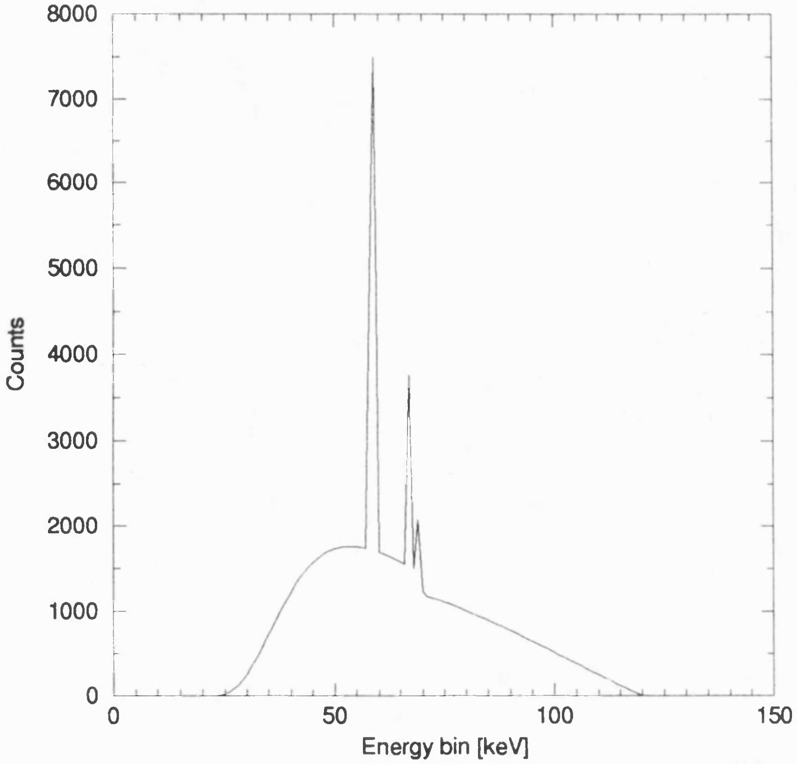

Figure 5.1 A 120 kV$_p$ x-ray tube spectrum filtered with 0.33 mm of copper taken from the HPA Spectral Catalogue.

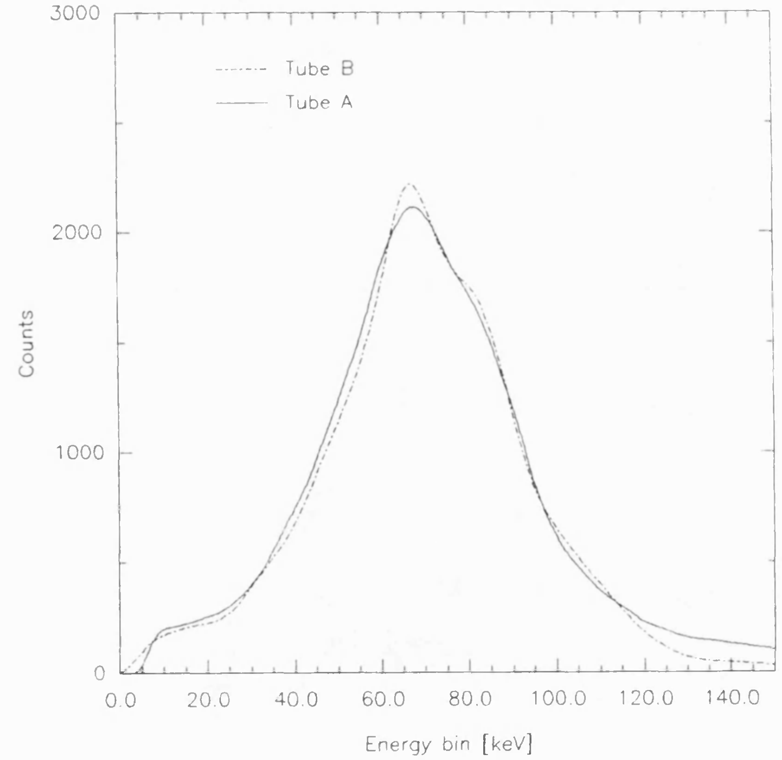

Figure 5.2 Gantry x-ray tube spectra measured by gantry scintillation detectors.

5.1.1.1 Experimental assessment of precision

Experimental measurements of ρ[e], obtained from the phantoms described in §4.3, over a range of incident beam kV_p values were made from 80 to 120 kV_p. These measurements were taken in order to confirm the predictions made by the Monte Carlo computer simulations (§4.2.1) which forecasted an increase in single scatter and an increase in single scatter relative to multiple scatter as kV_p increased. Although specific scatter proportions would not be available from experimental data, the general predictions of the Monte Carlo model would be confirmed by an increase in measurement precision with kV_p. The phantom employed was the circular (size 1) phantom, described in chapter 4, containing a 1.17 gcm^{-3} density solution chosen as a mid-range density value. The exposure time was 30 s and the mA set at 2.0. This exposure time was chosen as being significantly longer than the 10 s exposure time quoted by Koligliatis (1990) in order to ensure good counting statistics.

The graph in figure 5.3 shows some examples of the results obtained from the circular phantom for different incident kV_p values, and table 5.1 shows the corresponding CV values.

Incident kV_p value	CV value (%)	gradient value of best fit line
80	2.0	0.015 ± 0.003
100	1.7	0.021 ± 0.003
110	1.4	0.036 ± 0.003
120	1.0	0.041 ± 0.003

Table 5.1 Table showing CV values for circular phantom (size 1) measured over a range of incident kV_p values.

---

[e] $\rho = (S_1.S_2 / T_1.T_2)^{1/2}$

These results indicate that the 120 kV_p incident spectrum has the lowest CV and hence provides a measurement with the best precision. The CV values tend to decrease as incident kV_p increases. This is in agreement with the computer model which predicted a higher single scatter count relative to the multiple scatter count at the scatter detector. Although this is not possible to establish experimentally the data collected from the gantry indicates an increase in the total scatter count at the scatter detector, which is in agreement with the computer model. This is also in agreement with the findings of Battista and Bronskill (1978) who calculated scatter fluences inside phantoms using monoenergetic beams over a wide range of energies.

In figures 5.3 to 5.8 the values of k have been arbitrarily selected in order to display the data clearly.

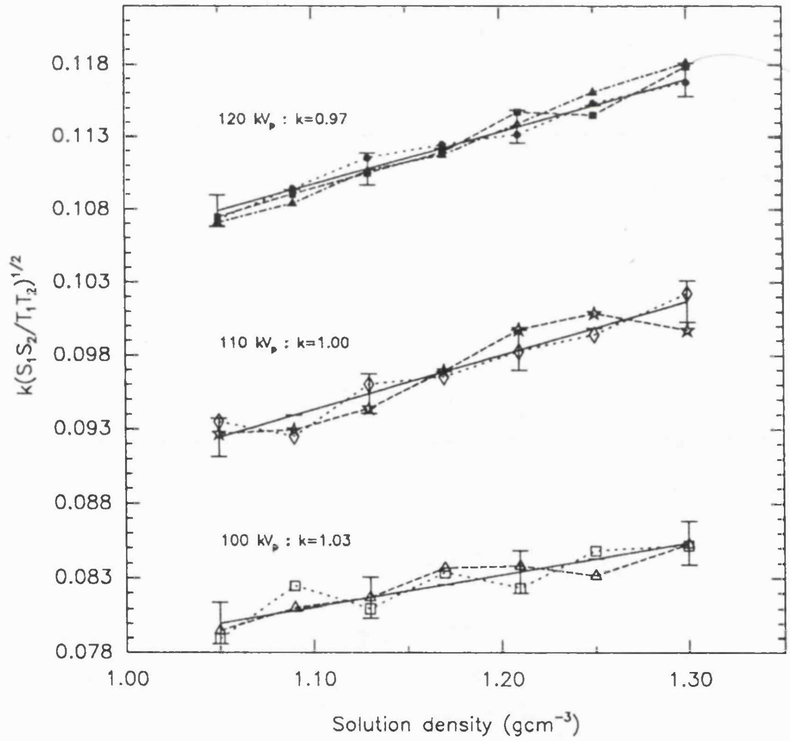

what ?

Slopes similar.

(?)

Figure 5.3 Examples of results of CSD measurements on the circular phantom (size 1) showing variation of rho with incident kV_p

An increase in kV_p also reveals a slight increase in the line gradient, which will allow more sensitive discrimination of small changes in density. As kV_p increases the production of single scatter from the critical volume becomes more probable which produces higher values of rho which accounts for the gradient increase.

5.1.2 Effect of exposure time on precision

Exposure time had to be chosen in order to give the best precision for the least exposure time, which meant a compromise was necessary between the best precision and the lowest dose. This would be an approximate precision of 1% with the shortest exposure time. This precision is the ideal required for detection of abnormal bone loss rates over longitudinal bone density studies (§1.4). Measurements to determine the best exposure time were carried out on a large phantom which represented an average thickness measurement site (size 3 circular phantom). A large phantom was selected as this would produce the worst case precision as the counting statistics would be poor. Measurements were made at 10, 20, 30 and 50 seconds, repeated at least three times and the CV assessed in each case. An example of the data collected is shown in figure 5.4.

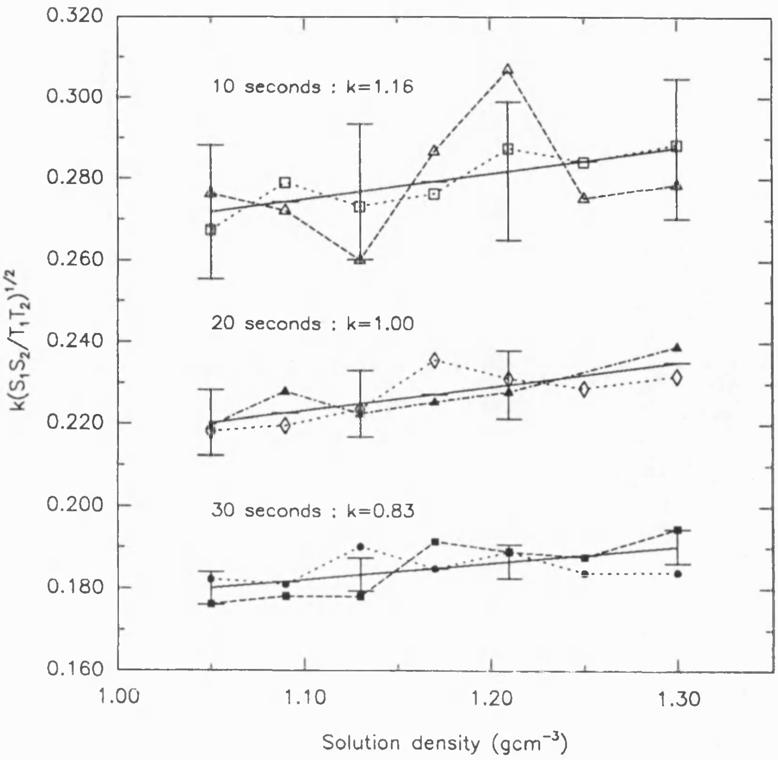

Figure 5.4 Examples of CSD results showing variation of rho with exposure time measured on the circular size 3 phantom.

OK ✓

notation

These results indicated that short exposure times (10 or 20 s) produce results with poor precision. At 30 s the precision is approaching 1%, and the precision appeared to only slowly improve as exposure time was increased. The small improvement in precision was not considered worth the extra dose imparted to the patient. Also, the patient would have to remain motionless for twice the length of time, increasing the probability of movement errors.

5.1.3 Effect of phantom size on precision

Once the optimum incident kV_p and exposure time had been assessed, a series of CSD measurements were made on different size phantoms to see the effect of measurement site size change on precision. Precision was expected to improve as the measurement site decreased in size as the scatter count statistics would also improve. Measurements were made on all the circular solution-containing phantom sizes with an incident beam of 120 kV_p for an exposure time of 30 s. The results are shown in figure 5.5 and the corresponding CV values in table 5.2.

Circular phantom size	CV value (%)	gradient value of best fit line
1	1.1	0.078 ± 0.003
2	1.5	0.072 ± 0.003
3	1.8	0.073 ± 0.003

Table 5.2 Table showing CV and gradient values for measurements taken on the circular solution-containing phantom.

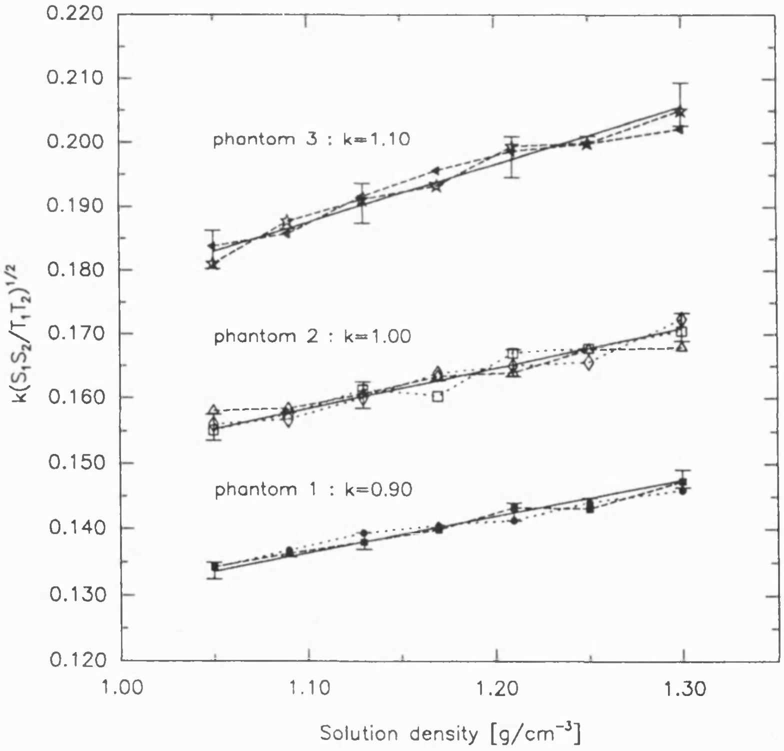

Figure 5.5 Examples of CSD results showing the variation of rho with circular phantom size.

These results show the measurement precision on the large phantoms to be lower than the measurements on the small phantoms, as expected, due to the poorer counting statistics obtained from the larger phantom. Although phantom size is an important factor when assessing the precision, phantom size changes produced no significant change in the gradient of the best fit line. This is predicted by CSD theory using dual x-ray beams and is essential if comparative serial density measurements are to be made using CSD.

Results from the femoral neck phantom are shown in figure 5.6 which shows measurements with a CV of ~1% and a gradient of 0.074 ± 0.003 which is the same as the circular phantom gradients within experimental error limits. The precision of the femoral neck measurements are significantly better than the comparable size 3 circular phantom. This was attributable to the large diameter of the trabecular substitute inserts in the femoral neck phantom which would eliminate any repositioning error. The circular phantom density solution inserts have a diameter of 18 mm which is only slightly longer than the long dimension of the critical volume in the y-axis plane (figure 5.7). A slight repositioning error would produce unwanted signals from the cortical bone substitute surrounding the density solution insert.

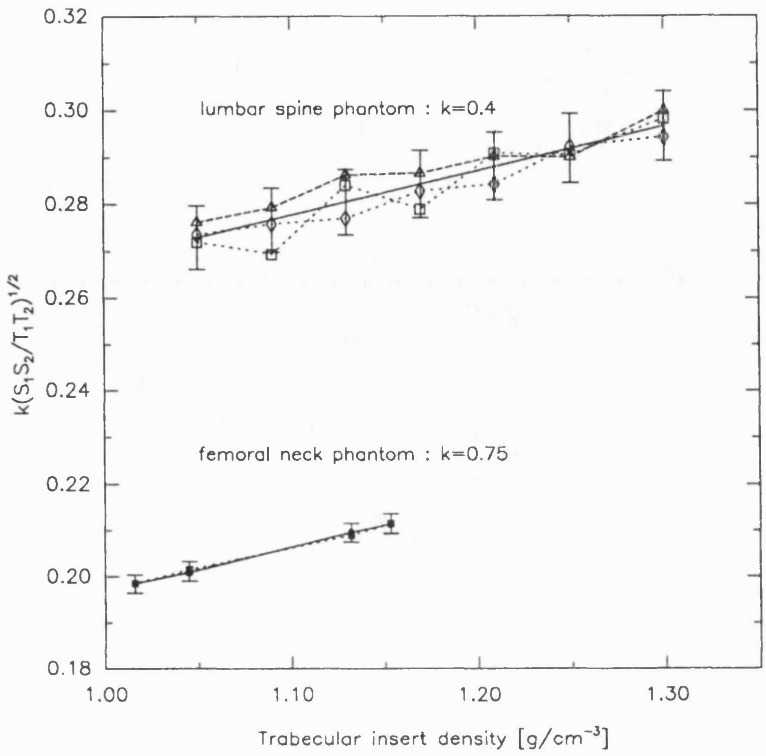

Figure 5.6 Examples of CSD results showing variation of rho with density solution inserts for lumbar spine and femoral neck phantom.

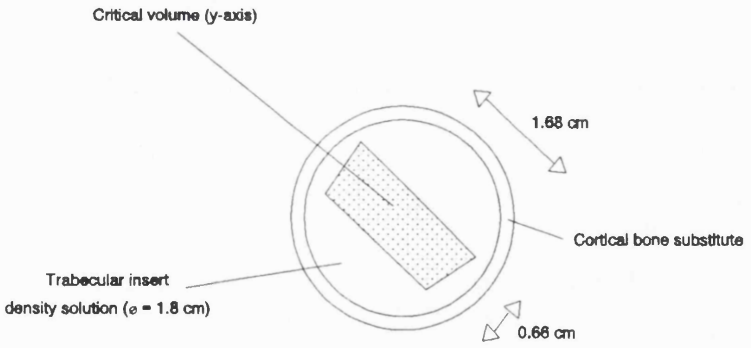

Figure 5.7 Diagram illustrating relation of critical volume dimension (y-axis cross-section) with dimension of trabecular insert density solution.

The graph in figure 5.6 also shows results collected from the lumbar spine phantom producing a CV of 2.5%. This is higher than all the other phantoms and is attributable to the large size of the phantom reducing the scattered photon counts and the statistical precision. These figures also show that phantom size changes and also phantom geometry changes produced no significant change to the gradient values of the best fit lines. As stated previously, this is predicted by CSD theory and is necessary for longitudinal studies of bone density. All the graphs in figures 5.3 to 5.8 show data sets with arbitrary calibration constants (*k*), selected to display the data more clearly. Section 5.1.5 will study the value of the calibration constants calculated from the phantom data using the density solutions as calibration standards (Hanson *et al*, 1984), and the application of the *mcf* values.

5.1.4 Precision of CSD technique for biological samples.

Measurements on the solution-containing phantoms used to assess precision were limited since they measured a homogeneous trabecular bone substitute. Trabecular bone is an inhomogeneous substance which can change in composition over short distances (Leichter *et al*, 1985). In order to assess the effects of repositioning and critical volume size on precision, real bone samples or a realistic trabecular phantom must be used as a measurement site. In this case several repeat measurements, with the same exposure conditions used for the previous phantom measurements (120 kV_p beam; 30 s exposure; 2 mA), were made on the bone-containing phantoms described in the last chapter (§4.3.1). Some examples of the results are shown in figure 5.8. The CV of these measurements was found to be 1.6% which compared favourably with the similar size 3 circular phantom (CV=1.8%).

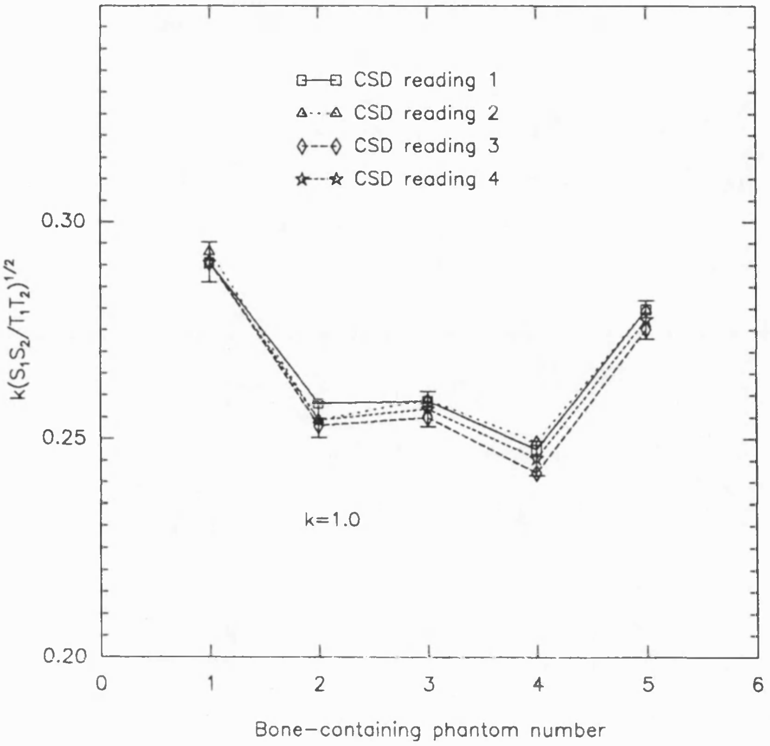

Figure 5.8 Graph showing consecutive CSD measurements on same phantom used to assess the precision of the technique.

This result indicated that the precision for the bone samples was the same as the phantom results within experimental error limits. This would seem to confirm that the critical volume was the correct size for averaging over a volume of trabecular bone and also that the repositioning errors for the bone-containing phantoms were minimal. The averaging effect of CSD can be illustrated by comparing the structural dimensions of trabecular bone with the size of the trabecular volume. A CT image (figure 5.9) shows the structure formed by the trabeculae and the marrow filling the spaces between the bone fibres. An ROI corresponding to the dimensions of the critical volume section was defined within the CT image. The CSD critical volume dimensions can be seen to encompass a large number of fibres and marrow spaces producing an average value of the density within the volume.

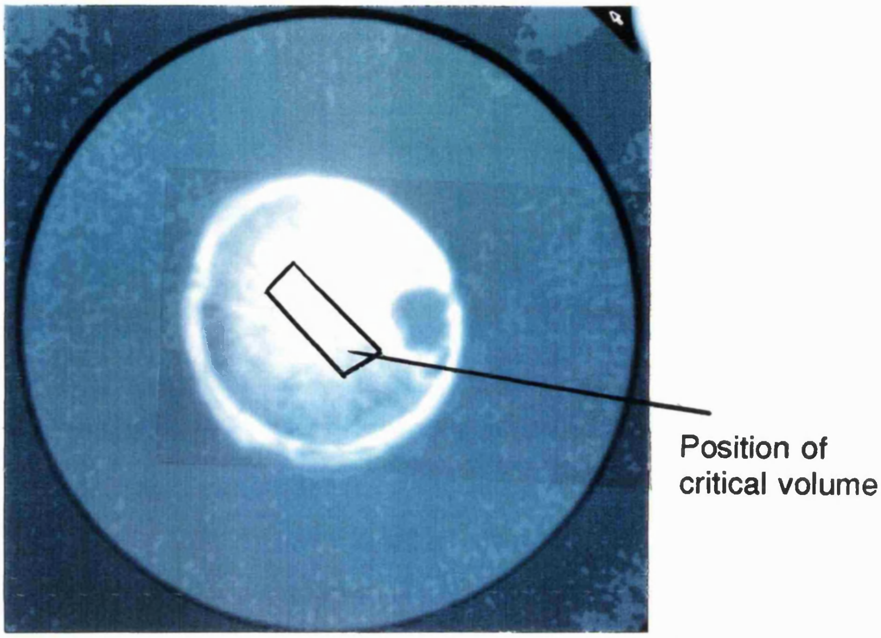

Figure 5.9 CT image of bone slice showing relationship with critical volume dimension (y-axis section).

5.1.5 Value of *k* and application of *mcf* values

From equation 2.4 it can be seen that an absolute density value requires the calculation of a calibration constant *k* and the application of a multiple scatter correction factor (*mcf*). The *mcf* values have been previously calculated by Monte Carlo computer simulation of the CSD apparatus for all the phantoms used in these studies and are presented in section 4.4.2. All the solution-containing phantoms contain trabecular insert density solutions of known density. By rewriting equation 4.3 to produce an expression for determining *k* (equation 5.1), the values of *k* can then be calculated with respect to phantom size.

$$k = \frac{\rho}{\left(\frac{S_1.S_2}{T_1.T_2}\right)^{\frac{1}{2}} . mcf} \qquad 5.1$$

In order to use the calibration constant *k* to provide an absolute value of bone density, the value of *k* was calculated from the known density values of the trabecular inserts for the phantoms described previously. These *k* values were then plotted versus the beam path length of the transmitted beam. This path length is an easily obtainable characteristic parameter from the measurement site. These values of *k* also include the calculated *mcf* values (§4.4) as part of the calibration constant (equation 5.1) applied to the terms S_1/T_1 and S_2/T_2. The values of *k* are shown plotted in figure 5.10. Interpolated values of *k* can be selected for use in the determination of unknown density values when the dimensions of the measurement site are known. This would only be valid if the x-ray source kV_p, mA value and SCA energy windows settings remain the same as those during the phantom measurements.

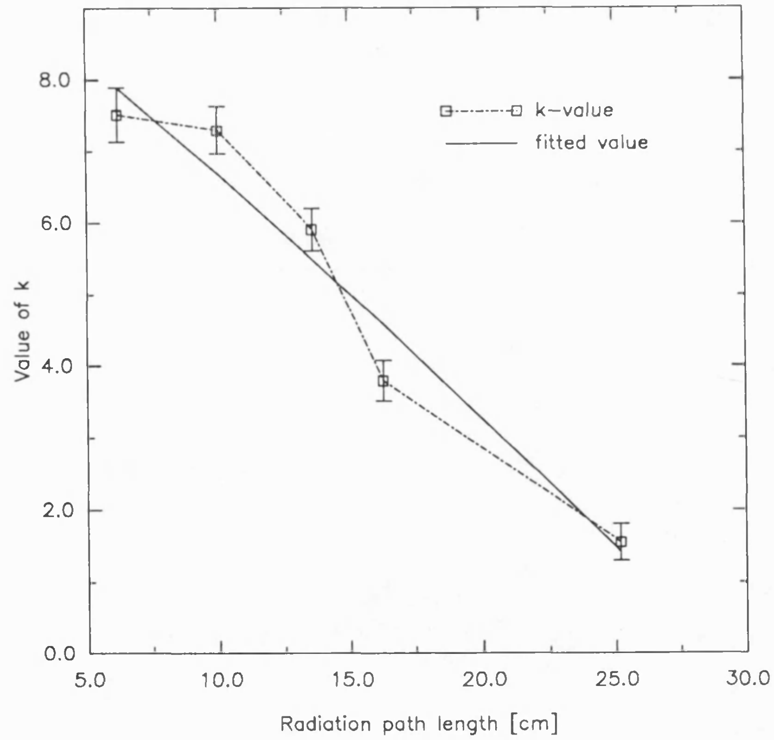

Figure 5.10 Graph showing variation of calibration constant *k* with radiation path length through measurement phantoms.

5.1.6 Results from bone-containing phantoms

Applying the calibration constant *k* for the diameter of the bone-containing phantom produces absolute density values for the bone samples in the phantom. These values are shown in table 5.3 and figure 5.11 and can be used to compare with density evaluations of the same phantoms using other bone density measurement modalities.

Phantom	**1**	**2**	**3**	**4**	**5**
CSD density value [gcm^{-3}]	1.21 ± 0.02	1.06 ± 0.02	1.07 ± 0.02	1.02 ± 0.02	1.16 ± 0.02

Table 5.3 Table showing CSD density values for the bone-containing phantoms.

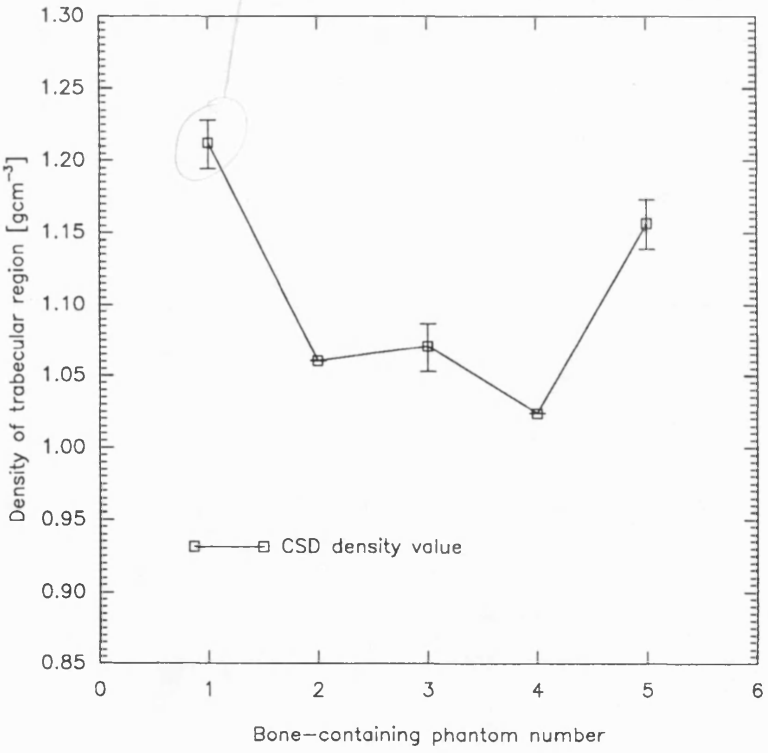

Figure 5.11 Graph showing CSD bone density measurements made on the bone-containing phantoms.

5.2 Comparison with other modalities

In order to assess the effectiveness of CSD for use as a clinical technique it is necessary to compare CSD density data obtained from test phantoms and patients, with data collected from clinically established techniques. One of the most applicable techniques is with QCT measurements, as both QCT and CSD measure the density of the central trabecular region of the bone. A comparison is also made with DEXA data which is rapidly becoming the clinical standard for bone mineral assessment (§1.5.5.3). However, this technique provides density data on the whole bone as it is based on an integral measurement.

In this thesis the bone density and BMC measured by these techniques are compared statistically. The most widely used measure of association between sets of variables is the linear correlation coefficient (*r*) which provides a quantitative measure of the correlation. If there is no correlation between the variables the value of *r* will be close to zero; when there is a strong correlation between the variables *r* will take a value near to ± 1. The measure of scatter around the regression line of the two variables is known as the standard error of estimate (*see*) and is similar in properties to the standard deviation. The *p* value quoted in the regression graphs is the significance level at which the null hypothesis of zero correlation is disproved when using Students' t-distribution i.e. a small value will indicate a significant correlation.

5.2.0 Quantitative Computed Tomography bone density measurements

A properly calibrated CT machine can measure attenuation coefficients with a reproducibility greater than 0.15% and with an absolute accuracy of 1% (Cann *et al*, 1985). A CT system is calibrated on an absolute scale referenced to air and water, and for biological materials the x-ray attenuation coefficient is linear with respect to tissue density. QCT can therefore be used to accurately measure the bone mineral content absolutely in the presence of a known soft-tissue component e.g. bone mineral mixed with marrow. If the soft tissue has a variable attenuation due to the presence of fat in the marrow then a dual energy technique can be employed. However, several investigators have found little or no loss of accuracy when using single energy QCT instead of dual energy QCT and report a strong correlation between results obtained from single energy and dual energy QCT (Cann *et al,* 1985; Reinbold *et al,* 1986; Eriksson *et al,* 1988).

CT images are collected and reconstructed to form slice images of the measurement site. One of the advantages of this technique is the ability to select the central trabecular region of the bone and determine the mean CT number of the region. This ability to examine the trabecular region only is also exhibited by the CSD technique. With the inclusion of mineral equivalent calibration materials in the image, a value for the bone density can then be determined.

5.2.0.0 Acquisition of QCT data

The CT scanner used in this study was a Philips Tomoscan 350 situated at University College Hospital. Exposure factors were; 120 kV_p spectrum filtered with 0.5 mm of copper set at 200 mAs. A slice thickness of ~0.5 cm was used to scan the central regions of the solution-containing phantoms. This is similar to protocols reported by many researchers (for example, Cann *et al,* 1986; Banks and Stevenson, 1986). The bone containing phantoms were scanned with a slice thickness of 0.15 cm spaced at 0.30 cm. The narrow slices and thin spacing were used because of the short length of bone available in the phantom. These slices would ideally be contiguous but there were time constraints on the use of the scanner. Each phantom had four K_2HPO_4 solutions (1.05, 1.13, 1.21, 1.30 gcm^{-3}) attached to the surface to provide bone mineral equivalent reference density values.

To allow comparison with CSD data the single slice measurements on the femoral neck, lumbar spine and circular phantoms were collected through the mid-plane of the phantoms. Each of the bone-containing phantoms had seven slices collected around the mid-plane of the phantom.

Images were collected and transferred to the departmental SUN workstations for analysis. Analysis of the circular, femoral neck and lumbar spine phantoms was carried out as follows: regions of interest (ROIs) were defined in the centre of the reference solutions and the mean CT numbers recorded for each image. These CT numbers were then plotted versus reference solution density to confirm the linearity of response. The error bars are the standard deviations of areas of uniform tissue in the phantoms. An example of this plot is shown in figure 5.12. An ROI was defined at the centre of the trabecular bone inserts and the mean CT number recorded for each image. Partial volume effects were avoided by defining the ROI well within the tissue boundaries. This was checked by moving the ROI small distances towards the boundaries in different directions and observing any significant change in the mean CT number. Interpolation was used to calculate the equivalent K_2HPO_4 mineral density of the trabecular bone ROI from the reference solution graph for each phantom.

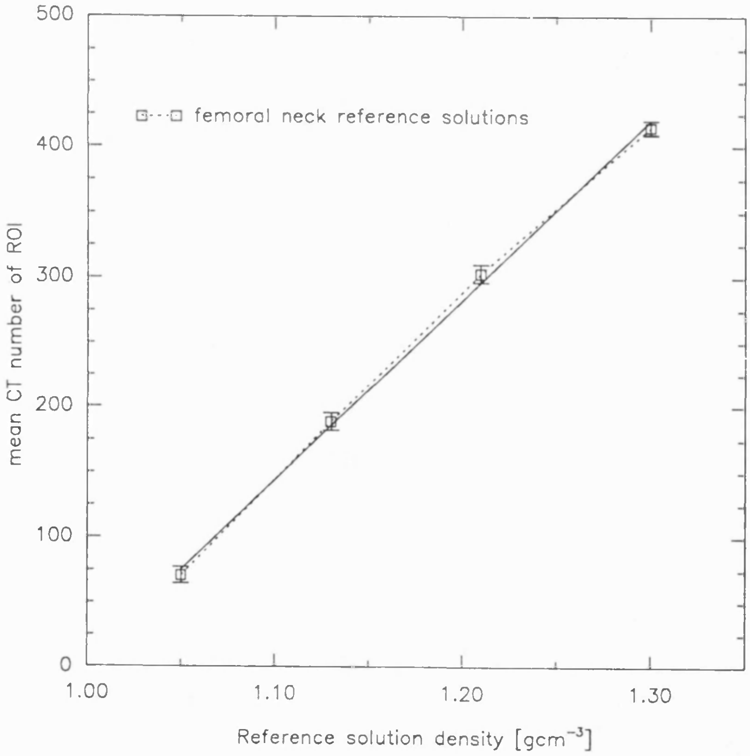

Figure 5.12 Graph showing linear response of mean CT number from reference solution ROI with density of reference solutions.

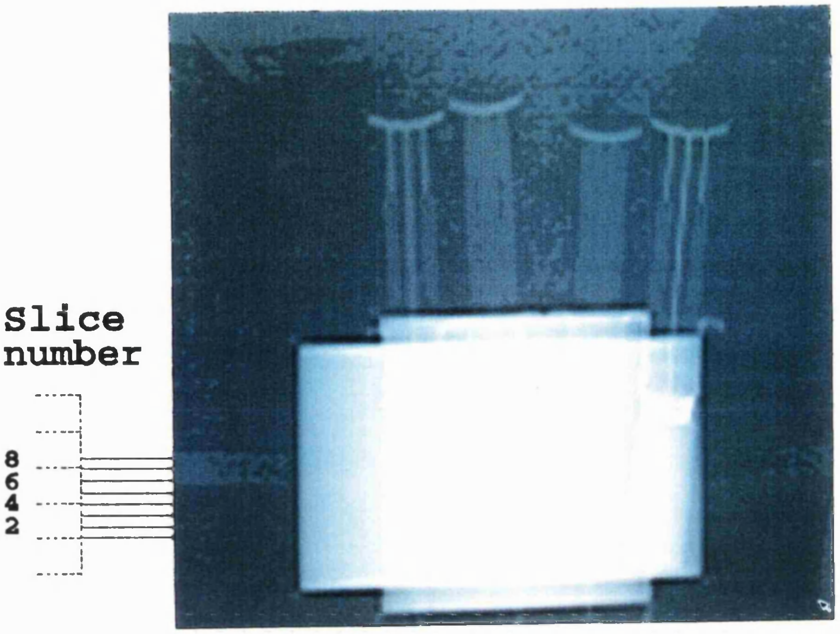

Figure 5.13 Scanogram of bone-containing phantom acquired from the CT scanner showing the positions of the scanned slices.

For each of the bone-containing phantoms a 'scanogram' was performed which formed a projection image of the phantoms (figure 5.13). This allowed the position of the bone within the phantom to be clearly seen. Each slice was also marked on the scanogram indicating which part of the bone was under examination.

For the bone-containing phantoms the treatment of the reference solutions followed the same procedure with an additional check that the mean CT numbers of the regions did not differ between the slices of the same phantom. For examination of the bone regions a quadrilateral ROI with the same dimensions as a central cross-section of the CSD critical volume was used. This was placed at the centre of the phantom, in the phantom mid-plane slice in order to simulate a CSD measurement, as shown in figure 5.14. Although part of the critical volume overlapped into the neighbouring CT slices, the contribution was small and was excluded from the analysis. As CSD produces an average response over the whole critical volume, the mean CT number from this ROI was calculated and the mineral equivalent value found by interpolation from the reference solution graph. This technique was not necessary for the solution-containing phantoms since they contain homogeneous trabecular substitutes.

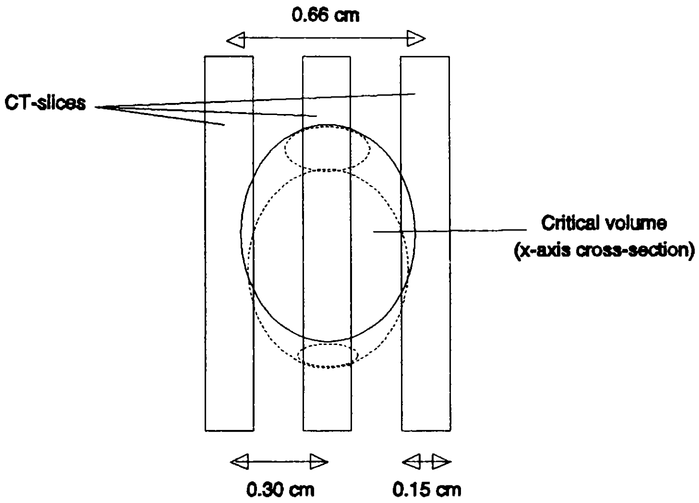

Figure 5.14 Schematic diagram showing relationship of CT slices through bone phantom with CSD critical volume dimensions.

Trabecular bone is a very inhomogeneous material which can vary in density over short distances due to the rapidly changing architecture of the bone fibres. In previous QCT studies (e.g. Sartoris *et al*, 1986), the mean CT number may vary by up to 100% between the same ROI in thin contiguous slices. This effect seems marked in the femoral neck region. To reduce the effect of this short-term variation the largest possible ROI and largest number of slices should be combined to produce a mean CT number over a large volume of trabecular bone. This was implemented on the bone samples to investigate how representative a smaller critical volume ROI assessment of the trabecular bone density would be compared to the density found by averaging the CT number over a large volume of trabecular bone. Therefore, an irregular ROI was defined a short distance within the cortical casing of the bone, to avoid partial volume effects, and the mean CT number recorded. This was achieved by zooming the image and altering the grey-scale values until the cortical bone components of the image were highlighted. The same grey-scale values were used for each slice and the ROI process was repeated for each slice of the bone phantoms. The mineral equivalent was found from the expression -

$$ME = \frac{\sum_{k=1}^{n} (M_n A_n)}{\sum_{k=1}^{n} (A_n)} \qquad 5.2$$

where

ME mineral equivalent of trabecular bone volume [gcm^{-3} of K_2HPO_4]
M_n mean mineral equivalent density of defined ROI in slice n
A_n area of ROI in slice n

5.2.0.1 Results from QCT measurements

Figure 5.12 showed the expected linear response of the mean CT number from circular regions of interest in the mineral equivalent calibration solutions attached to the femoral neck phantom plotted against the density values. These values were used to assess the mineral equivalent density of the trabecular bone substitute inserts within the phantom. Table 5.4 shows these values compared with the known density values of the trabecular inserts from the femoral neck phantom. The CT values were slightly lower than expected. The reduction in density value can be attributed to beam hardening effects. Ruegsegger *et al* (1981) suggest that calibration, as described above, is a simple and effective way of correcting for this effect. In this case a correction factor of 0.951 was used. This factor should be applied to other measurements acquired in the central region of similar size phantoms. Although the CT density values were approximately 5% lower than the known insert densities, the correlation between the two sets of values was very high and is shown in figure 5.15.

Phantom	**Femoral neck phantom**			
Known insert [gcm^{-3}]	1.085	1.119	1.176	1.188
CT measured density [gcm^{-3}]	1.02 ± 0.01	1.05 ± 0.01	1.13 ± 0.01	1.15 ± 0.01

Phantom	**Bone-containing phantom [whole bone ROI]**				
Bone insert	1	2	3	4	5
CT measured density [gcm^{-3}]	1.23 ± 0.01	1.15 ± 0.01	1.17 ± 0.01	1.18 ± 0.01	1.24 ± 0.01

Phantom	**Bone-containing phantom [critical volume ROI]**				
Bone insert	1	2	3	4	5
CT measured density [gcm^{-3}]	1.31 ± 0.01	1.20 ± 0.01	1.23 ± 0.01	1.23 ± 0.01	1.31 ± 0.01

Table 5.4 Table showing bone density values of two measurement phantoms measured by CT.

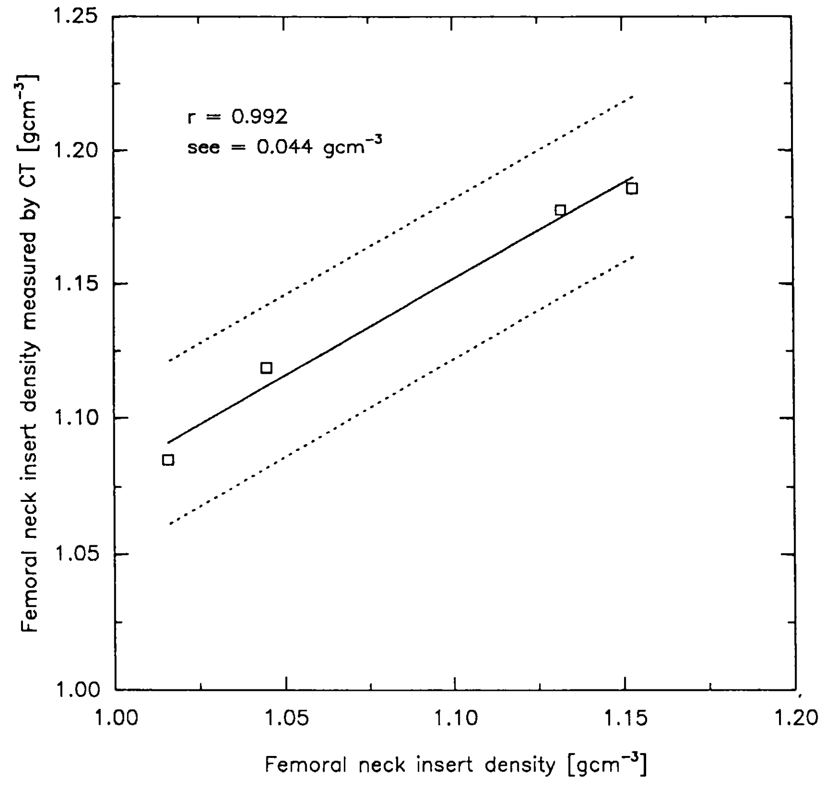

Figure 5.15 Graph showing correlation between femoral neck bone density inserts and CT measurements ($p<0.001$).

Table 5.4 also shows the CT density results obtained from the bone-containing phantoms assessed from the critical volume ROIs and the whole bone ROIs which are plotted in figure 5.16. Mineral equivalent values were calculated from the calibration solutions attached to the phantoms in the same manner as the femoral neck phantom. The beam hardening correction, described at the beginning of this section, was also applied as the dimensions of the phantoms were similar. The density values ascertained by the whole bone ROIs were approximately 6% lower than the densities calculated from the critical volume ROIs. This was probably due to the structure of the femoral head; the trabecular fibres become more tightly clustered and gradually become solid cortical bone towards the top of the femoral head. The critical volume ROI was centrally positioned inside the bone and represented an average volume. The whole bone ROI had several large-area slices beneath the critical volume ROI which contained lower density trabecular bone, which over-compensated for the smaller areas of high density trabecular bone above the critical volume ROI, which was towards the top of the femoral head. This was also shown by examining the density of the ROIs within individual CT slices. The density values decreased as the site of the slices progressed away from the top of the femoral head, down towards the shaft. Although the absolute values of density differed between the two ROIs, the correlation between the two sets of density data was good (r=0.992) and is shown in figure 5.17. Both these ROIs were similar to those described by Steiger *et al* (1990), for lumbar spine measurements, who found a good correlation between both sets of density data (r=0.985) and proposed them as suitable ROIs for clinical application. Also described was a third ROI which encompassed all the bone within the slice except for the transverse processes, but this was not considered successful because of the preferential bone loss in the trabecular region.

The density values from the QCT measurements of bone density in the bone-containing phantoms and from the CSD measurements were found to correlate well. This was expected since both techniques assess the density of the trabecular region. The correlation of the density data between the critical volume ROI QCT measurements and CSD data (r=0.90) was found to be better than between the whole bone ROI QCT measurements and CSD data (r=0.84). These data sets are shown in figures 5.18 and 5.19. The good correlation between the CT density measurements and the CSD values was also expected since there was a close match between the CSD critical volume section and the CT volume under examination in the image (§5.3.0.0). However, the absolute density values obtained from the CSD density measurements were lower than the critical volume ROI CT values by approximately 7%. This variation may be accounted for by several reasons: there may be a positioning error of the critical volume ROI within the bone images which does not register well with the position of the CSD critical volume. This may be due to a rotation of the images with respect to the angle of the critical volume or an error in the positioning of the bone during the construction of the phantoms. As a result, the whole bone ROI values appeared closer to the CSD values since they represented an average through the volume of the trabecular bone. Also, the rapid change of bone architecture may have meant that the non-contiguous slices used for the CT assessment may have produced a less representative value than contiguous slices, which would also be due to the non-homogeneity of the trabecular bone. A larger sample of measurements on phantoms is required in order to assess any trends due to these effects.

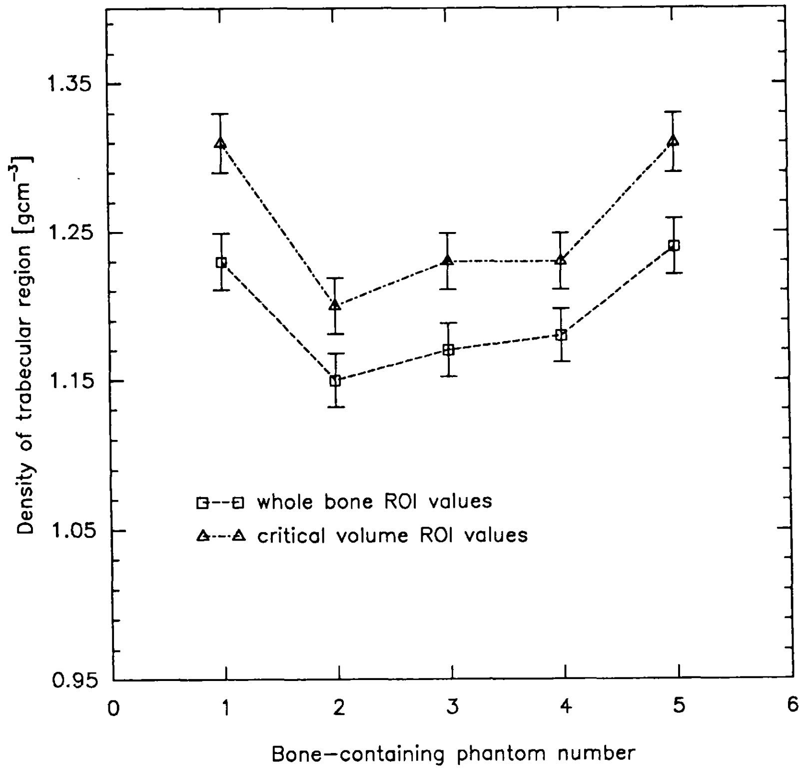

Figure 5.16 Graph showing density values of bone-containing phantom inserts measured by CT.

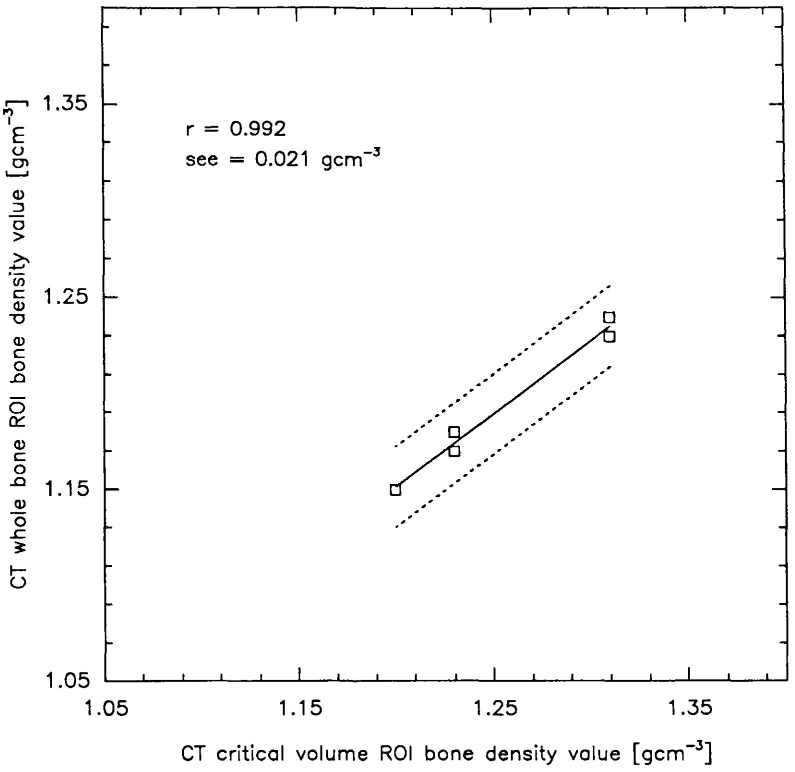

Figure 5.17 Graph showing correlation of bone-containing phantom measurements made by critical volume ROI CT and whole bone ROI CT ($p<0.001$).

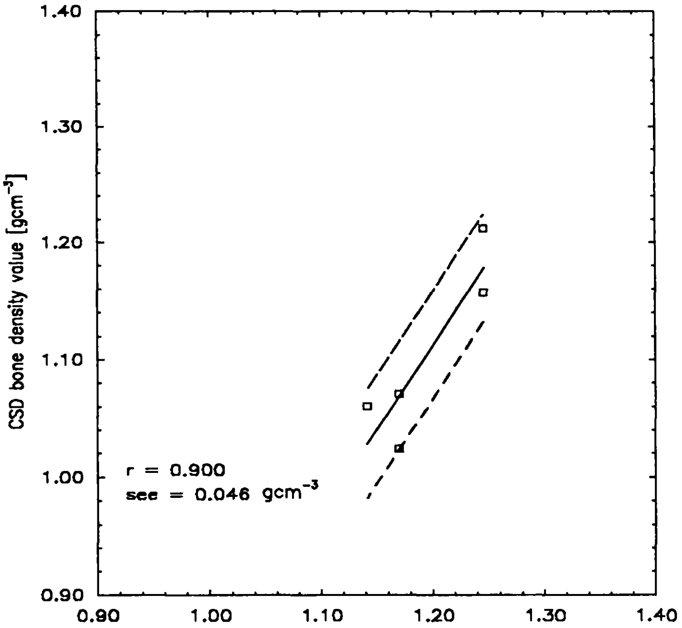

Figure 5.18 Graph showing correlation of bone-containing phantom measurements made by critical volume ROI CT and CSD ($p<0.05$).

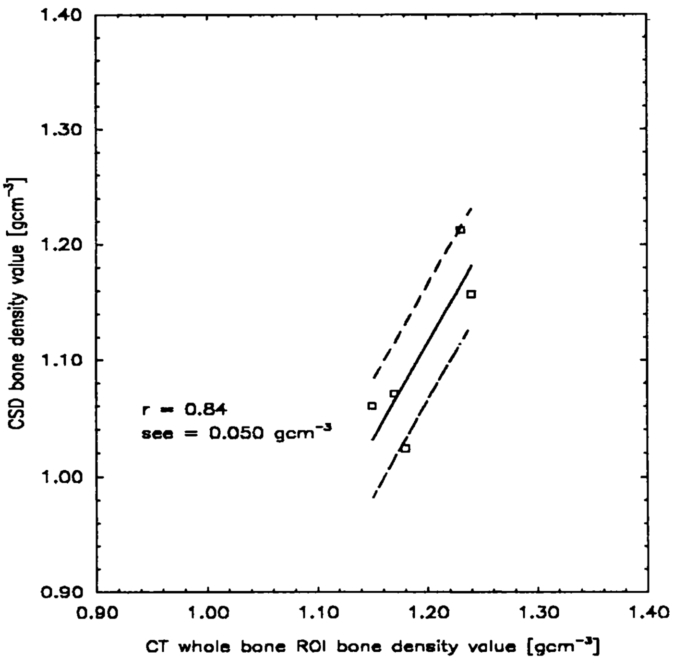

Figure 5.19 Graph showing correlation of bone-containing phantom measurements made by CT using whole bone ROI and CSD (p=0.07).

5.2.1 DEXA bone mineral measurements

DEXA is the latest development in the field of photon absorptiometry (PA) bone density measurement and is rapidly becoming the clinical standard. The apparatus used for this study was a Hologic QDR 1000/W machine based in the Institute of Nuclear Medicine at the Middlesex Hospital. This machine scans an x-ray beam across a pre-determined measurement area. Each point on the scan is individually calibrated with a rotating reference disc which places a known sample of bone and soft tissue equivalent material into the beam path. A more detailed description of the QDR principles and technique is provided by Cullum *et al* (1989) and a general overview of DEXA is described in section 1.5.5.3.

5.2.1.0 Acquisition of DEXA data

Measurements were made on the bone-containing and solution-containing phantoms previously described. Phantoms containing density solutions were scanned with the same set of solutions used in the CT data acquisition (§ 5.2.0.0) inserted. The pre-defined measurement area was set as the projectional cross-sectional area of the phantom which made the maximum soft-tissue area available for the DEXA soft-tissue background calculation. For the circular phantom this was set as the whole phantom cross-sectional area. For the femoral neck, lumbar spine and bone-containing phantoms this was set as a strip across the centre of the phantom spanning the entire width of the phantom. This allowed comparison with the CSD measurements which were made in the central region of the phantoms. Each scan was made in 'performance spine' mode which provided the best spatial resolution. The QDR uses a kV_p switched source (70/140 kV_p) at 2.0 mA with a source collimator of 0.3 mm diameter. Line spacing of the raster scan motion was 1.003 mm with a sample spacing of ~1.02 mm. Software installed on the scanner was Version 6.10. Some examples of the scans are shown in figures 5.20 and 5.21.

After the scan has been made the QDR calculates the area of the bone within the pre-defined area using an edge detection routine. The bone mineral content (BMC [g]) of the bone area is calculated using a dual energy analysis, as described in chapter 2, and is displayed along with the BMD (gcm^{-2}) which is the BMC divided by the bone area. The edge detection, area and BMD calculation routines were tested on the same phantom on several different occasions and produced the same results to within 1%.

However the following results from the DEXA measurements have not been corrected for the contribution of scatter into the detected beam. This effect is described in chapters 2 and 3 but has not been calculated for the QDR Hologic since the machine specifications were not available at the time that the calculations were made. Furthermore, application of the correction factors calculated for the Norland XR26 was not considered viable since the operating conditions of the x-ray source differed significantly (Norland XR26 operates at

100 kV_p; Hologic QDR operates with a switched 70/140 kV_p).

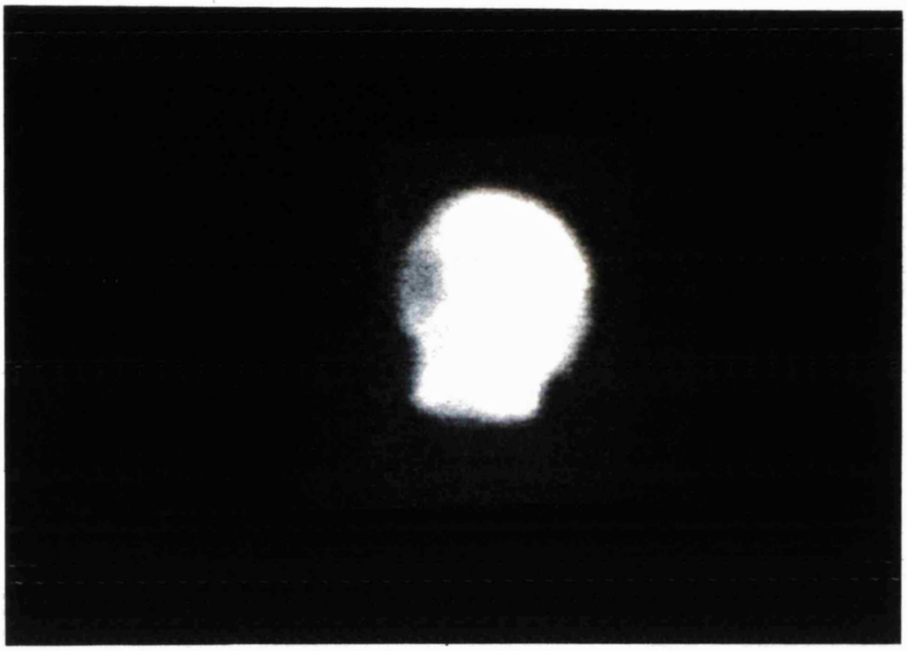

Figure 5.20 Example of QDR DEXA scan showing the image produced from an acquisition on a bone-containing phantom.

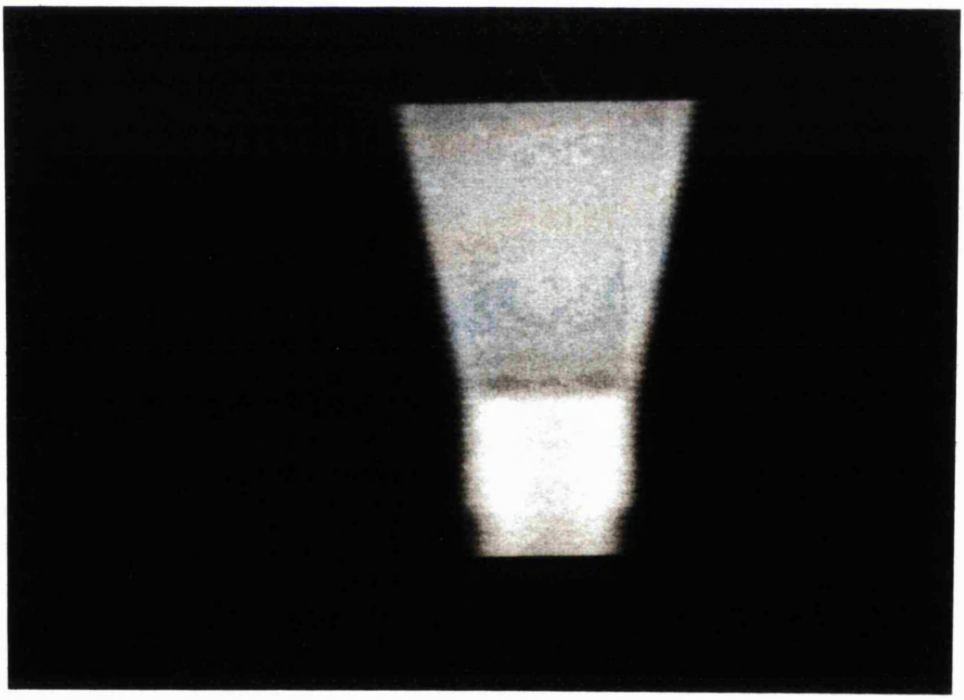

Figure 5.21 Example of QDR DEXA scan showing the image produced from an acquisition on the femoral neck phantom.

5.2.1.1 Results from DEXA measurements

Close examination of the scan images, in figures 5.20 and 5.21, reveal a 'feathering' effect at the tissue interfaces. This was due to the motion of the scanner moving the x-ray beam across a tissue boundary before the rotating calibration disc had finished calibrating at that point. However, this effect did not seem to hinder the edge detection routine and area calculation.

Anatomical details of the measurement phantoms could be clearly seen in the scan images, especially the bone details e.g. the spinal process in the lumbar spine phantom could be seen superimposed on the rest of the bone. The superimposition of the bone details is characteristic of a projection image or integration technique such as DEXA.

BMD values were calculated using the software supplied with the machine and are shown in table 5.5. The precision of the technique has been reported as being ~1% (Cullum *et al,* 1989) but is prone to certain systematic errors. Photon absorptiometry (PA) techniques require prior knowledge of the attenuation coefficients of soft tissue and bone in order to calculate the BMD of the scanned area. Consequently, BMD can differ between models since manufacturers provide their own protocols for the software BMD calculation. The software version is an important consideration when comparing data sets collected by PA instruments. There is also evidence of software being responsible for BMD variations especially for weak sources (DPA machines) and thick attenuators (Dunn *et al,* 1987; Shipp *et al,* 1988). This should not affect this study which is not longitudinal and uses an x-ray source on a medium thickness attenuator.

QDR measures the attenuation through the whole bone. An integration technique, such as DEXA, measures the radiation path length rather than the change in bone density. This is illustrated by examination of the femoral neck phantom scans (figure 5.21). There appears an apparent change in bone density along the bone, which is due to the cortical shell gradually thinning along the bone, even though the density of the cortical and trabecular bone substitute materials remains constant throughout the phantom.

Also the cortical processes on the lumbar spine vertebra are included in the calculation of the BMD which may mask a loss of density within the more metabolically active trabecular region.

Despite these sources of error, the correlation of the DEXA measured BMD values with the CSD density values for the bone-containing phantoms was very good (r=0.951) and is shown in figure 5.22. Similarly, the correlation of the BMD values with the QCT density values for the bone-containing phantoms was very good for both of the regions of interest used (r=0.976[f], 0.957[g]) which are shown plotted in figures 5.23 and 5.24. However, both the CSD and QCT techniques measure the density of the trabecular bone region which is a better indicator of bone loss.

Phantom	**Circular phantom**				**Femoral neck phantom**				
Known insert [gcm^{-3}]	1.05	1.13	1.21	1.30	1.085	1.119	1.176	1.188	
BMD [gcm^{-2}]	0.449 ± 0.005	0.548 ± 0.006	0.650 ± 0.007	0.745 ± 0.008	0.561 ± 0.006	0.581 ± 0.006	0.592 ± 0.006	0.599 ± 0.006	

Phantom	**Lumbar spine**				**Bone-containing phantom**				
Known insert [gcm^{-3}]	1.05	1.13	1.21	1.30	1	2	3	4	5
BMD [gcm^{-2}]	1.163 ± 0.016	1.196 ± 0.012	1.232 ± 0.012	1.268 ± 0.013	1.097 ± 0.011	0.913 ± 0.009	0.923 ± 0.009	0.915 ± 0.008	1.090 ± 0.009

Table 5.5 Showing values of BMD for the measurement phantoms obtained from the DEXA Hologic QDR 1000/W.

---

[f] critical volume ROI

[g] whole bone ROI

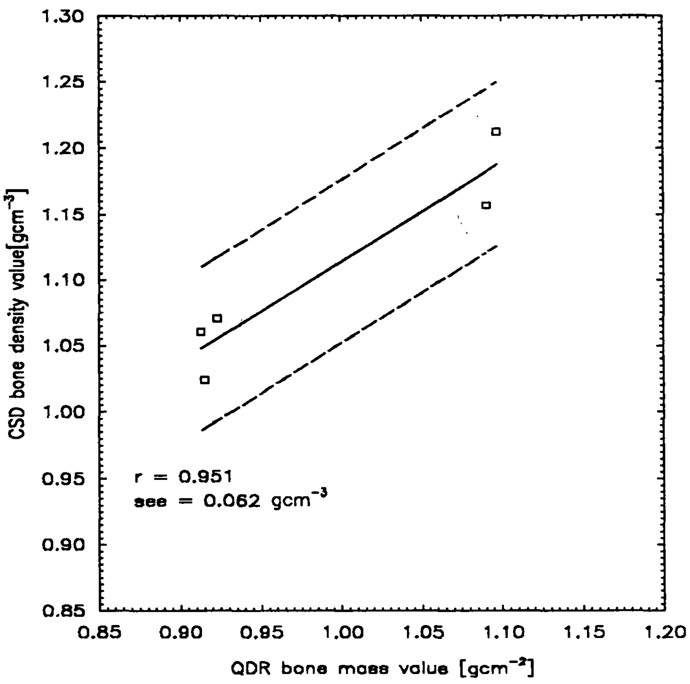

Figure 5.22 Graph showing correlation between bone-containing phantom measurements made by QDR and CSD ($p<0.01$).

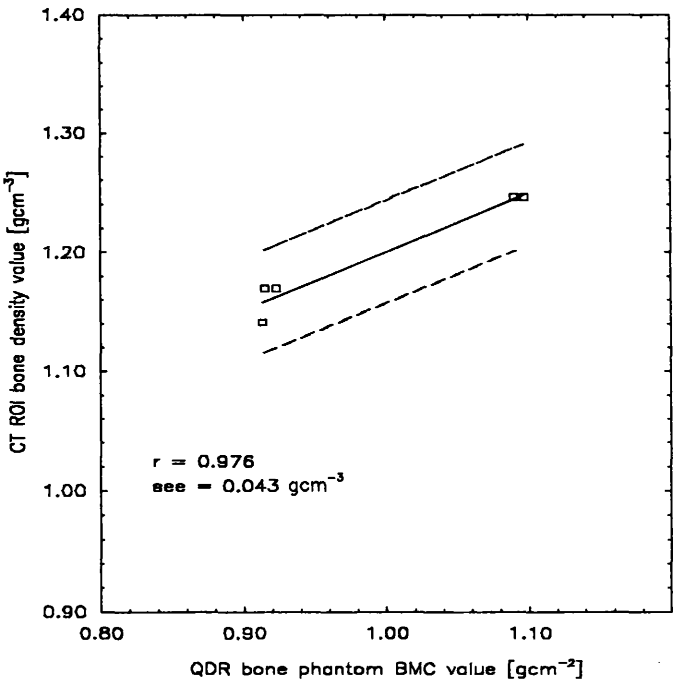

Figure 5.23 Graph showing correlation of bone-containing phantom measurements made by critical volume ROI CT and QDR ($p<0.005$).

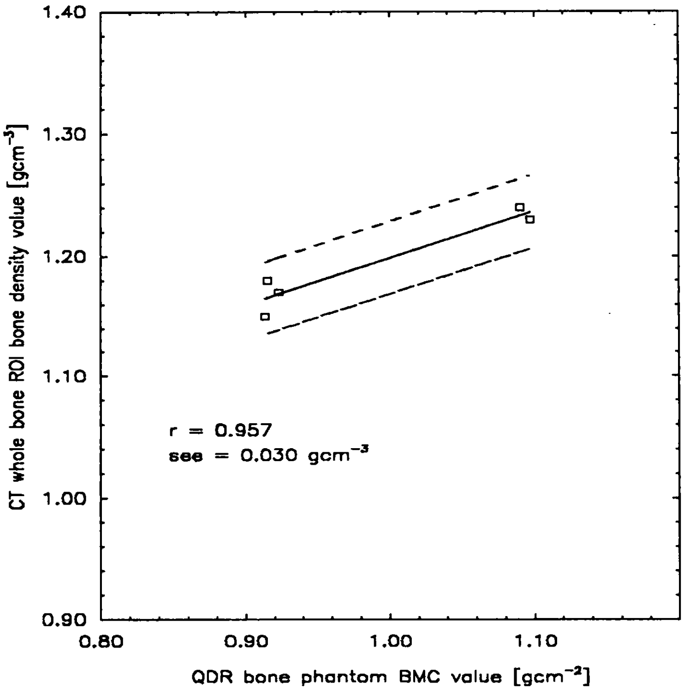

Figure 5.24 Graph showing correlation of bone-containing phantom measurements made by whole bone ROI CT and QDR ($p<0.01$).

5.3 Discussion of QCT, DEXA and CSD results

DEXA (and DPA) techniques are presumed not to correlate well with conventional QCT results since these PA techniques include denser bone from the cortical casing of the bones and from bone processes in the spine. Mazess *et al* (1991) state that the correlation between trabecular QCT and DPA as 0.8-0.9 over spinal studies which included a wide range of patient densities. This study, although limited in size has shown a correlation of >0.95, for phantom studies, which compares well. In osteoporotic patients Mazess *at al* (1991) also showed this correlation to be poorer as the range of variation is restricted and also preferential bone loss does occur within the vertebral body. No published comparisons are available for CSD density and DEXA BMD data, but the CSD data can be treated similarly to the CT analysis as they both examine the trabecular region. In this case the correlation between CSD density and DEXA BMD data from bone-containing phantoms was found to be very good (r=0.951) although very slightly lower than the CT and DEXA data r values.

Although QCT and CSD techniques examine the same bone region the correlation between the two techniques was poorer (r=0.90[h], 0.84[i]), although significant (p<0.05[h], 0.07[i]), than their respective correlations with the DEXA BMD values. The slightly poorer correlation may be due to errors in positioning the critical volume and the use of non-contiguous slices during the QCT data acquisition.

5.4 CSD measurements on a simulated patient

In order to assess the application of CSD for measurements on patients, a series of bone density measurements were performed on a simulated patient. This would allow a set of realistic density measurements to be obtained without subjecting patients to a radiation dose. The simulated patient consisted of a pelvis and femur bone submerged in a water bath. Both bones had been excised from cadavers, cleaned, preserved in formalin and allowed to dry in air. The water bath was used to simulate the surrounding soft tissue in the hip region of the body. The femur had a hole drilled through the trabeculae, down the length of the shaft, to accommodate the density solution inserts which had previously been used in the solution-containing phantom studies (§4.3.0). A diagram of the simulated patient showing a cross-section of the femur and the position of the pelvis is shown in figure 5.25. The water depth used was 13.1 cm which produced a radiation beam path length of 14.5 cm, which was comparable to the femoral neck phantom dimensions.

---

[h] critical volume ROI

[i] whole bone ROI

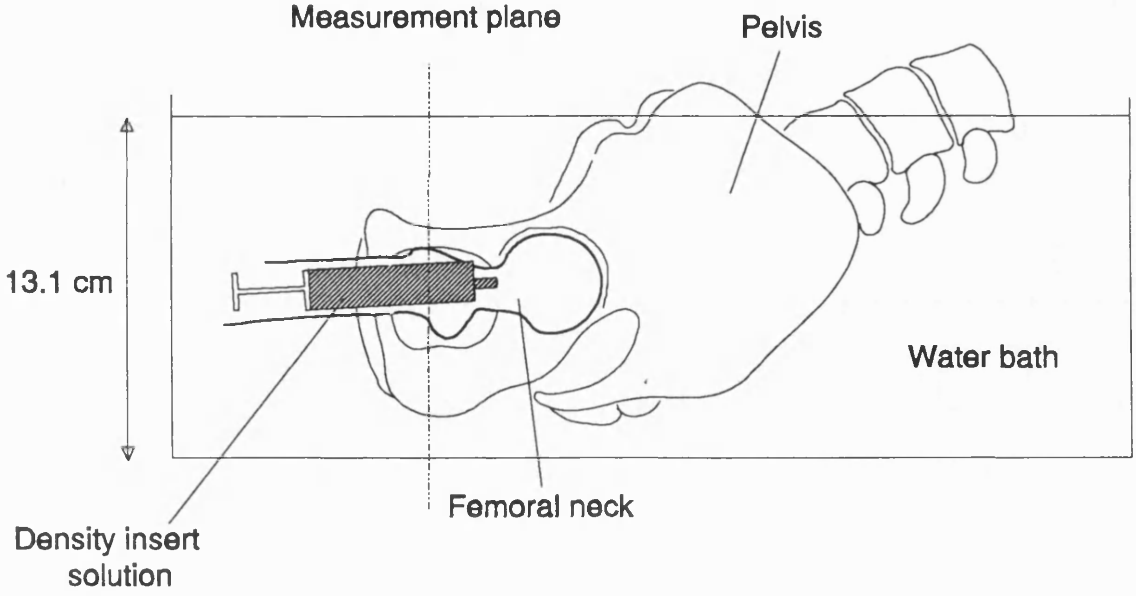

Figure 5.25 Diagram showing section through femur and position of the pelvis bone for the simulated patient.

5.4.0 Scout scan of simulated patient

One of the crucial factors in longitudinal bone density measurements is the reduction of errors due to repositioning. The technique of scout scans in CSD has been described for dry bone samples and phantoms in section 4.3.4. Several scout scans at different kV_p values were performed in order to assess the optimum kV_p value for a scan of a patient. The results of these scans are shown in figure 5.26, where the structure of the scans compares well with those shown in figures 4.19 and 4.21 for the phantom studies. Structural details of the simulated patient bone formation are apparent in the scan and corresponded well to lead markers placed on the pelvis and femur.

which ?

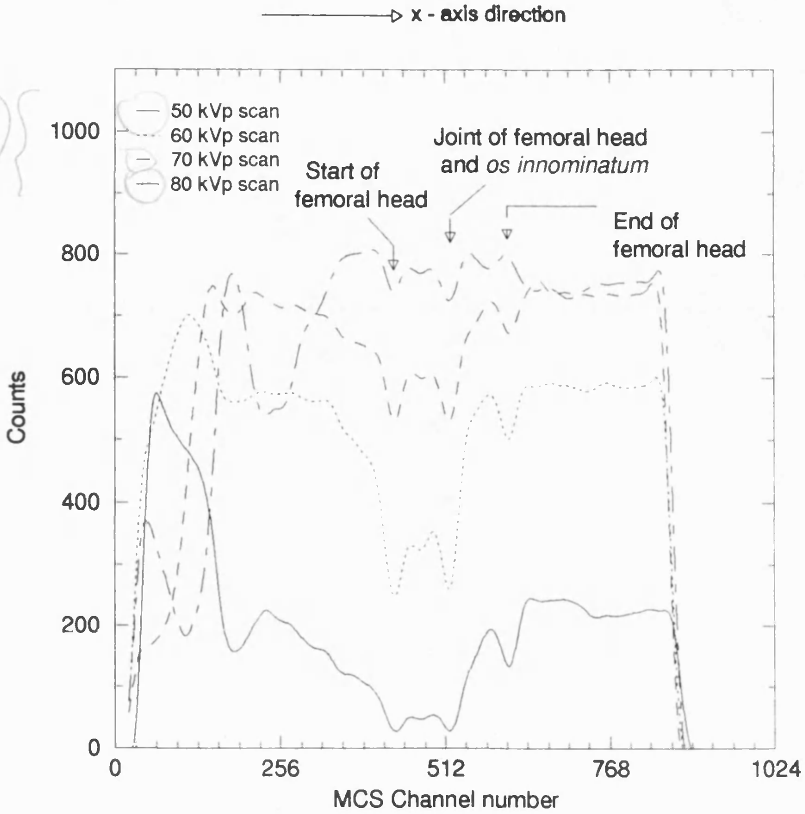

Figure 5.26 Scout scans of the simulated patient performed at several incident kV_p values.

From this data an incident kV_p value of 60-70 kV_p was selected as producing the clearest indication of tissue boundaries in the simulated patient. This data was then used to position the critical volume along the x-axis within the centre of the femoral shaft at the femoral neck, which would produce a density value for the density solution insert. The greater trochanter on the femur bone was used as a landmark to position the critical volume along the y-axis and z-axis, as described in section 4.3.4.

5.4.1 Results from the simulated patient

Several sets of density data were collected using a 120 kV_p incident spectrum for 30 s exposure time, as described previously in section 5.1 for the phantom measurements. The radiation beam path length through the water depth used (tissue equivalent thickness) was 14.5 cm, yielding a calibration value (*k*) of 5.2 from the calibration data plotted in figure 5.10. The density solution inserts used in the simulated patient measurements were 1.05, 1.13, 1.25 and 1.30 gcm^{-3}. Calibrated density results from these measurements are plotted in figure 5.27 and were found to correspond well with the physical density of the density insert solutions. The precision of the CSD density data sets was found to be ~1.1% (CV value) which agreed well with the CV of the femoral neck phantom measurements, a measurement site of comparable size. A phantom of comparable dimensions was required as precision had been found to alter with phantom size (§ 5.1.3)

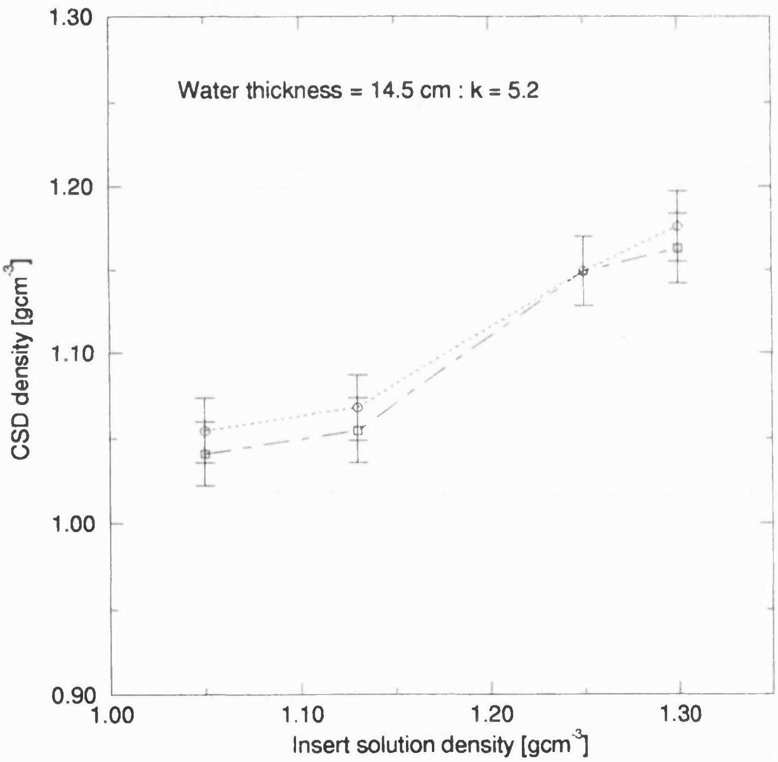

Figure 5.27 Example of results from CSD density measurements made on the simulated patient [120 kV$_p$; 30 s]

5.4.2 Comparison of CSD simulated patient data with DEXA measurements

In order to compare the CSD results from the simulated patient with an established clinical technique, a DEXA scan of the simulated patient was made using the Hologic QDR 1000/W and the protocol described previously in section 5.2.1. The soft tissue background for the DEXA dual-energy calculation was set as the entire width of the water bath. The BMD values obtained from the scans of the simulated patient with different density inserts are shown in table 5.6 and an example DEXA scan is shown in figure 5.28.

Phantom	**Simulated patient**			
Known density insert [gcm^{-3}]	1.05	1.13	1.25	1.3
DEXA measured BMD [gcm^{-2}]	0.918 ± 0.009	0.980 ± 0.01	1.106 ± 0.011	1.130 ± 0.011

Table 5.6 Table showing BMD values of the simulated patient DEXA measurements.

These results have similar BMD values to the DEXA measurements on the bone-containing phantoms described in section 5.2.1.1. These phantoms were of similar dimensions and contained bone tissue samples from the femoral head. Similar results were expected as the cortical bone thickness and trabecular bone region density were comparable between these phantoms and the simulated patient.

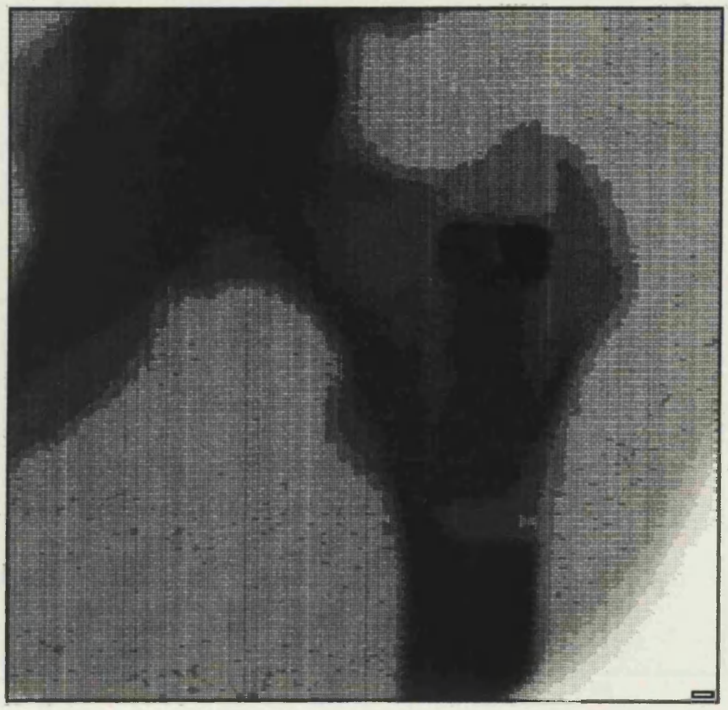

Figure 5.28 An example scan from a DEXA measurement on the femoral shaft of the simulated patient containing a 1.30 gcm^{-3} density solution [Hologic QDR 1000/W].

The correlation between the CSD and the DEXA measurements on the simulated patient was found to be very high, which would imply that the CSD measurements on the simulated patient were as sensitive as those density measurements performed on the phantoms as described in section 5.2.1. For the example measurements shown in figure 5.27 the correlation coefficients (r) were 0.992 and 0.997, with p values of <0.005 indicating a significant correlation. The correlation regressions are shown in figure 5.29.

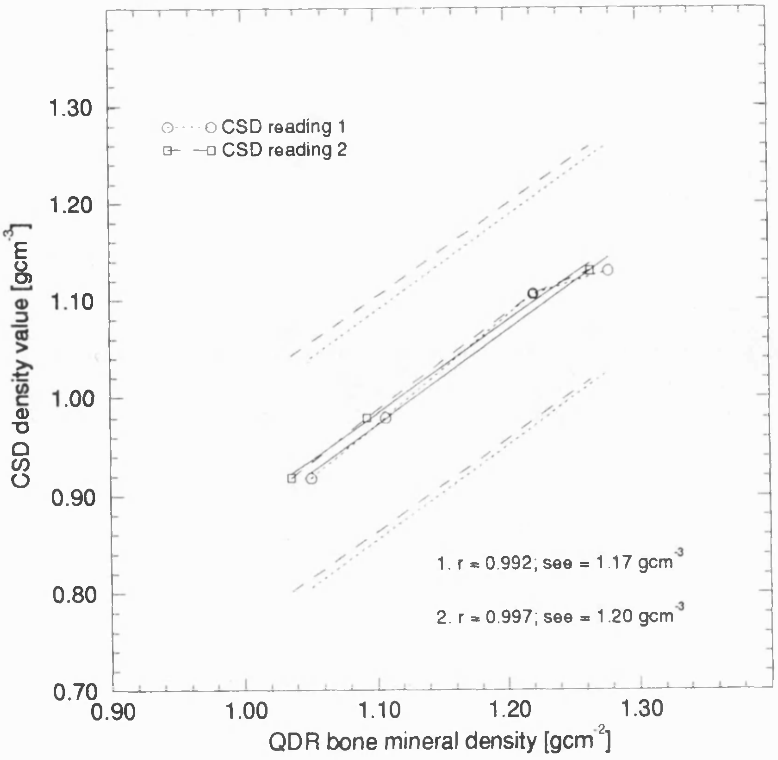

Figure 5.29 Graph showing correlation of two CSD density measurements with DEXA BMD measurements made on the simulated patient ($p<0.005$).

5.4.3 Discussion of simulated patient results

From the results shown in figure 5.27 it was apparent that the use of CSD can produce density measurements which agree well with the physical density within the critical volume within the measurement site. However, the use of a simulated patient introduced several factors which were had not been accounted for in these measurements.

The calibration factors (*k*) (§ 5.1.5) were calculated using phantoms mainly composed of soft tissue substitute, instead of water as used in the simulated patient, which may have altered the way in which the scattered photon spectrum was attenuated. Similarly, the incident spectrum entering the critical volume may have been slightly altered, producing a shifted scatter spectrum. To account for this, calibration factors should be calculated for a range of water thicknesses. Also the energy windows on the SCA, used to process the detector signals, may need to be adjusted according to any shift in spectrum. The scattering properties of water are also slightly different from the scattering properties of soft tissue and adipose, which were used to calculate the multiple scatter correction factors (*mcf*) for the phantoms used in these studies. These changes may account for the slight difference in the gradient of the graph in figure 5.27, which indicated a slightly reduced CSD density value at the higher density insert values. However, any corrections due to these factors are small as the agreement between the CSD density evaluations and the physical density at the critical volume was good.

Chapter 6.

Conclusions and future work

6.0 Conclusions to thesis

The first part of this thesis has shown that Monte Carlo based computer simulations can model the interactions involved in a photon absorptiometry (PA) bone mass measurement. The results show that scatter has a detrimental effect on the calculation of bone mass (M_b) for PA techniques. The data produced from the computer simulations have shown significant levels of scattered x-ray radiation in the detected beam. When primary radiation only is considered both the dual photon absorptiometry (DPA) and dual energy x-ray absorptiometry (DEXA) techniques produce the same value for M_b within statistical limits. The inclusion of scatter in the M_b calculations produces a reduction of between 0.5% and 3.5% depending on the system type and measurement site size. If data collected on different systems were compared, part of this deficit would remain even if the scatter in an individual system had been 'corrected for' by calibration. This deficit would be 0.8% for a femoral neck measurement and between 0.9% to 1.5% for a lumbar spine measurement.

!

why?

Serial measurements of bone density over long periods of time may entail changes in the dimensions of the patient. Calibration with a known density phantom cannot remove the scatter effect due to the phantom being a different size to the patient under examination. This effect has been shown to reduce the value of M_b by 0.5% to 1.0%.

Although these systems have been shown to be reasonably insensitive to the degree of scatter contribution in the detected beam, the inclusion of scatter will produce errors of the order of 1%. This may be significant since density changes reflect bone strength changes of a factor of two greater (Mosekilde *et al*, 1987). Thus, when performing serial measurements patient size should be taken into account or when comparing measured values with previously obtained data sets the conditions of measurement should be considered.

The second part of this thesis has shown that scatter can be used as a source of information about bone density. The continuing development of a device using the principles of Compton scatter densitometry has been described. By using experimental and Monte Carlo based computer simulation results an optimum incident x-ray beam kV_p was found, and an optimum exposure time of 30 s for a large subject was determined.

The detrimental effects of multiple scatter in CSD have been well documented (Battista and Bronskill, 1978; Speller and Horrocks, 1988). By use of computer simulation studies the effects of multiple scatter were reduced by the calculation and implementation of energy windows in the detector signal processing system. The effects of multiple scatter within the detected signal were corrected for by applying calculated correction factors (*mcf*). These were calculated for each phantom measured in the CSD gantry geometry. These developments together with the replacement of the transmission detector copper filtration with a pinhole diaphragm led to reproducible density measurements with a precision (CV) of less than 1% (femoral neck measurement).

Measurements were performed on a variety of realistic phantoms containing of bone substitute and bone tissue samples. The data obtained from the bone substitute inserts of known density allowed calibration constants (*k*) to be calculated, which were then applied to density measurements of phantoms with an unknown bone density. The calibration constants also included the multiple scatter correction factors. These same phantoms were also measured on a clinical DEXA machine and by QCT which are established methods of bone density and bone mass measurement. All the measurements were found to correlate well with the CSD technique, with r=0.90 for QCT and r=0.95 for DEXA.

A method for locating the bone within a measurement site using the CSD gantry has been demonstrated. The use of scout scans and landmarks enabled reproducible positioning of the bone, which is an essential component of any future screening program.

Scout scans were successfully used on a series of CSD density measurements made on the femoral shaft within a simulated patient. The critical volume was positioned within the femur bone which contained a density solution insert. The CSD measurements were repeated and found to have a precision of 1.1%. The calibrated density results were found to agree well with the physical density of the density solution inserts, and correlated well (r=0.992) with a series of DEXA BMD measurements performed on the same measurement site.

Dose measurements on phantoms were made and the data obtained used to calculate an effective dose of 6.9 μSv for a femoral neck measurement. Comparison of this value with published data on other radiographic techniques has shown CSD to be a low dose technique.

6.1 Future work and development

This section will outline some ideas for the future development of the scatter studies in bone density and bone mass measurements presented in this thesis.

6.1.0 Further modelling of PA systems

In order to apply corrections for the effects of scatter in clinical situation a broader base of data must be accumulated. This would involve modelling other commercial densitometers in clinical use over the range of patient sizes. Corrections could then be applied to existing data-bases to allow better comparison between different densitometry techniques.

With the increasing availability of high-speed computers the statistical quality of the Monte Carlo data can be improved. This may also enable the simulation to be extended to provide dose distributions within the patient during a bone density scan.

6.1.1 Assessing multiple scatter in CSD

A range of multiple scatter correction factor (*mcf*) have been calculated for the CSD apparatus described in this thesis. The simulation of the multiple scatter is modelled using phantoms and the values for the patients interpolated according to size and applied together with the calibration constant.

An easier and more direct technique would be to monitor the multiple scatter associated with a CSD measurement on each patient. The calculation of multiple scatter correction factors is a highly geometry dependent problem and a direct measurement from a patient would help to eliminate any error from the misalignment of patient geometry and Monte Carlo computer simulation geometry. This would require a study which monitored the scatter output from various volumes of tissue within the measurement site to find a relation between the scatter from the tissue volume and the multiple scatter calculated from Monte Carlo computer simulations. This would require apparatus which duplicated the CSD gantry geometry but without the constraints of the gantry supporting structure. A scatter monitor would probably consist of a third scatter detector collimated in such a way that the critical volume is not within the acceptance cone of the collimator. This detector would monitor the scatter level within the tissue surrounding the critical volume. This would include the multiple scatter from the phantom and single scatter from a second critical volume it would form with the transmission collimator in the tissues surrounding the density evaluation critical volume. This method would allow some aspect of multiple scatter from the critical volume to be included in the total assessment of multiple scatter from the measurement site. Figure 6.1 shows a schematic diagram of this arrangement.

If a rational relationship between the ratio of scatter from the detector and the transmitted beam ($S_3/T_{1,2}$) and the computer simulation *mcf* values was found, then a multiple scatter monitor could be included in the CSD apparatus.

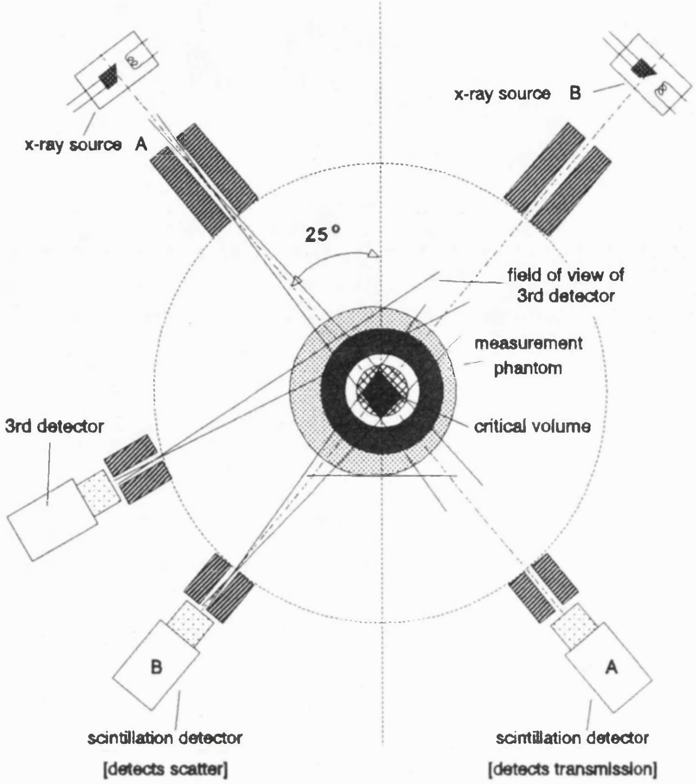

Figure 6.1 Schematic diagram of CSD apparatus showing position of 3rd detector used for assessment of multiple scatter.

6.1.2 Development of CSD scout scans

Scout scans in the z-axis direction were not found to be successful on bone samples because of the restricted movement of the gantry in that direction. The success of the scout scans in the x-axis direction would indicate that a redesign of the gantry to enable z-axis scans would be worthwhile. This would involve increasing the size of the gantry bore into which the patient fits, which would require recalculation of geometry dependent variables such as the *mcf* values.

6.1.3 Improvement of CSD collimation design

The precision of the CSD technique is basically determined by the statistical quality of the scatter counts S_1 and S_2. An improved detector collimator design would ideally collect more scatter counts without distorting or enlarging the critical volume. This would involve collecting the scatter counts around the azimuthal angle of scatter focused on the critical volume.

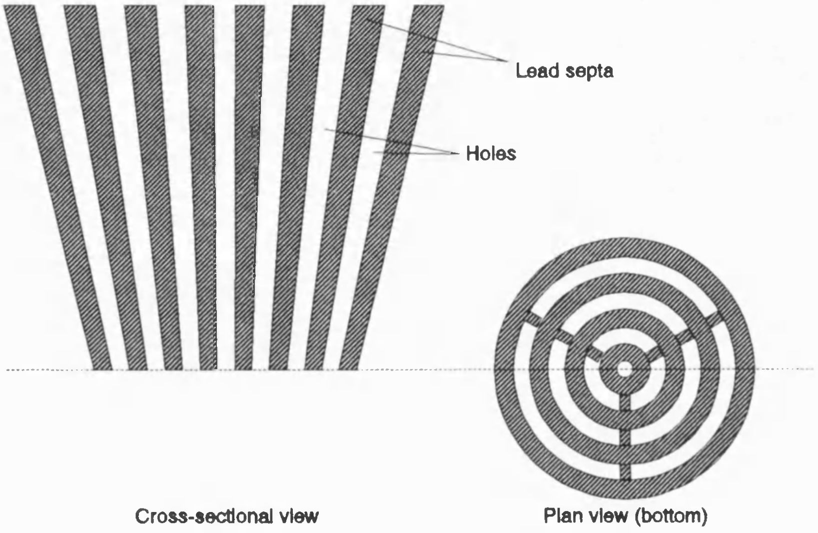

Figure 6.2 Schematic diagram of proposed improvement to CSD gantry detector collimators.

This particular form of collimator would involve a critical volume made up of the intersection of focused scatter cones and the incident beam. This would require the recalculation of the critical volume dimensions and the recalculation of the *mcf* values for the gantry. Any improvement in the statistical quality of the data and reduction in patient dose would have to be balanced with any loss of precision through increased multiple scatter detection, for example.

6.1.4 Measurements on patients

The CSD gantry described has been shown to give reproducible bone density measurements on the femoral neck site with a CV of <1% for phantoms. For a simulated patient the precision was found to be 1.1% at a femoral shaft measurement site. The effective dose for such a measurement is 6.9 µSv. The calculation of calibration constants enables a value for mineral equivalent density to be found for a subject with unknown bone density. This would indicate that a series of measurements on a set of patients would be the next step in this project. Ideally the patient population would be measured on the CSD system and a measurement of the same site made on a DEXA machine or other established clinical technique.

The results from the phantom and simulated patient bone density measurements would indicate that the necessary precision is available to warrant a study on a patient population with the apparatus described, without imparting a high radiation dose to the subjects.

Appendix 1.

Optimal Wiener filtering.

The removal of noise from a 'corrupted' signal is a filtration technique routinely handled by Fourier analysis. A detailed reference for the following description is provided by Press *et al* (1986). If we consider an 'uncorrupted' signal *u(t)* which we require to measure, an imperfect measuring device (e.g. a scintillation detector system) will provide a corrupted signal *c(t)*. This signal *c(t)* may be degraded in two respects; firstly the measurement device may not have a perfect delta-function response so that the true signal *u(t)* is convolved with some known response function *r(t)* to give a signal *s(t)*, where;

$$s(t) = \int_{-\infty}^{\infty} r(\tau)\, u(t-\tau)\, d\tau \qquad \text{A.1}$$

or

$$S(f) = R(f)\, U(f) \qquad \text{A.2}$$

where

S, R, U are the Fourier transforms of s, r, u respectively.

Secondly, the measured signal *c(t)* may contain a noise component *n(t)*, where

$$c(t) = s(t) + n(t) \qquad \text{A.3}$$

we require an optimal filter $\phi(t)$ or $\Phi(f)$ which when applied to *c(t)* or *C(f)* and deconvolved with *r(t)* or *R(f)*, produces a signal $\hat{u}(t)$ or $\hat{U}(f)$ which is as close as possible to *u(t)* or *U(f)*.

$$\hat{U}(f) - \frac{C(f)\,\Phi(f)}{R(f)} \qquad \text{A.4}$$

$\hat{U}$ is close to U in the least squares sense where

$$\int_{-\infty}^{\infty} |\hat{u}(t) - u(t)|^2\, dt - \int_{-\infty}^{\infty} |\hat{U}(f) - U(f)|^2\, df \qquad \text{A.5}$$

is minimised.

By substituting these equations and minimising the integrand with respect to $\Phi(f)$ gives;

$$\Phi(f) - \frac{|S(f)|^2}{|S(f)|^2 + |N(f)|^2} \qquad \text{A.6}$$

which provides the optimal filter $\Phi(f)$.

To determine $\Phi(f)$ the separate estimates of $|S|^2$ and $|N|^2$ must be obtained, and a simple and sufficiently accurate method is to plot the power spectrum of the data set $c(t)$, where;

$$|S(f)|^2 + |N(f)|^2 \sim P_c(f) - |C(f)|^2 \qquad \text{A.7}$$

where

$P_c(f)$ power spectrum of the data set $c(t)$

$0 \le f < f_c$

The resulting plot will show the spectral signature of the signal above a continuous noise spectrum. The noise spectrum may be flat, tilted or curved; this is not important as long as a reasonable smooth curve can be drawn through the noise spectrum and extrapolated into the region dominated by the signal. A smooth curve is drawn through the signal plus noise part of the spectrum and the difference between the two curves is the smooth 'model' of the signal power $|S|^2$ (see figure A.1)

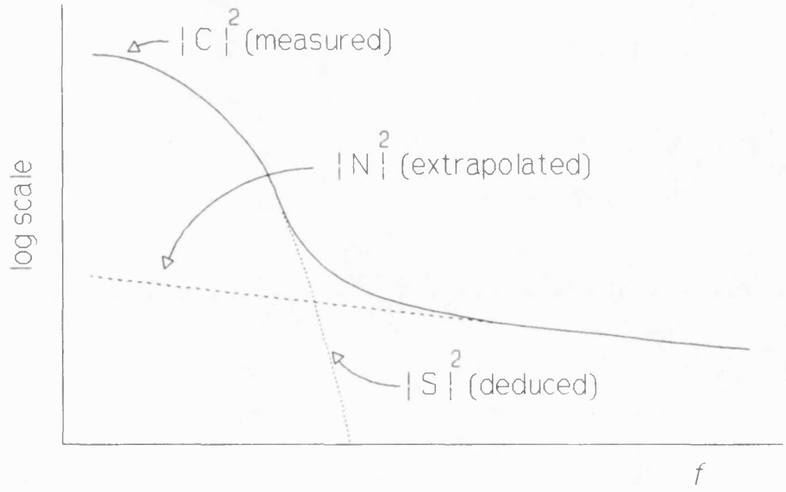

Figure A.1 Diagram showing the power spectrum of the data set *c(f)* showing the signal and noise component models.

By dividing the smooth model $|S|^2$ by the signal+noise model $|S|^2 + |N|^2 = |C|^2$ the result provides the optimal filter $\Phi(f)$.

For the data sets studied in this thesis the response function *r(t)* was considered as unity. The power spectra were plotted out and curves fitted to the signal+noise and the noise parts of the spectra using linear and non-linear least squares fitting. The optimal filter produced was convolved with the transformed data sets and an inverse transform performed on the result to return the optimally filtered data.

References

Andreo P. **1991** Monte Carlo techniques in medical radiation physics.
Phys. Med. Biol. **36** 861-920

Baba-Hamed T. **1990** Applications of dual energy techniques for tissue characterisation in conventional diagnostic radiology.
Ph.D. Thesis (University of London, London, UK) 13-21

Balseiro J, Fahey F H, Ziessmann H A and Le T V. **1988** Comparison of bone mineral density in both hips.
Radiol. **167** 151-153

Banks L M and Stevenson J C. **1986** Modified method of spinal computed tomography for trabecular bone mineral measurements.
J. Comp. Assist. Tomo. **10** 463-467

Barnett E and Nordin B E C. **1960** The radiological diagnosis of osteoporosis: a new approach.
Clin. Rad. **11** 166-174

Barrett H H and Swindell W. **1981** The theory of image formation, detection, and processing.
Radiological Imaging, vol 1. (Academic Press, London) 321-329

Battista J J and Bronskill M J. **1978** Compton scatter tissue densitometry: calculation of single and multiple scatter photon fluences.
Phys. Med. Biol. **23** 1-23

Battista J J and Bronskill M J. **1981** Compton scatter imaging of transverse sections: an overall appraisal and evaluation for radiotherapy planning.
Phys. Med. Biol. **26** 81-99

Battista J J, Santon L W and Bronskill M J. **1977** Compton scatter imaging of transverse sections: corrections for multiple scatter and attenuations.
Phys. Med. Biol. **22** 229-244

Birch R, Marshall M and Ardran G M. **1979** The Hospital Physicists' Association Catalogue of spectral data for diagnostic x-rays.
Scientific report series **30** The Hospital Physicists' Association

Block J E, Smith R, Claus-Christian G, Steiger P, Ettinger B and Genant H K. **1989** Models of spinal trabecular bone loss as determined by Quantitative Computed Tomography.
J. Bone. Miner. Res. **4** 249-257

Britton J M and Davie M W J. **1990** Mechanical properties of bone from the iliac crest and relationship to L5 vertebral bone.
Bone **11** 21-28

Cameron J R and Sorenson J. **1963** Measurement of bone mineral *in vivo*: an improved method.
Science **142** 230-232

Cann C E. **1988** Quantitative computed tomography for determining bone mineral density : a review.
Rad. **166** 509-522

Cann C E, Genant H K, Kolb F O and Ettinger B. **1985** Quantitative computed tomography for prediction of vertebral fracture risk.
Bone **6** 1-7

Chan H P and Doi K. **1985** Physical characteristics of scattered radiation in diagnostic radiology: Monte Carlo simulation studies.
Med. Phys. **12** 152-165

Chan H P and Doi K. **1986** Some properties of photon scattering in water phantoms in diagnostic radiology.
Med. Phys. **13** 824-830

Christiansen C and Rødbro P. **1977** Long term reproducibility of bone mineral content measurements.
Scand. J. Clin. Lab. Invest. **37** 321-329

Clarke R L and van Dyke P. **1973** A new method for measurement of bone mineral content using both transmitted and scattered photon beams of gamma rays.
Phys. Med. Biol. **18** 532-537

Cohn S H, Dombrowski C S and Fairchild R G. **1977** *In vivo* neutron activation analysis of calcium in man.
Int. J. Appl. Radiat. Isot. **31** 127-138

Compston J E, Evans W D, Crawley E O and Evans C. **1988** Bone mineral content in normal UK subjects.
Brit. J. Radiol. **61** 631-636

Cullum I D, Ell P J and Ryder J P. **1989** X-ray dual-photon absorptiometry: a new method for the measurement of bone density.
Brit. J. Radiol. **62** 587-592

De Vries D J, Moore S C, Zimmermann R E, Mueller S P, Friedland B and Lanza R C. **1990** Development and validation of a Monte Carlo simulation of photon transport in an Anger camera.
IEEE Trans. on Med. Imag. **9** 430-438

Dawson-Hughes B, Deehr M S, Berger P S, Dallal G E and Sadowski L J. **1989** Correction of the effects of source, source strength, and soft-tissue thickness on spine dual-photon absorptiometry measurements.
Calcif. Tiss. Int. **44** 251-257

Dequeker J. **1973** Bone and aging. Differentiation between physiological and pathological bone loss.
Clinical aspects of metabolic bone disease ed. Frame B *et al* (Amsterdam: Excerpta Medica)

DeSimone D P, Stevens J, Edwards J, Shary J, Gordon L and Bell N H. **1989** Influence of body habitus and race on bone mineral density of the mid-radius, hip, and spine in aging women.
J. Bone. Miner. Res. **4** 827-830

Duke P R and Hanson J A. **1984** Compton scatter densitometry with polychromatic sources.
Med. Phys. **11** 624-632

Dunn W L, Kan S H and Wahner H W. **1987** Errors in longitudinal measurements of bone mineral: effect of source strength in single and dual photon absorptiometry.
J. Nucl. Med. **28** 1751-1757

Eriksson S, Isberg B and Lindgren U. **1988** Vertebral bone mineral measurement using dual photon absorptiometry and computed tomography.
Acta. Radiol. **29** 89-94

Gotfredsen A, Pødenphant J, Nørgaard H, Nilas L, Hers Nielsen V and Christiansen C. **1988** Accuracy of lumbar spine bone mineral content by dual photon absorptiometry.
J. Nucl. Med. **29** 248-254

Gray H. **1988** *Gray's Anatomy* ed. Pick T P and Howden R (Galley Press, London, UK)

Haddaway M J, Davie M W J and McCall I W. **1992** Bone mineral density in healthy normal women and reproducibility of measurements in spine and hip using dual-energy x-ray absorptiometry.
Brit. J. Radiol. **65** 213-217

Hansen M A, Hassager C, Overgaard K, Marslew U, Riis B J and Christiansen C. **1990** Dual-energy x-ray absorptiometry: a precise method of measuring bone mineral density in the lumbar spine.
J. Nucl. Med. **31** 1156-1162

Hanson J A, Moore W E, Figley M M and Duke P R. **1984** Compton scatter with polychromatic sources for lung densitometry.
Med Phys **11** 633-637

Hansson T and Roos B. **1986** Age changes in the bone mineral of the lumbar spine in normal women.
Calcif. Tiss. Int. **38** 249-251

Hansson T, Roos B and Nachemson A. **1980** The bone mineral content and ultimate compressive strength of lumbar vertebrae.
Spine **5** 46-55

Harding G and Tischler R. **1986** Dual energy Compton scatter tomography.
Phys. Med. Biol. **31** 477-489

Hedlund L R and Gallagher J C. **1989** The effect of age and menopause on bone mineral density of the proximal femur.
J. Bone. Miner. Res. **4** 639-642

Houston R A. **1943** *A treatise on light* (Longmans, London, UK)

Hubbell J H. **1964** Common volume of two intersecting cylinders.
J. Res. Nat. Bur. Stand. **69C** (2) 139-143

Hubbell J H. **1969** Photon cross-sections, attenuation coefficients and energy absorption coefficients for 10 keV to 100 GeV.
NSRDS-NBS **29**

Huddleston A L and Bhaduri D. **1979** Compton scatter densitometry in cancellous bone.
Phys. Med. Biol. **24** 310-318

Huddleston A L, Bhaduri D and Weaver J. **1979** Geometrical considerations for Compton scatter densitometry.
Med. Phys. **6** 519-522

Huddleston A L and Sackler J P. **1985** The determination of electron density by the dual energy Compton scatter method.
Med. Phys. **12** 13-19

ICRP. **1974**. *ICRP Publication 23* (Pergamon Press, Oxford, UK)

ICRP. **1977**. *ICRP Publication 26* (Pergamon Press, Oxford, UK)

ICRP. **1991**. *ICRP Publication 60* (Pergamon Press, Oxford, UK)

ICRU Report 24. **1976** *Determination of absorbed dose in a patient irradiated by beams of X or gamma rays in radiotherapy procedures.* (ICRU, Washington, USA) 4-6

Kennett T J and Webber C E. **1976** Bone density measured by photon scattering. II. Inherent sources of error.
Phys. Med. Biol. **21** 770-780

Kerr S A, Kouris K, Webber C E and Kennett T J. **1980** Coherent scattering and the assessment of mineral concentration in trabecular bone.
Phys. Med. Biol. **25** 1037-1047

Kleerekoper M, Parfitt A M and Ellis B I. **1985** Measurement of vertebral fracture rates in osteoporosis.
Osteoporosis I. Proceedings of the Copenhagen International Symposium ed. Christiansen C *et al* Copenhagen 103-109

Knoll G F. **1979** *Radiation detection and measurement.* (Wiley, London, UK) 131-139

Knuth D E. **1969** Semi-numerical algorithms.
The art of computer programming, vol. 2 (Addison-Wesley, Reading, UK) 54-65

Koligliatis T. **1990** A scattering method for bone density measurements with polychromatic sources.
Ph.D Thesis. (University of London, London, UK).

Krølner B and Nielsen S P. **1980** Measurement of bone mineral content (BMC) of the lumbar spine. I. Theory and application of a new two-dimensional dual photon attenuation method.
Scand. J. Clin. Lab. Invest. **40** 653-664

Krølner B and Nielsen S P. **1982** Bone mineral content of the lumbar spine in normal and osteoporotic women: cross-sectional and longitudinal studies.
Clin. Sci. **62** 329-336

Krølner B, Nielsen S P, Lund B, Lund Bj, Sørenson O H and Uhrenholdt A. **1980** Measurement of bone mineral content (BMC) of the lumbar spine, II. Correlation between forearm BMC and lumbar spine BMC.
Scand. J. Clin. Lab. Invest. **40** 655-670

Kruse H I P and Kuhlencordt F. **1983** Studies in primary osteoporosis.
Osteoporosis a multidisciplinary problem ed. St J Dixon A (Academic Press, London, UK) 149-152

Lambiase R, Sartoris D J, Fellingham L, Andre M and Resnick D. **1987** Vertebral mineral status: assessment with single- verses multi-section CT.
Rad. **164** 231-236

Leichter I, Karellas A, Shukla S S, Looper J L and Craven J D. **1985** Quantitative assessment of bone mineral by photon scattering - calibration considerations.
Med. Phys. **12** 466-468

Lindley D V and Scott W F. **1984** *New Cambridge elementary statistical tables.*
(Cambridge University Press, Cambridge, UK) 40-42

Mazess R B, Bardin H S and Ettinger M. **1988** Radial and spine bone mineral density in a patient population.
Arth. Rheum. **31** (7) 891-897

Mazess R B, Pedersen P, Vetter J and Bardin H S. **1991** Bone densitometry of excised vertebrae; anatomical relationships.
Calcif. Tiss. Int. **48** 380-386

Mazess R B, Peppler W W, Chesney R W, Lange T A, Lindgren U and Smith E, Jr. **1984** Total body and regional bone mineral by dual-photon absorptiometry in metabolic bone disease.
Calcif. Tiss. Int. **36** 8-13

Morin R L, Raeside D E, Goin J E and Widman J C. **1979** Monte carlo advice.
Med. Phys. **6** 305-306

Mosekilde L, Mosekilde L and Danielson C C. **1987** Biomechanical competence of vertebral trabecular bone in relation to ash density and age in normal individuals.
Bone **8** 79-85

Nelp W B, Palmer H E, Murano R, Pailthorp K, Hinn G M, Rich C, Williams J L, Rudd T G and Denny J D. **1970** Measurement of total body calcium (bone mass) *in vivo* with the use of total body neutron activation analysis.
J. Lab. Clin. Med. **76** 151-163

Nilas L and Christiansen C. **1987** Bone mass and it's relationship to age and the menopause.
J. Clin. Endo. Metab. **65** 697-702

NRPB Report R200. **1986** *A national survey of doses to patients undergoing a selection of routine x-ray examinations in English hospitals.* (NRPB, Didcot, Oxfordshire, UK)

Pacifici R, Susman N, Carr P L, Birge S J and Avioli L V. **1987** Single and dual energy tomographic analysis of spinal trabecular bone: a comparative study in normal and osteoporotic women.
J. Clin. Endo. Metab. **64** 209-214

Parfitt A M. **1983** The physiologic and clinical significance of bone histomorphetric data.
Bone Histomorphometry: Techniques and Interpretation. ed Recher R (CRC Press, Boca Raton, UK) 143-223

Pocock N A, Eisman J A, Mazess R B, Sambrook P N, Yeates M G and Freund J. **1988** Bone mineral density in Australia compared with the US.
J. Bone. Miner. Res. **3**(6) 601-604

Pouilles J M, Tremollieres M, Louvet J P, Fournie B, Morlock G and Ribot C. **1988** Sensitivity of dual-photon absorptiometry in spinal osteoporosis.
Calcif. Tiss. Int. **43** 329-334

Press W H, Flannery B P, Teukolsky S A and Vetterling W T. **1986** *Numerical recipes. The art of scientific computing.* (Cambridge University Press, Cambridge, UK) 484-488

Puumalainen P, Uimarihuhta A, Olkkonen H and Alhava E M. **1982** A coherent/Compton scattering method employing an x-ray tube for measurement of trabecular bone mineral content.
Phys. Med. Biol. **27** 425-429

Pye D W, Hannan W J and Hesp R. **1990** Effective dose equivalent in dual x-ray absorptiometry.
Brit. J. Radiol. **63** 149-151

Raeside D E. **1976** Monte carlo principles and applications.
Phys. Med. Biol. **21** 181-197

K
Reinbold W D, Genant H K, Reiser U J, Harris S T and Ettinger B. **1986** Bone mineral content in early-postmenopausal and postmenopausal osteoporotic women: comparison of measurement methods.
Rad. **160** 469-478

Riggs B L, Wahner H W, Dunn W L, Mazess R B, Offord K P and Melton L J. **1981** Differential changes in Bone mineral density of the appendicular and axial skeleton with aging. Relationship to spinal osteoporosis.
J. Clin. Invest. **67** 328-335

Riggs B L, Wahner H W, Melton L J, Richelson L S, Judd H L and Offord K P. **1986** Rates of bone loss in the appendicular and axial skeletons of women. Evidence of substantial vertebral bone loss before menopause.
J. Clin. Invest. **77** 1487-1491

Riggs B L, Wahner H W, Seeman E, Offord K P, Dunn W L, Mazess R B, Johnson K A and Melton L J. **1982** Changes in bone mineral density of the proximal femur and spine with aging. Differences between the postmenopausal and senile osteoporosis syndromes.
J. Clin. Invest **70** 716-723

Roos B O, Hansson T H and Sköldborn H. **1980** Dual photon absorptiometry in lumbar vertebrae. Evaluation of baseline error.
Acta Radiol. Oncol. **19** 111-114

Roos B O and Sköldborn H. **1974** Dual photon absorptiometry in lumbar vertebrae. I. Theory and method.
Acta Radiol. Ther. Phys. Biol. **13** 266-280

Royle G J. **1992** Elastic photon scattering for tissue analysis
Ph.D. Thesis (University of London, London, UK) *to be submitted*

Royle G J and Speller R D. **1991** Low angle x-ray scattering for bone analysis.
Phys. Med. Biol. **36** 383-389

Royle G J and Speller R D. **1992** Phantoms for evaluating the performance characteristics of bone densitometers.
Brit. J. Radiol. (accepted for publication)

Ruegsegger P, Anliker M and Dambacher M. **1981** Quantification of trabecular bone with low dose computed tomography.
J. Comput. Assist. Tomogr. **5** 384-390

Ruegsegger P, Dambacher M D, Ruegsegger E, Fisher J A and Anliker M. **1984** Bone loss in premenopausal and postmenopausal women. A cross-sectional and longitudinal study using quantitative computed tomography.
J. Bone. Joint Surg. **66** 1015-1023

Sartoris D J, Andrè M, Resnick C and Resnick D. **1986** Trabecular bone density in the proximal femur: Quantitative CT assessment.
Rad. **160** 707-712

Shipp C C, Berger P S, Deehr M S and Dawson-Hughes B. **1988** Precision of dual-photon absorptiometry.
Calcif. Tiss. Int. **42** 287-292

Smith W S and Kruger R A. **1986** A signal processing model of diagnostic x-ray scatter.
Med. Phys. **13** 831-835

Sorenson J A and Floch J. **1985** Scatter rejection by air-gaps : an empirical model.
Med. Phys. **12** 308-315

Speller R D and Horrocks J A. **1988** A monte carlo study of multiple scatter effects in Compton scatter density measurements.
Med. Phys. **15** 707-712

Speller R D and Horrocks J A. **1991** Photon scattering - a 'new' source of information in medicine and biology.
Phys. Med. Biol. **36** 1-6

Speller R D, Royle G J and Horrocks J A. **1989** Review article: instrumentation and techniques in bone density measurement.
J. Phys. E. Sci. Instrum. **22** 202-214

Speller R D, White D R, Veerappan R, Coleman A J and Waller P E. **1981** A survey of 29 CT machines in Britain.
Brit. J. Radiol. **54** 123

Spiegel M R. **1961** *Schaum's outline of theory and problems of statistics.* (Schaum Publishing Company, New York, USA) 241-248

Steiger P, Block J E, Steiger S, Heinck A F, Friedlander A, Ettinger B, Harris S T, Glüer C C and Genant H K. **1990** Spinal bone mineral density measured with quantitative computed tomography: Effect of regions of interest, vertebral level, and technique.
Rad. **175** 537-543

Storm E and Israel H I. **1970** Photon cross-sections from 1 keV to 100 MeV for elements Z=1 to 100.
Nuclear Data Tables **A7** 565-635

Thomsen K, Gotfredsen A and Christiansen C. **1986** Is postmenopausal bone loss an age-related phenomenon?
Calcif. Tiss. Int. **39** 123

Tothill P, Smith M A and Sutton D. **1983** Dual photon absorptiometry of the spine with a low activity source of Gd-153.
Brit. J. Radiol. **56** 829-835

Tothill P, Pye D M and Teper J. **1988** The influence of extra-skeletal fat on the accuracy of DPA of the spine.
Clin. Phys. Physiol. Meas. **9** 177-184

Wahner H W, Dunn W L, Mazess R B, Towsley M, Lindsay R, Markhard L and Dempster D. **1985** Dual-photon Gd-153 absorptiometry of bone.
Rad. **156** 203-206

Webber C E and Kennett T J. **1976** Bone density measured by photon scattering. I. A system for clinical use.
Phys. Med. Biol. **21** 760

Williamson J F and Morin R L. **1983** An efficient method of randomly sampling the coherent angular scatter distribution.
Phys. Med. Biol. **28** 57-62

Woodard H Q and White D R. **1982** Bone models for use in radiotherapy dosimetry.
Brit. J. Radiol. **55** 277-282

Woodard H Q and White D R. **1986** The composition of body tissues.
Brit. J. Radiol. **59** 1209

Woolf A D and Dixon A S. **1988** *Osteoporosis : A Clinical Guide.*
[Martin Dunitz, London, UK] 1-23